NORTHWESTERN UNIVERSITY

Three-Dimensional FDTD Modeling of Impulsive Electromagnetic Propagation
in the Global Earth-Ionosphere Waveguide below 30 kHz

A DISSERTATION

SUBMITTED TO THE GRADUATE SCHOOL
IN PARTIAL FULFILLMENT OF THE REQUIREMENTS

for the degree

DOCTOR OF PHILOSOPHY

Field of Electrical Engineering

By

Jamesina Jean Simpson

EVANSTON, ILLINOIS

June 2007

ABSTRACT

Three-Dimensional FDTD Modeling of Impulsive Electromagnetic Propagation
in the Global Earth-Ionosphere Waveguide below 30 kHz

Jamesina J. Simpson

Wave propagation at the bottom of the electromagnetic spectrum (below 300 kHz) in the Earth-ionosphere system is a problem having a rich history of theoretical investigation extending over many decades. Propagation within this system involves complex interactions of electromagnetic waves with the lithosphere, oceans, and ionosphere, leading to resonances that involve literally the entire planet Earth. Currently, electromagnetic phenomena below 300 kHz form the physics basis of remote-sensing investigations of lightning and sprites, global temperature change, subsurface structures, submarine communications, and potential earthquake precursors.

This dissertation addresses the application of the finite-difference time-domain (FDTD) algorithm to model impulsive electromagnetic wave propagation within the global Earth-ionosphere cavity at frequencies below 30 kHz. Two generations of numerical models are presented: a latitude-longitude grid-cell arrangement, and a geodesic grid-cell arrangement. Both types of models extend from 100 km below sea level to an altitude of 100 km, and enable a direct, full-vector, 3-D time-domain Maxwell's equations calculation of electromagnetic wave propagation due to an arbitrary excitation. Furthermore, they can account for arbitrary horizontal as well as vertical geometrical and electrical inhomogeneities and anisotropies of the ionosphere,

lithosphere, oceans, and Earth's magnetic field. First, the models are verified by comparing the FDTD-calculated daytime ELF propagation attenuation with data reported in the literature. Next, four example applications are provided: (1) an investigation of hypothesized preseismic electromagnetic phenomena; (2) the development of a novel subsurface radar designed to sense the presence of major oil deposits; (3) the development of a novel radar for locating and characterizing localized ionospheric anomalies within 100 km of the Earth's surface; and (4) the development of a gyrotropic ionosphere plasma model for studying electromagnetic radiation from lightning and sprites.

ACKNOWLEDGEMENTS

DEDICATION

To Briana – my inspiration to be a better and happy person.

Contents

List of Figures

List of Tables

1   Introduction

1.1   Dissertation Statement

Wave propagation at the bottom of the electromagnetic (EM) spectrum (below 300 kHz) in the Earth-ionosphere system is a problem having a rich history of theoretical investigation extending over many decades (see for example [1–6]). Propagation within this system involves complex interactions of EM waves with the lithosphere, oceans, and ionosphere, leading to resonances that involve literally the entire planet Earth. Currently, EM phenomena below 300 kHz form the physics basis of remote-sensing investigations of lightning and sprites [7], global temperature change [8], subsurface structures [9, 10], submarine communications [11], and potential earthquake precursors [12, 13].

The work discussed in this dissertation advances the state-of-the-art in modeling sub-30 kHz electromagnetic propagation in the Earth-ionosphere waveguide. Presented in the following chapters are two techniques for modeling the Earth-ionosphere waveguide using the finite-difference time-domain (FDTD) [14] solution to Maxwell's equations. Specifically, two-dimensional (2-D) and three-dimensional (3-D) latitude-longitude and geodesic FDTD models are described, along with four novel applications that have been investigated using these advanced models. The following section describes the organization of each of these topics within this dissertation.

1.2   Organization of Dissertation

This dissertation is organized into six chapters. Chapter 2 provides background information on related previous analytical and numerical studies, including both frequency and time-domain investigations. Next, Chapter 3 describes the numerical algorithm for the 2-D and 3-D spherical-coordinate, FDTD grids that are later used to construct the Earth-ionosphere models. These include both the latitude-longitude grid-cell arrangement and the geodesic grid-cell arrangement. Chapter 4 summarizes the parameters (grid size and resolution) and input values (Earth's bathymetry / topography and the electrical properties of the lithosphere, oceans, and ionosphere) used to develop the 3-D grid arrangements of Chapter 3 into realistic models of the Earth-ionosphere waveguide. Chapter 4 also provides a validation study comparing the FDTD-calculated propagation attenuation with data previously reported in the literature. Chapter 5 presents four applications of the 3-D FDTD Earth-ionosphere waveguide models which have been explored to date, including: (1) an investigation of hypothesized preseismic electromagnetic phenomena; (2) the development of a novel subsurface radar designed to sense the presence of major oil deposits; (3) the development of a novel radar for locating and characterizing localized ionospheric anomalies within 100 km of the Earth's surface; and (4) the development of the first 3-D EM solver of the Earth-ionosphere waveguide that incorporates the magnetized gyrotropic ionosphere plasma subjected to the Earth's geomagnetic field. Finally, Chapter 6 provides a summary and a discussion of future research in this area.

2   Background

2.1   Literature Review of Related Analytical and Numerical Studies

Many notable researchers have devoted their attention to the challenge of understanding EM propagation characteristics at frequencies below about 300 kHz. Motivation for work in this area has not only been to understand the basic physics, but also to develop important applications, such as long-range communication and navigation systems.

Many EM propagation problems have been solved analytically (see for example [1 – 6]), or numerically using codes based on waveguide mode theory or the wavehop method [15]. A particularly widely used simulation tool in this area is the LWPC (Long Wave Propagation Code) developed over many years at the Naval Ocean Systems Center [16]. However, none of the above mentioned analytical or numerical techniques are capable of accommodating continuously-varying geometrical and electrical details of the excitations, ionosphere, or lithosphere [17]. On the other hand, because the grid-based FDTD method possesses that capability, the remainder of this dissertation addresses the application of FDTD to modeling EM propagation in the Earth-ionosphere waveguide. First, an overview of related FDTD work by other authors will be covered [18].

2.2   First FDTD Work in this Area

Berenger was the first to use the FDTD method to model subionospheric wave propagation at frequencies below 300 kHz. His conference abstracts in this area date back to 1994 [19]. The goal of his work was initially two fold: (1) to compare FDTD results with previous frequency-

domain mode theory calculations [16]; and (2) to create an entirely new model having the capability of accommodating continuously varying parameters over the propagation path.

The basis for Berenger's first model is a 2-D spherical-coordinate grid extending from the Earth's surface upwards to the effective reflection height in the ionosphere at the frequency of interest, and extending a few thousand kilometers (km) laterally along a great-circle cut. Perfect electric conductor (PEC) boundary conditions terminate the grid in all four directions, and a surface impedance is applied at the Earth's surface to model the finite conductivity of the lithosphere or ocean. Initially the natural geomagnetic field is not taken into account. However this is later modeled in [17] by way of solving the differential equations governing the current density in the ionosphere. The formulation of [17] achieves a gyrotropic (anisotropic) ionosphere model, a feature particularly important for nighttime propagation.

In [17, 20, 21], several techniques are developed to reduce the computational burden of Berenger's grid for modeling propagation over several megameters (Mm). For example, Thevenot et. al. [17] introduce a technique involving a moving computational spatial domain extending backwards from the wavefront until steady state is attained. So long as reflections from the rear grid edge (opposite to the direction of interest) and propagation speeds are carefully considered, this technique can be used to significantly decrease the size of the grid.

A second way Berenger reduces the computational burden is by counteracting the numerical angular dispersion inherent to the FDTD mesh [20]. This strategy permits the use of coarser grids. That is, high-resolution meshes are needed for subionospheric propagation in the 3 – 300 kHz range because "more than ten modes contribute significantly to the field strength" [20]. Each of these modes propagates with a different eigenangle, and therefore accrues a different phase shift at varying distances from the source. Berenger solves this issue by introducing an

anisotropic permeability. Specifically, an artificial permeability μ_r is incorporated into the radial (vertical) derivatives of Maxwell's equations [20, 21]. This technique provides very good results for propagation at a single frequency or over a narrow range of frequencies, and for propagating modes having eigenangles within a certain range.

In his work, Berenger shows good agreement between waveguide mode theory and FDTD calculations for single-frequency propagation from a vertical dipole antenna. He considers typical daytime and nighttime ionosphere conductivity profiles, transitions between day and night, and disturbed conditions during a nuclear burst [17, 21].

2.3   Advantages of FDTD Modeling -- references

Berenger notes in his initial publications on subionospheric propagation [17] that FDTD algorithms offer three primary advantages over previous analytical and frequency domain techniques.   First, FDTD can accommodate continuously varying parameters over the propagation path. In fact, FDTD can, in principle, permit straightforward modeling (with no increase in simulation time) of arbitrary geometrical and electrical horizontal as well as vertical inhomogeneities of the lithosphere and ionosphere.   Previous methods do not offer this capability.

Second, Berenger states that although FDTD is more computationally demanding than frequency-domain mode theory, ongoing improvements in computer resources will continue to decrease FDTD simulation times in the future. Cummer [22] subsequently corroborates this statement in a study involving FDTD–calculated propagation from lightning. He concludes in

[22] that "the simplicity of FDTD propagation modeling and ever-increasing computer power [will] probably make FDTD the technique of the future."

Third, Berenger [17] shows that FDTD "is more versatile than the waveguide method" because it can provide results for general wideband and impulsive applications. This finding is also supported by Cummer's FDTD study of lightning [22], which shows that a "major strength" of FDTD is its automatic calculation of all the fields due to lightning (discharge and post-discharge, evanescent and propagating). Other solution techniques are forced to treat these fields separately[1].

2.4   Overview of Related FDTD studies

Since Berenger's initial FDTD work on subionospheric propagation, several research groups have employed FDTD to study a range of applications, including lightning, global propagation, and Schumann resonances. An overview on each of these topics is provided below.

2.4.1   Lightning

Lightning is the strongest natural source of waves in the 3 Hz – 30 kHz frequency range at the Earth's surface. In [22], Cummer compares FDTD results to mode theory and analytical calculations for propagation in this frequency band from a broadband lightning discharge over a 1000-km lossy ground path. He employs a 2-D cylindrical-coordinate FDTD grid having a PEC ground and an anisotropic but frequency-independent conducting ionosphere (assumes the collision frequency is much higher than the wave frequency at all altitudes). In [22], Cummer

---

[1] **We note here that these claims are strictly speaking applicable only to equivalent wavelengths that are adequately resolved by the FDTD grid.**

obtains "extremely good" agreement between numerical mode theory and FDTD for nighttime spectra below 10 kHz radiated from the lightning source, and a comparable level of agreement for the daytime spectra.

In [23], Hu and Cummer improve the 2-D cylindrical FDTD model described in [22] by treating the ionosphere as a true cold plasma. Their new model includes the effects of charged particles (electrons, positive ions, and negative ions). It also includes an Earth's curvature correction, as well as a surface impedance boundary condition (SIBC) [24, 25] for modeling the lossy ground. As a result, the model of [23] provides improved accuracy to altitudes of up to ~200 km and frequencies up to ~ 30 kHz. Hu and Cummer validate the model of [23] by comparing FDTD calculations to mode theory solutions and broadband experimental data. Specifically, they compare the FDTD model results with experimental data for the frequency spectra of ten sferics radiated from negative lightning discharges at distances of about 629 km. The level of agreement is "very strong" considering the number of uncertainties that prevent a better comparison [23].

Yang and Zhou [26] also employ a 2-D cylindrical coordinate FDTD model to study EM fields very close to lightning channels. They find that the calculated vertical electric (*E*)-field agrees with measurements taken at 15 m distance. Further, the horizontal *E*-field at a distance of 100 m agrees with the Cooray-Rubinstein approximation [27, 28].

Lightning discharges have been associated with complicated phenomena in the lower ionosphere that result in Trimpis, or transient perturbations (amplitude and phase) of subionospheric signals [29]. Two classes of Trimpis exist, both of which have been studied using the FDTD method. The first class is known variously as lightning-induced electron precipitation (LEP) Trimpis, classic Trimpis, or whistler-induced electron precipitation (WEP)

Trimpis. The second class, known as early Trimpis or early/fast Trimpis, are those assumed not caused by lightning-induced electron precipitation because of their very short onset delay after a lightning discharge. This second class includes sprites and elves.

Poussard and Corcuff [30] have studied the first class of Trimpis using the FDTD method. They employ 2-D FDTD models based on Berenger's initial propagation code [19]. However their 2-D FDTD model includes all six field components and no phase information. As a result, Poussard and Corcuff propose a hybrid system involving both FDTD and mode theory to study propagation below 10 kHz, and predict the location, longitudinal extent, and height of disturbed regions associated with the Trimpi events. Their results show good agreement with temporal signatures measured in France for signals arriving from England and the United States.

Hayakawa and Otsuyama [31] have studied the second class of Trimpis using the FDTD method. They use a 2-D FDTD model of a 500-km-long propagation path bounded by a PEC Earth and an ionosphere having an exponential conductivity profile. They first calculate scattering from sprite-induced plasma sheets of varying widths and distances and extending 20 km downwards from the ionosphere. Second, they calculate EM scattering from ionospheric perturbations associated with elves extending 10 km downwards from the ionosphere. These perturbations are assumed to be regions of increased ionization expanding outwards (radially) for 1.5 msec to a total of 450 km, followed by a decay of ionization expanding outwards at the same rate and over the same region. Results in [31] show that scattering at 40 kHz by elves is significantly larger than those from sprites. In fact, the calculated scattering from sprites is so small the authors hypothesize that a weak perturbed region in the ionosphere extending laterally beyond the approximately 40-km-diameter sprite (as observed by optical measurements) must exist.

Finally, specific FDTD techniques to model wave generation by lightning have been published. For example, Sarto creates in [32] an absorbing boundary condition specifically for when the space-cell size is several thousand times smaller than the minimum wavelength, such as for the case of lightning interaction with complex structures. Second, Berenger introduces in [33] a post-processing technique for removing most of the numerical anisotropy of the FDTD mesh when modeling propagation over large distances (> 5000 km). His previous single-frequency correction technique of [17] is not applicable to studies involving broadband lightning. Using the new technique of [33], coarser grids can be used as long as the ratio of the space-cell size to the shortest wavelength is greater than ten. He finds that the time required for post-processing is significantly less than the computational costs of using a finer mesh.

2.4.2   Global Propagation

Hayakawa and Otsuyama [34, 35] have reported a global three-dimensional (3-D) spherical-coordinate, latitude-longitude model of the Earth-ionosphere waveguide based upon fundamental work by Holland [36]. Their grid resolution is 250 x 250 x 2 km, and they assume a PEC ground and typical exponential conductivity profiles for the ionosphere according to [37]. Because they use the same grid as Holland, their model is subject to increasing space-cell eccentricity upon approaching the poles due to converging lines of longitude. This space-cell eccentricity mandates a significant time-step reduction factor for high-resolution grids, since the Courant stability limit is set by the grid's smallest space-cell dimension.

In [31, 34], Hayakawa and Otsuyama simulate a lightning discharge at the Equator having a double-exponential current time-waveform similar to that reported by Bruce and Golde [38]. The calculated radiated waveforms and wave impedances are compared at several distances

(between 5 and 20 Mm) from the source to those predicted by previous analytical formulations [39, 40]. Further, the effect of modeling one-half of the Earth having a daytime ionosphere profile and the other half having a nighttime profile is investigated for both the symmetrical and more realistic tilted cases with respect to the North and South Poles. They observe a shorter time of arrival when nighttime propagation is included in the propagation path. Further, the antipode location is shifted for the tilted case of the day and nighttime profiles [39].

2.4.3 Schumann Resonances

In 1952, W. O. Schumann predicted the resonant frequencies of the Earth-ionosphere cavity below about 100 Hz, which are now called Schumann resonances (SR) [41]. Interest in SRs have increased in recent years because of the apparent correlation between the resonant frequencies and global temperature changes [8], as well as with global lightning activity [42]. Further, SRs can be studied on other planetary bodies to provide information about their atmospheres [43]. To date, FDTD studies of SRs have been conducted by three groups.

The first group, Otsuyama et. al. [44], use the global 3-D model described in [31, 34] and in Section IV to perform FDTD SR calculations. They simulate a lightning strike occurring at the Equator and record the E and magnetic (H) fields at distances between 5 and 20 Mm. Their results show that the size and width of the SR peaks strongly depends on the source-observer distance. Further, they find that the FDTD-calculated SR peaks for the first and second modes are consistent with previous analytical calculations [37, 45].

The second group, Soriano et. al. [46], use an azimuthally-symmetric 3-D spherical-coordinate FDTD model to conduct SR studies. Their model resolution is 1.5° laterally and 5 km vertically, and they assume a PEC ground. First, a lossless Earth-ionosphere cavity is

considered, with a PEC ionosphere boundary at a height of 60 km. Good agreement is obtained between the FDTD-calculated resonances and previous analytical and transmission line matrix (TLM) results [47]. However, because the results differ from actual measurements, Soriano et. al. progress to a more advanced model including losses in the ionosphere. They model the quiet-atmosphere conductivity profiles of [47] and [48] to a height of 100 km. The results obtained using this improved ionosphere model are in much better agreement with those of a semi-analytical two-scale height ionosphere model [49] and with actual measurements.

The third group, Yang and Pasko [50], also study SRs using an azimuthally-symmetric 3-D FDTD model of the Earth-ionosphere cavity. Their model extends to an altitude of 100 km with a resolution of 1,000 x 1,000 x 2.5 km. They assume a PEC ground and test four different ionosphere conductivity profiles: (1) an ideal, free space cavity with a PEC ionosphere boundary; (2) a single-exponential profile [51]; (3) a two-exponential profile using the same scale height for both sections [52 – 54]; and (4) a "knee" profile [e.g. 54]. Yang and Pasko excite their grid with a lightning current source and calculate the first five SR frequencies and associated Q factors from the radial *E*-field power spectrum at a distance of 2 Mm. Good agreement is obtained between the 3-D azimuthally symmetric FDTD model predictions described in [53] and the analytical (mode theory) results of [50].

In [50], Yang and Pasko first show that the "knee" profile provides the most accurate results compared to the theoretical model of Ishaq and Jones [55]. This observation agrees with that of [54], which models of the Earth-ionosphere system require an ionosphere having at least two scale heights in order to achieve realistic SR frequencies and Q-factors. Next, Yang and Pasko study SRs for disturbed conditions associated with solar proton events and X-ray bursts. The solar proton event is modeled as azimuthally symmetric conductivity perturbations at an altitude

of 40 km and centered at the North and South Poles; the X-ray burst is modeled as an azimuthally symmetric conductivity perturbation at an altitude of 70 km and centered only at the North Pole. A discussion follows comparing the FDTD-calculated results with previous reports in the literature [48, 53, 56 – 58].

In [59], Yang and Pasko investigate diurnal and seasonal variations of the power of the first Schumann resonance. For this study, they use a fully 3-D FDTD model of the Earth-ionosphere waveguide (i.e. no longer azimuthally symmetric) having an ionospheric conductivity profile derived from the International Reference Ionosphere (IRI) [60] above 60 km. The overall behavior of the calculated FDTD results agrees well with the experimental data of [61] for when the modeled lightning source location is varied between the three major lightning storm regions of the world (South-East Asia, Africa, South America) depending on the time of day, and the receiver is located in the Negev Desert, Israel [59].

In [62], Yang and Pasko investigate SRs on other planetary bodies, including Titan (Saturn's largest moon), Mars, and Venus. Understanding SRs on planets such as Titan could help support the existence of electrical discharges and provide other useful information regarding its lower atmosphere. For their FDTD model, conductivity profiles are derived from previously reported models, and their results are compared to previously reported calculations [e.g. 43].

2.5 Goals of this Work

This dissertation addresses FDTD modeling of the global Earth-ionosphere waveguide using a fully 3-D grid extending from 100 km below sea level to an altitude of 100 km and having a nominal resolution on the order of one to tens of kilometers in all three directions. These models enable a direct, full-vector, 3-D time-domain Maxwell's equations calculation of electromagnetic

wave propagation within the lithosphere-ionosphere cavity due to an arbitrary excitation. Furthermore, they can account for arbitrary horizontal as well as vertical geometrical and electrical inhomogeneities and anisotropies of the ionosphere, lithosphere, oceans, and Earth's magnetic field. And finally, they can permit inclusion of 3-D gyrotropic ionosphere plasma as influenced by the Earth's magnetic field. This level of detail and resolution has not existed in any previously analytical or numerical model, as can be seen in the literature review of Sections 2.1 – 2.4.

The specific aims of the work described in this dissertation are to apply detailed 3-D FDTD models of the Earth-ionosphere cavity to four applications. The goal of the first application is to test whether tectonic stresses at crustal plate boundaries precursory to major earthquakes can generate EM "signatures" detectable above the natural noise background due primarily to lightning. Such knowledge could possibly lead to useful information regarding to earthquake predictions and warnings. The goal of the second application is to develop a global remote-sensing system that could rapidly and inexpensively survey thousands of square km for significant oil and mineral resource deposits. The goal of the third application is to develop an advanced remote-sensing system for locating and characterizing local ionospheric anomalies within about 100 km of the Earth's surface. The goal of the fourth application is to advance the understanding of electromagnetic radiation from lightning and sprites under different conditions of the Earth's magnetic field and ionosphere.

In the following chapter, the development of two generations of FDTD models used for the above studies is described: the first having grid cells formed by lines of longitude and latitude, and the second having a geodesic grid-cell arrangement comprised of hexagons and pentagons.

3   FDTD Gridding Schemes for Spherical Waveguides

3.1   Introduction to FDTD Maxwell's Equations Modeling

Maxwell's equations are the foundation of classical electromagnetic theory. For linear, isotropic, nondispersive, lossy materials, Maxwell's curl equations in MKS units are:

$$\frac{\partial \vec{H}}{\partial t} = -\frac{1}{\mu}\nabla \times \vec{E} - \frac{1}{\mu}\left(\vec{M}_{source} + \sigma^* \vec{H}\right) \tag{1}$$

$$\frac{\partial \vec{E}}{\partial t} = \frac{1}{\varepsilon}\nabla \times \vec{H} - \frac{1}{\varepsilon}\left(\vec{J}_{source} + \sigma \vec{E}\right) \tag{2}$$

where $\vec{E}$ and $\vec{H}$ are the electric and magnetic field vectors, respectively, $\vec{J}$ is the current density vector, $\vec{M}$ is the equivalent magnetic current density, ε is the electrical permittivity, σ is the electric conductivity, and σ^* is the equivalent magnetic loss.

Writing out the vector components of equations (1) and (2) yields a system of six coupled scalar partial differential equations. In 1966, Yee introduced a finite-differencing scheme for solving these six equations [63]. His formulation is the basis of what is now called the FDTD method [64]. Today, the FDTD method is one of the most widely-used numerical methods for electromagnetic problems. It is discussed in detail elsewhere [14], and will not be repeated here.

3.2   Latitude-Longitude Grid-Cell Arrangement

This Section describes the FDTD algorithm used to model the global Earth-ionosphere waveguide wherein grid cells follow lines of latitude and longitude. Similar to the model developed by Otsuyama and Hayakawa [31, 34] described in Section 2.4.2, this model is based

upon the fundamental work by Holland [36]. However, unlike the Otsuyama and Hayakawa model, the FDTD grid employed here includes a means to reduce the eccentricity of the cells in the polar regions by a novel adaptive cell-combining technique applied to adjacent grid-cells in the West-East direction. This technique permits maintenance of the time-step at nearly the level allowed by the Courant stability condition for the square equatorial cells, yielding a greatly improved computational efficiency relative to conventional spherical-coordinate formulations.

3.2.1   2-D Model

In preparation for a fully 3-D model, the complete spherical surface of the Earth is first mapped onto a logically Cartesian, two-dimensional, $2M \times M$ -cell, transverse magnetic (TM) FDTD grid, where M is a power of 2 [65, 66]. Fig. 1 illustrates the general layout of the grid. The grid-cell position index in the West-to-East direction is $1 \leq i \leq 2M$, and the grid-cell position index in the south-to-north direction is $1 \leq j \leq M$. Note that the grid cells follow along lines of constant latitude, $\theta = \text{constant}$, where θ is the usual spherical angle measured from the North Pole; and along lines of constant longitude, $\phi = \text{constant}$, where ϕ is the usual spherical azimuthal angle measured from a specified prime meridian. In this manner, the grid shown in Fig. 1 is comprised of planar isosceles trapezoidal cells away from the North and South Poles (Fig. 2a), and planar isosceles triangular cells at the Poles (Fig. 2b).

The same angular increment is chosen in latitude, $\Delta\theta = \pi/m$, for each cell in the grid. Thus, the south-north span of each trapezoidal or triangular grid cell is $\Delta_{\text{s}-\text{n}} = \pi R_{\text{E}}/m$, where R_{E} is the Earth's radius. To maintain square or nearly square grid cells near the equator, a baseline value of the angular increment in longitude, $\Delta\phi$, is selected to equal $\Delta\theta$. However,

this causes the West-East span of each cell, $\Delta_{w-e} = R_E \, \Delta\phi \sin\theta$, to be a function of θ. This could be troublesome for cells near the North and South Poles where $\theta \to 0$ and $\theta \to \pi$, respectively. There, the geometrical eccentricity of each cell, $\Delta_{s-n}/\Delta_{w-e} = \Delta\theta/(\Delta\phi \sin\theta)$, would become quite large, and the numerical stability and efficiency of the FDTD algorithm would be degraded. Fig. 3 illustrates a means to mitigate this problem by merging pairs of adjacent cells in the West-East direction, effectively halving the cell eccentricity. This process can be repeated several times as the grid approaches a Pole, allowing the user to specify a maximum allowable cell eccentricity.
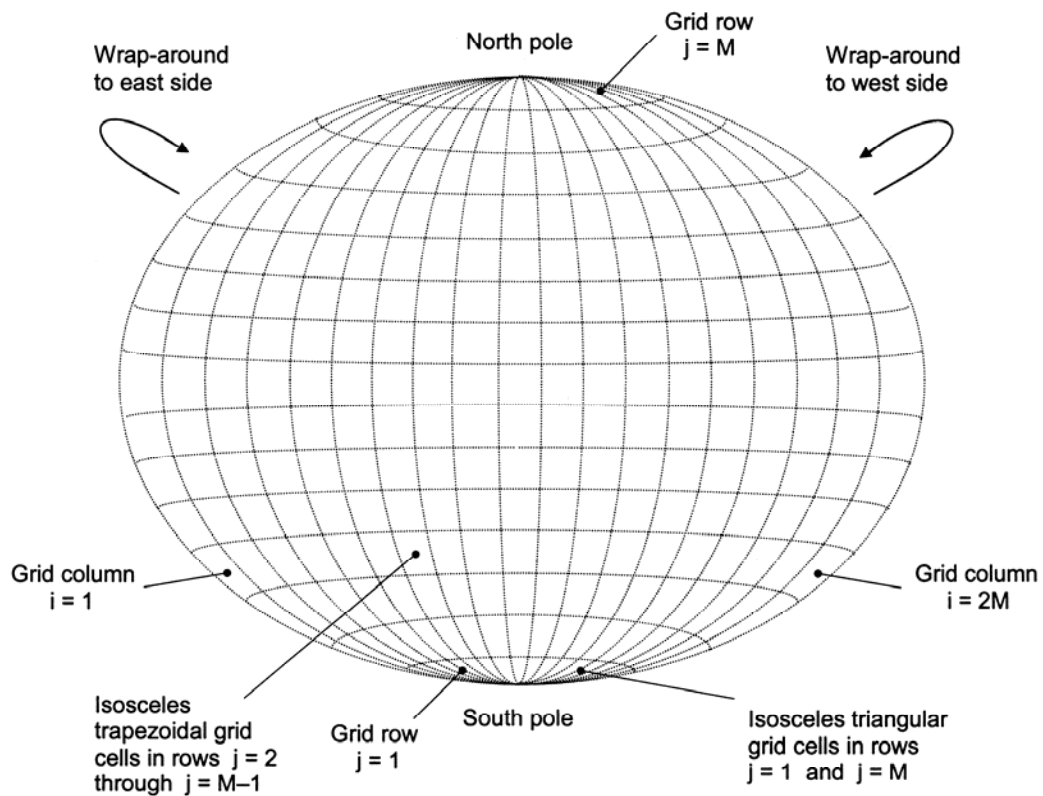
Figure 1 General layout of the of the three-dimensional FDTD lattice covering the complete Earth-sphere as seen in a TM plane at a constant radial coordinate.

(a)

(b)
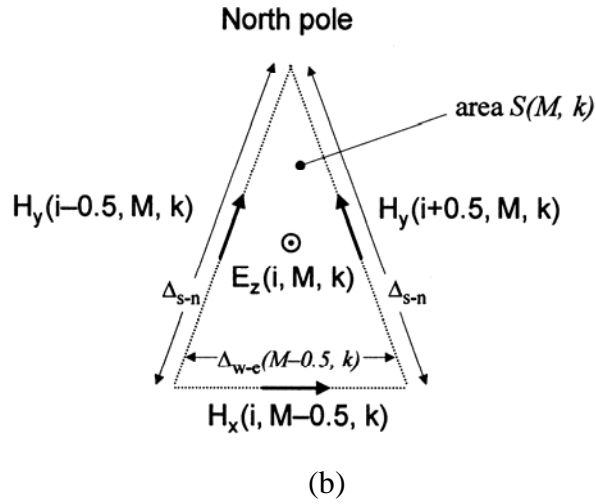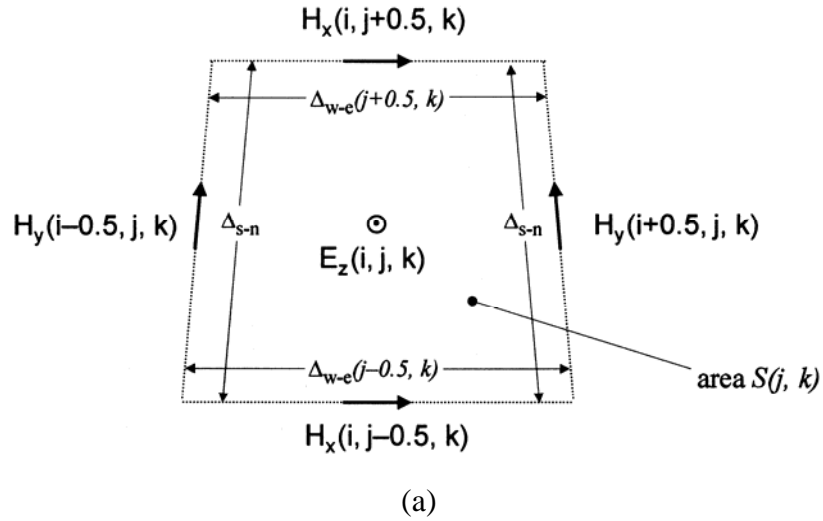
Figure 2 Details of the TM$_z$-plane lattice-cell geometry: (a) isosceles trapezoidal cell in the northern hemisphere away from the North Pole; (b) isosceles triangular cell at the North Pole.
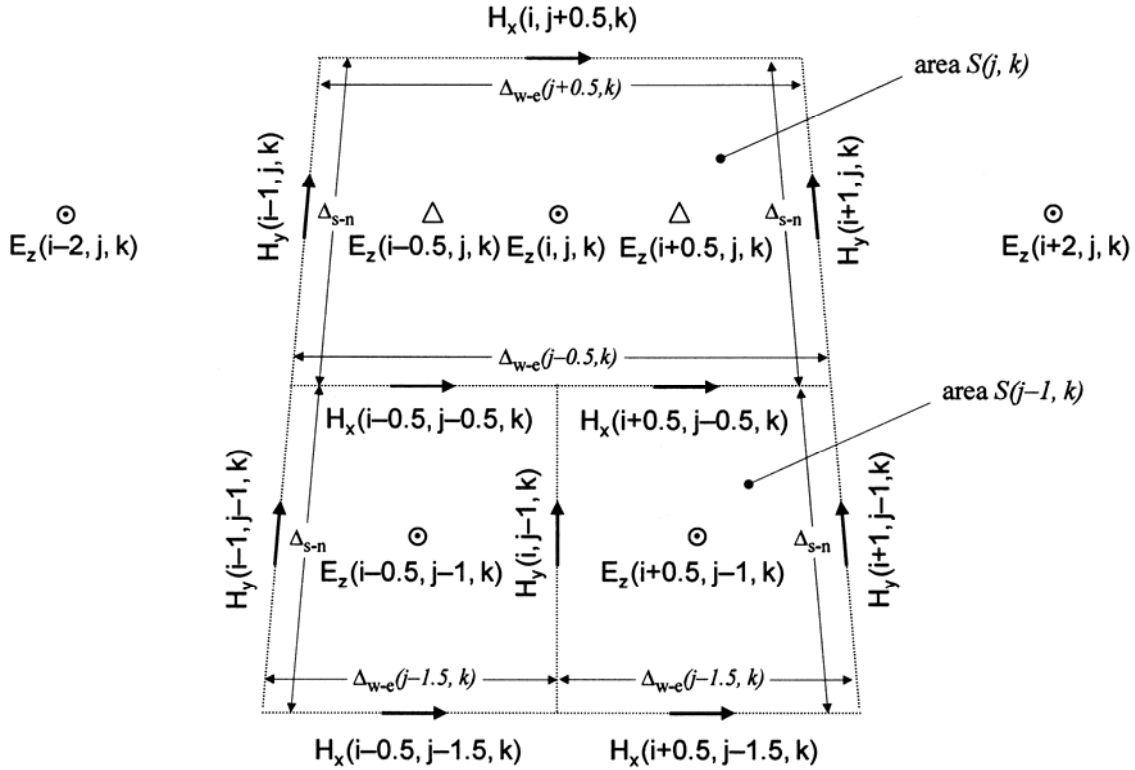
Figure 3   Details of the TM$_z$-plane grid-cell geometry in the northern hemisphere at the

transition between two adjacent regular cells and a single cell spanning twice

the distance in the West-East direction.

The wrap-around or joining of the grid is along a specific line of constant longitude, or meridian. This joining is, in effect, a periodic boundary condition applied at each *j*-row of grid cells, whether trapezoids or triangles.

The complete FDTD algorithm for the 2-D latitude-longitude spherical Earth grid is presented in [65]. Because this algorithm is incorporated into the fully 3-D formulation presented in the following Section, only the 2-D modeling results will be presented here.

First, the accuracy of the 2-D FDTD numerical model is tested using an impulsive circular cylindrical wave. The idea here is to track the wave in time and space as it propagates radially outward from a filamentary current source, travels completely around the earth-sphere model, and then propagates radially inward to the antipode. Results are obtained for a 1024×512 lossless grid spanning the Earth-sphere and using a time step of 32.6 μsec.
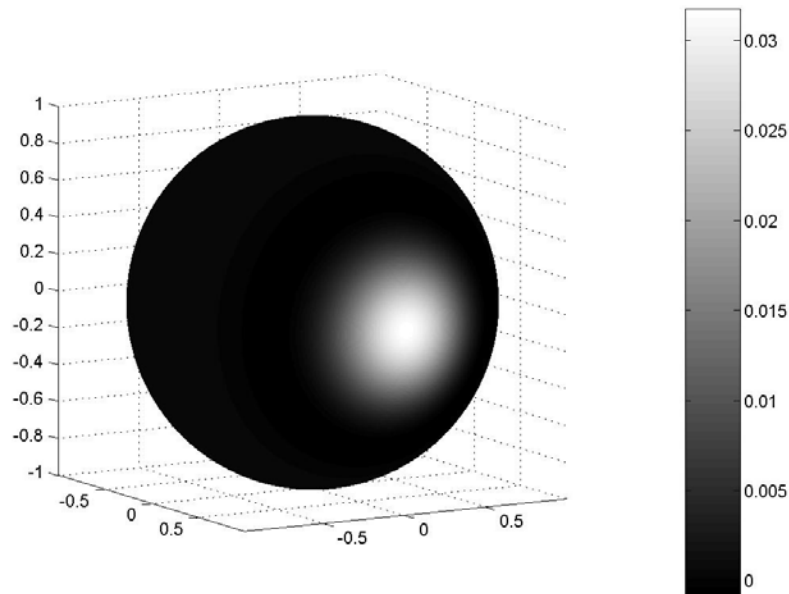
Figure 4   Grey-scale visualization of the electric field projected onto the surface of the

Earth-sphere at the time of its initial peak value at the antipode.

Fig. 4 is a gray-scale visualization of the electric field projected onto the surface of the Earth-sphere at the time of its initial peak value at the antipode. Fig. 5 is a gray-scale visualization of the electric field in the region immediately surrounding the antipode at the time

of its initial peak value. The high degree of azimuthal symmetry seen in these two figures is a measure of the isotropy of the numerical wave propagation within the model. Note that this propagation occurs concurrently through both simple, uniform grid regions near the equator and more complicated polar regions having a nonuniform mesh of cells with variable eccentricity, mergers, and transitions from trapezoids to triangles and back to trapezoids.

Fig. 6 graphs the calculated time-waveform of the electric field at the antipode for the first two circumnavigations of the Earth-sphere. This figure shows the 180° phase reversals of the electric-field at the antipode first calculated by Wait [4]. Further, Fig. 6 shows a 0.134-second circumnavigation period, corresponding to a fundamental Earth resonance of 7.46 Hz.
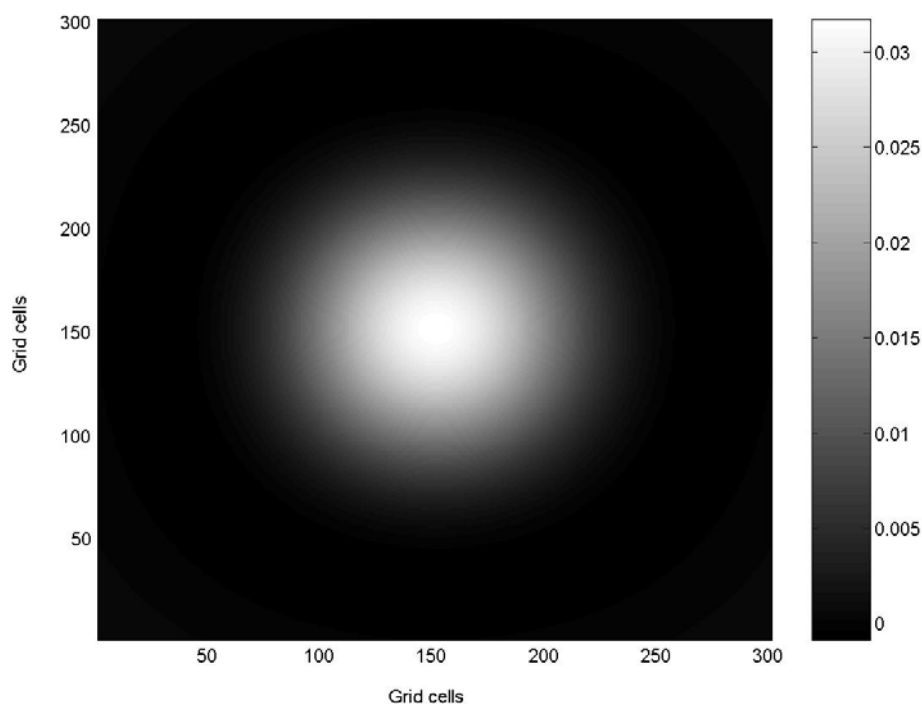
Figure 5 Grey-scale visualization of the electric field in the region immediately surrounding the antipode at the time of its initial peak value.
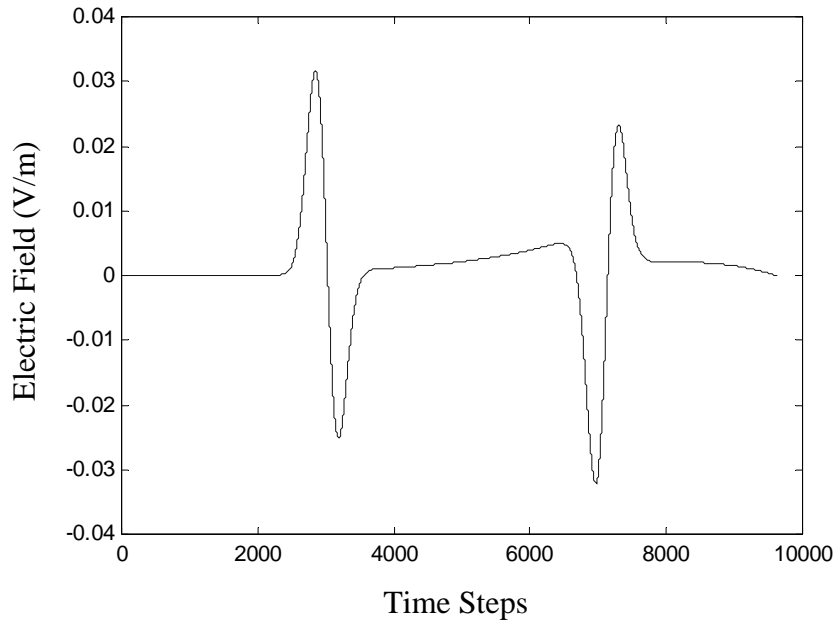
Figure 6 Calculated time-waveform of the electric field at the antipode for the first two circumnavigations of the Earth-sphere.

3.2.2 3-D Model

The 2-D work of Section 3.2.1 is expanded here to create a fully 3-D FDTD model of the entire Earth-ionosphere cavity extending between ±100 km of sea level [66, 67]. This 3-D space lattice has a nominal resolution of 40 x 40 x 5 km at the Equator, but it is constructed to permit variable cell size in the radial (vertical) direction. This cell size is a compromise choice to meet the following set of requirements: (1) limit the space-lattice size to permit its residence in memory on our laboratory's 2-GB workstation; (2) resolve ELF wavelengths of 800 km or greater (frequencies of 375 Hz or less) with 20 or more cells per wavelength; and (3) provide one-to-two cell resolution for the radial extent (height and depth) of the Earth's oceans and mountain ranges.

The complete 3-D model is comprised of alternating planes of TM and transverse electric (TE) field components in the radial direction. Each TM plane is of the type discussed in Section 3.2.1 and shown in Fig. 1. That is, the TM planes are comprised of isosceles trapezoidal and isosceles triangular cells (Figs. 2a and 2b). Similarly, each TE plane at a constant radial coordinate is comprised of isosceles trapezoidal cells away from the North and South Poles (Fig. 7a), and a polygon cell at each Pole (Fig. 7b). Adjacent TE and TM planes are then coupled together via regular Yee-type updates. Below, the FDTD algorithm is provided for each of the six field components of the 3-D latitude-longitude FDTD grid.

Basic Algorithm, TM_z Components

Ampere's Law in integral form [14] can be applied to develop an FDTD time-stepping relation for the electric field E_z at the center of the (i, j, k)'th trapezoidal grid cell. For example, referring to Fig. 2a, we have

$$E_z^{n+1}(i, j, k) = E_z^n(i, j, k)$$

$$+ \frac{\Delta t}{\varepsilon_0 \, S(j, k)} \left\{ \begin{array}{l} H_x^{n+0.5}(i, \, j-0.5, \, k) \, \Delta_{\text{w}-\text{e}}(j-0.5, \, k) - \\ H_x^{n+0.5}(i, \, j+0.5, \, k) \, \Delta_{\text{w}-\text{e}}(j+0.5, \, k) + \\ \left[H_y^{n+0.5}(i+0.5, \, j, \, k) - H_y^{n+0.5}(i-0.5, \, j, \, k) \right] \Delta_{\text{s}-\text{n}} \end{array} \right\} \tag{3}$$

where Δt is the time-step and

$$\Delta_{\text{w}-\text{e}}(j+0.5, \, k) = R \, \Delta\phi \, \sin\left[(M-j)\pi/M\right] \tag{4a}$$

$$\Delta_{\text{w}-\text{e}}(j-0.5, \, k) = R \, \Delta\phi \, \sin\left[(M-j+1)\pi/M\right] \tag{4b}$$

$$S(j, k) = \left[\Delta_{\text{w}-\text{e}}(j-0.5, \, k) + \Delta_{\text{w}-\text{e}}(j+0.5, \, k)\right] \Delta_{\text{s}-\text{n}} / 2 \tag{4c}$$

$E_x(i+0.5, j+1, k+0.5)$

$\Delta_{w-e}(j+1, k+0.5)$

$E_y(i, j+0.5, k+0.5)$ Δ_{s-n} ⊙ Δ_{s-n} $E_y(i+1, j+0.5, k+0.5)$

$H_z(i+0.5, j+0.5, k+0.5)$

$\Delta_{w-e}(j, k+0.5)$

area $S(j+0.5, k+0.5)$

$E_x(i+0.5, j, k+0.5)$

(a)

$E_x(N-0.5, M, k+0.5)$ $E_x(3.5, M, k+0.5)$

area $S(M+0.5, k+0.5)$

North pole
⊙
$H_z(0.5, M+0.5, k+0.5)$

$E_x(0.5, M, k+0.5)$ $E_x(2.5, M, k+0.5)$

$\Delta_{w-e}(M-0.5, k+0.5)$

$E_x(1.5, M, k+0.5)$
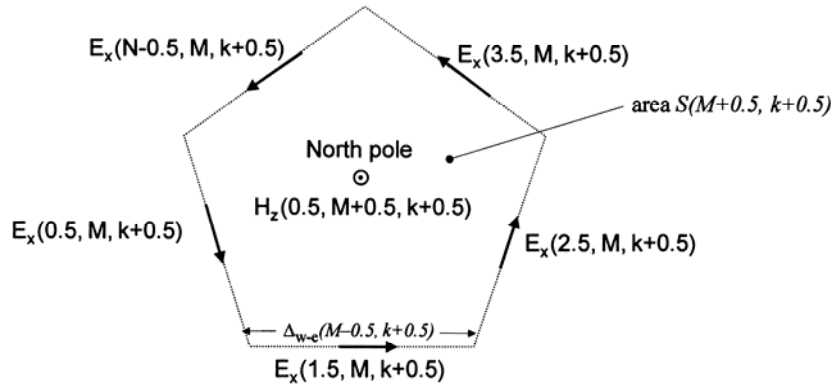
(b)

Figure 7 Details of the TE_z-plane lattice-cell geometry: (a) isosceles trapezoidal cell in the northern hemisphere away from the North Pole; (b) polygon cell directly at the North Pole.

Similarly, referring to Fig. 2b, the update for E_z at the center of the i'th triangular grid cell at the north pole ($j = M$) is given by

$$E_z^{n+1}(i,\,M,\,k) = E_z^n(i,\,M,\,k)$$
$$+ \frac{\Delta t}{\varepsilon_0\,S(M,\,k)} \left\{ \begin{array}{l} H_x^{n+0.5}(i,\,M-0.5,\,k)\,\Delta_{w-e}(M-0.5,\,k) + \\ \left[H_y^{n+0.5}(i+0.5,\,M,\,k) - H_y^{n+0.5}(i-0.5,\,M,\,k) \right] \Delta_{s-n} \end{array} \right\} \quad (5)$$

where $\Delta_{w-e}(M-0.5,\,k)$ is given by (2b) for the case $j = M$, and

$$S(M,\,k) = \frac{\Delta_{w-e}(M-0.5,\,k)\,\Delta_{s-n}}{2}\,\sin\left\{\cos^{-1}\left[\frac{\Delta_{w-e}(M-0.5,\,k)}{2\,\Delta_{s-n}}\right]\right\} \quad (6)$$

Expressions analogous to (5) and (6) can be derived for the i'th triangular grid cell at the south pole ($j = 1$).

The basic FDTD time-stepping algorithm is completed by specifying the updates for the H_x and H_y fields. For example, referring to the trapezoidal grid cell shown in Fig. 2a, we have

$$H_x^{n+1.5}(i,\,j-0.5,\,k) = H_x^{n+0.5}(i,\,j-0.5,\,k)$$
$$+ \frac{\Delta t}{\mu_0\,\Delta_r}\left[E_y^{n+1}(i,\,j-0.5,\,k+0.5) - E_y^{n+1}(i,\,j-0.5,\,k-0.5) \right] \quad (7)$$
$$+ \frac{\Delta t}{\mu_0\,\Delta_{s-n}}\left[E_z^{n+1}(i,\,j-1,\,k) - E_z^{n+1}(i,\,j,\,k) \right]$$

$$H_y^{n+1.5}(i+0.5,\,j,\,k) = H_y^{n+0.5}(i+0.5,\,j,\,k)$$
$$+ \frac{\Delta t}{\mu_0\,\Delta_r}\left[E_x^{n+1}(i+0.5,\,j,\,k-0.5) - E_x^{n+1}(i+0.5,\,j,\,k+0.5) \right] \quad (8)$$
$$+ \frac{\Delta t}{\mu_0\,\Delta_{w-e}(j,\,k)}\left[E_z^{n+1}(i+1,\,j,\,k) - E_z^{n+1}(i,\,j,\,k) \right]$$

where Δ_r is the cell span in the radial direction.

For a triangular grid cell at the north pole ($j = M$) shown in Fig. 2b, we similarly have

$$H_x^{n+1.5}(i,\,M-0.5,\,k) = H_x^{n+0.5}(i,\,M-0.5,\,k)$$

$$+\frac{\Delta t}{\mu_0\,\Delta_{\mathrm{r}}}\left[E_y^{n+1}(i,\,M-0.5,\,k+0.5)-E_y^{n+1}(i,\,M-0.5,\,k-0.5)\right] \qquad (9)$$

$$+\frac{\Delta t}{\mu_0\,\Delta_{\mathrm{s-n}}}\left[E_z^{n+1}(i,\,M-1,\,k)-E_z^{n+1}(i,\,M,\,k)\right]$$

$$H_y^{n+1.5}(i+0.5,\,M,\,k) = H_y^{n+0.5}(i+0.5,\,M,\,k)$$

$$+\frac{\Delta t}{\mu_0\,\Delta_{\mathrm{r}}}\left[E_x^{n+1}(i+0.5,\,M,\,k-0.5)-E_x^{n+1}(i+0.5,\,M,\,k+0.5)\right] \qquad (10)$$

$$+\frac{\Delta t}{\mu_0\,\Delta_{\mathrm{w-e}}(M,\,k)}\left[E_z^{n+1}(i+1,\,M,\,k)-E_z^{n+1}(i,\,M,\,k)\right]$$

Expressions analogous to (9) and (10) can be derived for a triangular grid cell at the south pole ($j=1$).

Merging Trapezoidal Grid Cells Approaching the Polar Regions

As stated earlier, near the north and south poles the geometrical eccentricity of each trapezoidal cell, $\Delta_{\mathrm{s-n}}/\Delta_{\mathrm{w-e}} = \Delta\theta/(\Delta\phi\sin\theta)$, can become quite large for a constant value of $\Delta\phi$, thereby degrading the numerical stability and efficiency of the FDTD algorithm. Fig. 3 illustrates a means to mitigate this problem by merging pairs of adjacent cells of the TM plane in the west-east direction, effectively halving the cell eccentricity. This process can be repeated several times as the grid approaches a pole, allowing the user to specify a maximum allowable cell eccentricity.

The required algorithm is now presented. Again applying Ampere's Law in integral form, the FDTD time-stepping relation for the E_z field at the center of the merged cell is given by

$$E_z^{n+1}(i, j, k) = E_z^n(i, j, k)$$

$$+ \frac{\Delta t}{\varepsilon_0 S(j, k)} \left\{ \begin{array}{l} H_x^{n+0.5}(i-0.5, \; j-0.5, \; k) \; \Delta_{\text{w-e}}(j-0.5, \; k)/2 + \\[4pt] H_x^{n+0.5}(i+0.5, \; j-0.5, \; k) \; \Delta_{\text{w-e}}(j-0.5, \; k)/2 - \\[4pt] H_x^{n+0.5}(i, \; j+0.5, \; k) \; \Delta_{\text{w-e}}(j+0.5, \; k) + \\[4pt] \left[H_y^{n+0.5}(i+1, \; j, \; k) - H_y^{n+0.5}(i-1, \; j, \; k) \right] \Delta_{\text{s-n}} \end{array} \right\} \tag{11}$$

The following E_z fields within the merged cell, required for the subsequent magnetic-field updates, are obtained by linearly interpolating the E_z field quantities calculated in (9):

$$E_z^{n+1}(i-0.5, \; j, \; k) = \left[3 E_z^{n+1}(i, \; j, \; k) + E_z^{n+1}(i-2, \; j, \; k) \right] / 4 \tag{12a}$$

$$E_z^{n+1}(i+0.5, \; j, \; k) = \left[3 E_z^{n+1}(i, \; j, \; k) + E_z^{n+1}(i+2, \; j, \; k) \right] / 4 \tag{12b}$$

Now, the time-stepping algorithm for the merged cell can be completed by specifying the updates for the H_x and H_y fields at the periphery of the cell, for example:

$$\begin{aligned} H_x^{n+1.5}(i-0.5, \; j-0.5, \; k) \; = \; & H_x^{n+0.5}(i-0.5, \; j-0.5, \; k) \\[6pt] & + \frac{\Delta t}{\mu_0 \Delta_{\text{r}}} \left[\begin{array}{l} E_y^{n+1}(i-0.5, \; j-0.5, \; k+0.5) - \\ E_y^{n+1}(i-0.5, \; j-0.5, \; k-0.5) \end{array} \right] \\[6pt] & + \frac{\Delta t}{\mu_0 \Delta_{\text{s-n}}} \left[E_z^{n+1}(i-0.5, \; j-1, \; k) - E_z^{n+1}(i-0.5, \; j, \; k) \right] \end{aligned} \tag{13}$$

$$\begin{aligned} H_x^{n+1.5}(i+0.5, \; j-0.5, \; k) = \; & H_x^{n+0.5}(i+0.5, \; j-0.5, \; k) \\[6pt] & + \frac{\Delta t}{\mu_0 \Delta_{\text{r}}} \left[\begin{array}{l} E_y^{n+1}(i+0.5, \; j-0.5, \; k+0.5) - \\ E_y^{n+1}(i+0.5, \; j-0.5, \; k-0.5) \end{array} \right] \\[6pt] & + \frac{\Delta t}{\mu_0 \Delta_{\text{s-n}}} \left[E_z^{n+1}(i+0.5, \; j-1, \; k) - E_z^{n+1}(i+0.5, \; j, \; k) \right] \end{aligned} \tag{14}$$

$$H_y^{n+1.5}(i+1,\ j,\ k) = H_y^{n+0.5}(i+1,\ j,\ k)$$

$$+ \frac{\Delta t}{\mu_0\,\Delta_r}\left[E_x^{n+1}(i+1,\ j,\ k-0.5) - E_x^{n+1}(i+1,\ j,\ k+0.5)\right] \qquad (15)$$

$$+ \frac{\Delta t}{\mu_0\,\Delta_{w-e}(j,\ k)}\left[E_z^{n+1}(i+2,\ j,\ k) - E_z^{n+1}(i,\ j,\ k)\right]$$

$$H_x^{n+1.5}(i,\ j+0.5,\ k) = H_x^{n+0.5}(i,\ j+0.5,\ k)$$

$$+ \frac{\Delta t}{\mu_0\,\Delta_r}\left[E_y^{n+1}(i,\ j+0.5,\ k+0.5) - E_y^{n+1}(i,\ j+0.5,\ k-0.5)\right] \qquad (16)$$

$$+ \frac{\Delta t}{\mu_0\,\Delta_{s-n}}\left[E_z^{n+1}(i,\ j,\ k) - E_z^{n+1}(i,\ j+1,\ k)\right]$$

West-East Grid Wrap-Around (Periodic Boundary Condition)

The grid wrap-around (periodic boundary condition) in the west-east direction completes the FDTD algorithm for the TM components. For each row j of grid column $i = 1$ in Fig. 1, this is implemented by the following special time-stepping relation for H_y at the west boundary of the grid:

$$H_y^{n+1.5}(0.5,\ j,\ k) = H_y^{n+0.5}(0.5,\ j,\ k)$$

$$+ \frac{\Delta t}{\mu_0\,\Delta_r}\left[E_y^{n+1}(0.5,\ j,\ k-0.5) - E_y^{n+1}(0.5,\ j,\ k+0.5)\right] \qquad (17a)$$

$$+ \frac{\Delta t}{\mu_0\,\Delta_{w-e}(j,\ k)}\left[E_z^{n+1}(1,\ j,\ k) - E_z^{n+1}(2M,\ j,\ k)\right]$$

Upon obtaining each such H_y value, the grid wrap-around is completed by implementing the following special relation for each row j of grid column $i = 2M$ for H_y at the east boundary of the grid:

$$H_y^{n+1.5}(2M+0.5,\ j,\ k) = H_y^{n+1.5}(0.5,\ j,\ k) \qquad (17b)$$

Steps (17a) and (17b) apply to all grid rows, whether containing trapezoidal or triangular cells.

Basic Algorithm, TE$_z$ Components

Similarly, Faraday's Law in integral form [14] can be applied to develop an FDTD time-stepping relation for the electric field H_z at the center of the $(i+0.5, j+0.5, k+0.5)$'th trapezoidal grid cell. For example, referring to Fig. 7a, we have
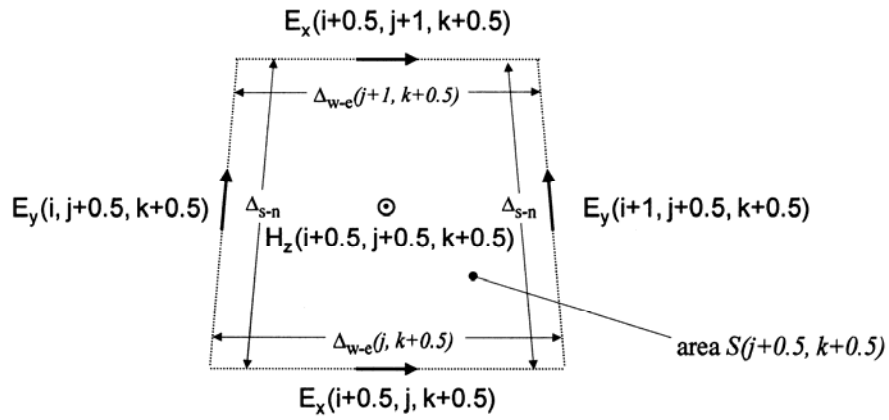
$$H_z^{n+1.5}(i+0.5, j+0.5, k+0.5) = H_z^{n+0.5}(i+0.5, j+0.5, k+0.5)$$

$$+ \frac{\Delta t}{\mu_0 S(j+0.5, k+0.5)} \left\{ \begin{array}{l} E_x^n(i+0.5, j+1, k+0.5) \, \Delta_{w-e}(j+1, k+0.5) - \\ E_x^n(i+0.5, j, k+0.5) \, \Delta_{w-e}(j, k+0.5) + \\ \left[\begin{array}{l} E_y^n(i, j+0.5, k+0.5) - \\ E_y^n(i+1, j+0.5, k+0.5) \end{array} \right] \Delta_{s-n} \end{array} \right\}$$

$$(18)$$

Similarly, referring to Fig. 7b, the update for H_z directly at the north pole $(i = 0.5, j = M+0.5)$ is given by

$$H_z^{n+1.5}(0.5, M+0.5, k+0.5) = H_z^{n+0.5}(0.5, M+0.5, k+0.5)$$

$$- \frac{\Delta t}{\mu_0 S(M+0.5, k+0.5)} \left\{ \sum_{X=1}^{N} E_x^n(X-0.5, M, k+0.5) \, \Delta_{w-e}(M, k+0.5) \right\} \qquad (19)$$

where $\Delta_{w-e}(M, k+0.5)$ is given by (4b) for the case $j = M$, N is the number of E_x components surrounding the H_z component directly at the pole, and

$$S(M+0.5, k+0.5) = \frac{N \, \Delta_{w-e}(M, k+0.5)^2}{4 \tan (\pi / N)} \qquad (20)$$

Expressions analogous to (19) and (20) can be derived for H_z directly at the south pole $(i = 0.5, j = 0.5)$.

The basic FDTD time-stepping algorithm is completed by specifying the updates for the E_x and E_y fields. For example, referring to the trapezoidal grid cell shown in Fig. 7a, we have

$$E_x^{n+1}(i+0.5,\ j,\ k+0.5) = E_x^n(i+0.5,\ j,\ k+0.5)$$

$$+\frac{\Delta t}{\varepsilon_0\,\Delta_r}\left[H_y^{n+0.5}(i+0.5,\ j,\ k) - H_y^{n+0.5}(i+0.5,\ j,\ k+1)\right] \qquad (21)$$

$$+\frac{\Delta t}{\varepsilon_0\,\Delta_{s-n}}\left[\begin{array}{l}H_z^{n+0.5}(i+0.5,\ j+0.5,\ k+0.5) - \\ H_z^{n+0.5}(i+0.5,\ j-0.5,\ k+0.5)\end{array}\right]$$

$$E_y^{n+1}(i,\ j+0.5,\ k+0.5) = E_y^n(i,\ j+0.5,\ k+0.5)$$

$$+\frac{\Delta t}{\varepsilon_0\,\Delta_r}\left[H_x^{n+0.5}(i,\ j+0.5,\ k+1) - H_x^{n+0.5}(i,\ j+0.5,\ k)\right] \qquad (22)$$

$$+\frac{\Delta t}{\varepsilon_0\,\Delta_{w-e}(j+0.5,\ k+0.5)}\left[\begin{array}{l}H_z^{n+0.5}(i-0.5,\ j+0.5,\ k+0.5) - \\ H_z^{n+0.5}(i+0.5,\ j+0.5,\ k+0.5)\end{array}\right]$$

Merging Trapezoidal Grid Cells Approaching the Polar Regions

As stated earlier, near the north and south poles the geometrical eccentricity of each trapezoidal cell, $\Delta_{s-n}/\Delta_{w-e} = \Delta\theta/(\Delta\phi\sin\theta)$, can become quite large for a constant value of $\Delta\phi$, thereby degrading the numerical stability and efficiency of the FDTD algorithm. Fig. 8 illustrates a means to mitigate this problem by merging pairs of adjacent cells in the TE plane in the west-east direction, effectively halving the cell eccentricity as for the TM case. This process can be repeated several times as the grid approaches a pole, allowing the user to specify a maximum allowable cell eccentricity.

The required algorithm is now presented. The following E_x field at the boundary of the merged cell, required for the subsequent magnetic-field update, is obtained by linearly interpolating the E_x field quantities:

$$E_x^{n+1}(i+0.5,\ j+1,\ k+0.5) = \left[\begin{array}{l}E_x^n(i-0.5,\ j+1,\ k+0.5) + \\ E_x^n(i+1.5,\ j+1,\ k+0.5)\end{array}\right] / 2 \qquad (23)$$
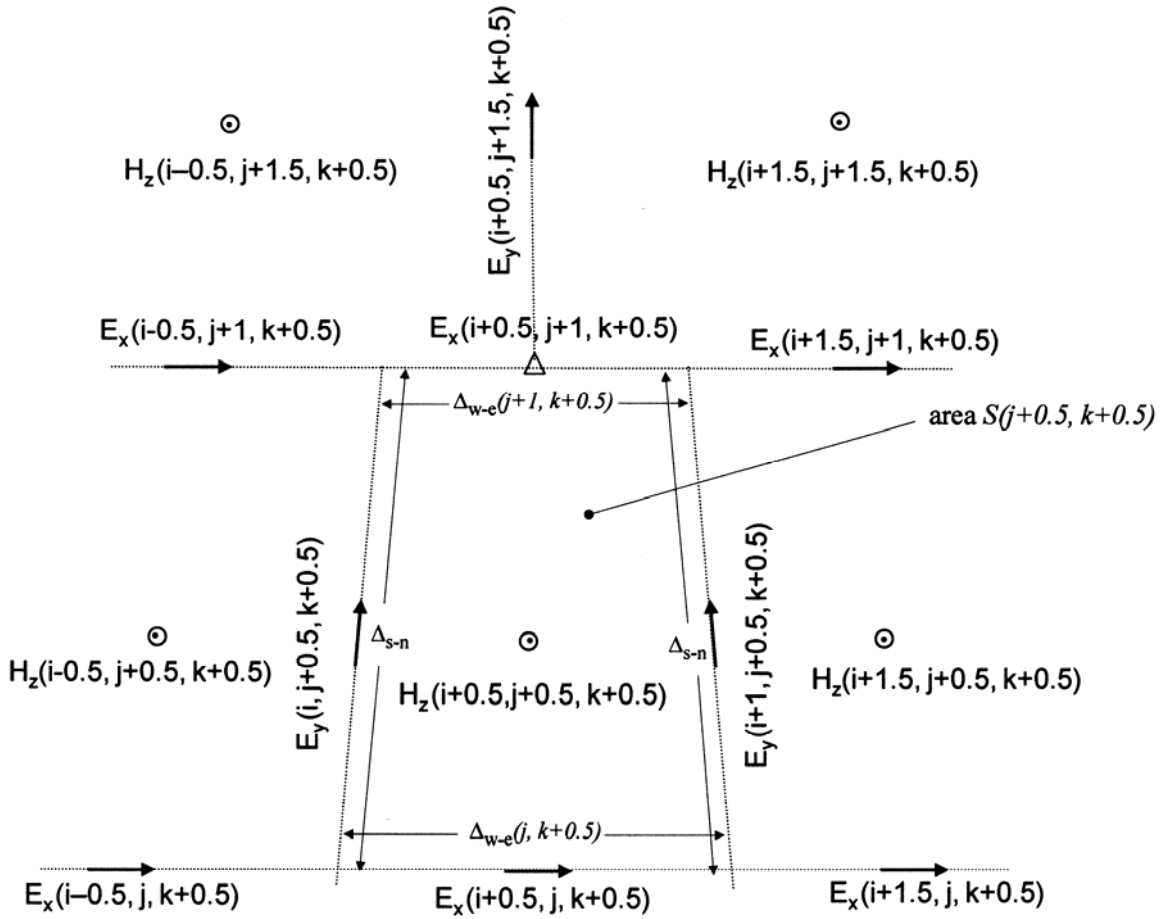
Figure 8   Details of the TE$_z$-plane grid-cell geometry in the northern hemisphere at the transition between three adjacent regular cells and two cells each spanning twice the distance in the West-East direction.

Applying Faraday's Law in integral form, the FDTD time-stepping relation for the H_z field below the center of the merged cell is then given by

$$H_z^{n+1.5}(i+0.5,\ j+0.5,\ k+0.5) = H_z^{n+0.5}(i+0.5,\ j+0.5,\ k+0.5)$$

$$(24)$$

$$+\frac{\Delta t}{\mu_0\ S(j+0.5,\ k+0.5)}\left\{\begin{array}{l} E_x^n(i+0.5,\ j+1,\ k+0.5)\ \Delta_{\text{w-e}}(j+1,\ k+0.5)-\\ E_x^n(i+0.5,\ j,\ k+0.5)\ \Delta_{\text{w-e}}(j,\ k+0.5)+\\ \left[\begin{array}{l} E_y^n(i,\ j+0.5,\ k+0.5)-\\ E_y^n(i+1,\ j+0.5,\ k+0.5)\end{array}\right]\Delta_{\text{s-n}}\end{array}\right\}$$

The time-stepping algorithm for the merged cell can be completed by specifying the updates for the E_x and E_y fields at the periphery of the cell. For example, the following algorithm is used to update the E_x components directly above each $H_z(I+0.5,\ j+0.5,\ k+0.5)$, for any even integer I, where $0 \le I \le 2M$:

$$E_x^{n+1}(i+0.5,\ j,\ k+0.5) = E_x^n(i+0.5,\ j,\ k+0.5)$$

$$+\frac{\Delta t}{\varepsilon_0\ \Delta_{\text{r}}}\left[H_y^{n+0.5}(i+0.5,\ j,\ k)-H_y^{n+0.5}(i+0.5,\ j,\ k+1)\right]\quad(25)$$

$$+\frac{\Delta t}{\varepsilon_0\ \Delta_{\text{s-n}}}\left[\begin{array}{l} H_z^{n+0.5}(i+0.5,\ j+0.5,\ k+0.5)-\\ H_z^{n+0.5}(i+0.5,\ j-0.5,\ k+0.5)\end{array}\right]$$

The E_x field below each H_z is updated as follows:

$$E_x^{n+1}(i+0.5,\ j,\ k+0.5) = E_x^n(i+0.5,\ j,\ k+0.5)$$

$$+\frac{\Delta t}{\varepsilon_0\ \Delta_{\text{r}}}\left[H_y^{n+0.5}(i+0.5,\ j,\ k)-H_y^{n+0.5}(i+0.5,\ j,\ k+1)\right]\quad(26)$$

$$+\frac{\Delta t}{\varepsilon_0\ \Delta_{\text{s-n}}}\left[\begin{array}{l} H_z^{n+0.5}(i+0.5,\ j+0.5,\ k+0.5)-\\ H_z^{n+0.5}(i+0.5,\ j-0.5,\ k+0.5)\end{array}\right]$$

Each E_y field at the periphery of the cell can be updated as follows:

$$E_y^{n+1}(i,\ j+0.5,\ k+0.5) = E_y^n(i,\ j+0.5,\ k+0.5)$$

$$+\frac{\Delta t}{\varepsilon_0\,\Delta_{\mathrm{r}}}\left[H_x^{n+0.5}(i,\ j+0.5,\ k+1) - H_x^{n+0.5}(i,\ j+0.5,\ k)\right] \qquad (27)$$

$$+\frac{\Delta t}{\varepsilon_0\,\Delta_{\mathrm{w\text{-}e}}(j+0.5,\ k+0.5)}\left[\begin{array}{l} H_z^{n+0.5}(i-0.5,\ j+0.5,\ k+0.5)- \\ H_z^{n+0.5}(i+0.5,\ j+0.5,\ k+0.5) \end{array}\right]$$

West-East Grid Wrap-Around (Periodic Boundary Condition)

The grid wrap-around (periodic boundary condition) in the west-east direction completes the FDTD algorithm for the TE components. For each row j of grid column $i=0.5$, this is implemented by the following special time-stepping relation for H_z at the west boundary of the grid:

$$H_z^{n+1.5}(0.5,\ j+0.5,\ k+0.5) = H_z^{n+0.5}(0.5,\ j+0.5,\ k+0.5)$$

$$+\frac{\Delta t}{\mu_0\,S(j+0.5,\ k+0.5)}\left\{\begin{array}{l} E_x^n(0.5,\ j+1,\ k+0.5)\,\Delta_{\mathrm{w-e}}(j+1,\ k+0.5)- \\ E_x^n(0.5,\ j,\ k+0.5)\,\Delta_{\mathrm{w-e}}(j,\ k+0.5)+ \\ \left[\begin{array}{l} E_y^n(2M,\ j+0.5,\ k+0.5)- \\ E_y^n(1,\ j+0.5,\ k+0.5) \end{array}\right]\Delta_{\mathrm{s-n}} \end{array}\right\}$$

$$(28a)$$

Upon obtaining each such H_z value, the grid wrap-around is completed by implementing the following special relation for each row j of grid column $i=2M+0.5$ for H_z at the east boundary of the grid:

$$H_z^{n+1.5}(2M+0.5,\ j+0.5,\ k+0.5) = H_z^{n+1.5}(0.5,\ j+0.5,\ k+0.5) \qquad (28b)$$

3.3   Geodesic Grid-Cell Arrangement

This Section describes the FDTD algorithm used to model the global Earth-ionosphere waveguide using a "geodesic" lattice arrangement.   Geodesic grids have been employed since the 1960's for the study of geophysical phenomena [68]. Comprised entirely of hexagon cells except for a small, fixed number of pentagon cells, they are best described as resembling the surface of a soccer ball [69]. The geodesic FDTD model developed in this Section is generated in collaboration with climatologist R. Heikes and is analogous to the grids currently being used for climate modeling [70].

The geodesic FDTD model is superior to the latitude-longitude model of Section 3.2 in a number of respects [70]. First, the geodesic grid completely avoids grid-cell convergences at the North and South Poles. Therefore, it provides much more isotropic wave propagation and is simpler to construct. Second, the geodesic grid ports efficiently to a massively parallel supercomputer. Third, it permits an easier interchange of data with state-of-the-art Earth-simulation codes used by the geophysics community.

3.3.1   2-D Model

In preparation of a fully 3-D model, the complete spherical surface of the Earth is first mapped onto a geodesic grid for the 2-D TM case of Maxwell's equations [66, 70]. Fig. 9 illustrates a sample grid having a total of 642 planar cells, of which 630 are hexagons and 12 are pentagons [69]. For purposes of efficient mapping into the computer memory, this grid can be divided into five equal panels of size $im5 \times jm$ cells, where $im5 = 18$ and $jm = 10$. Fig. 10a shows the five grid panels of Fig. 9 after unwrapping and stretching them flat. The cells at the North and South

Poles can be arbitrarily connected to any of the five panels. The $(i = 1, j = jm)$, $(i = im5, j = jm)$, and $(i = im5, j = 1)$ cells are dead cells, and the remainder of the cells in the $i = 1$ and $i = im5$ rows and in the $j = 1$ and $j = jm$ columns of each of the five panels correspond to ghost cells (see Section 3.3.2). Fig. 10b illustrates how the five grid panels of Fig. 9 can be assigned logically Cartesian coordinates, and how all five panels can then be laid side-by-side to constitute an overall $(im = 90, jm = 10)$ logically Cartesian grid. This powerful interpretation of a spherical geodesic grid as a single logically Cartesian grid for purposes of efficient computer processing can be implemented for a variety of meshing densities over the sphere, as shown in Table 1 [71].

(a) (b)
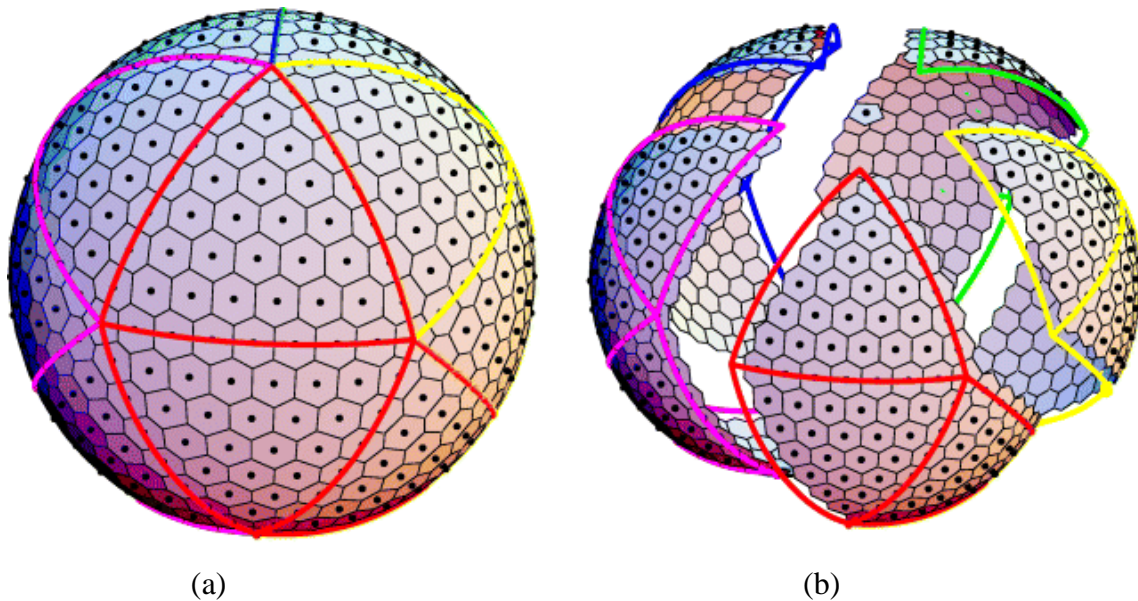
Figure 9 General layout of a 642-cell, two-dimensional geodesic grid covering the complete Earth-sphere. Each grid cell is planar. The grid is divided into five equal panels with $im5 = 18$ and $jm = 10$ (Figure courtesy of [69]).

(a)

(b)
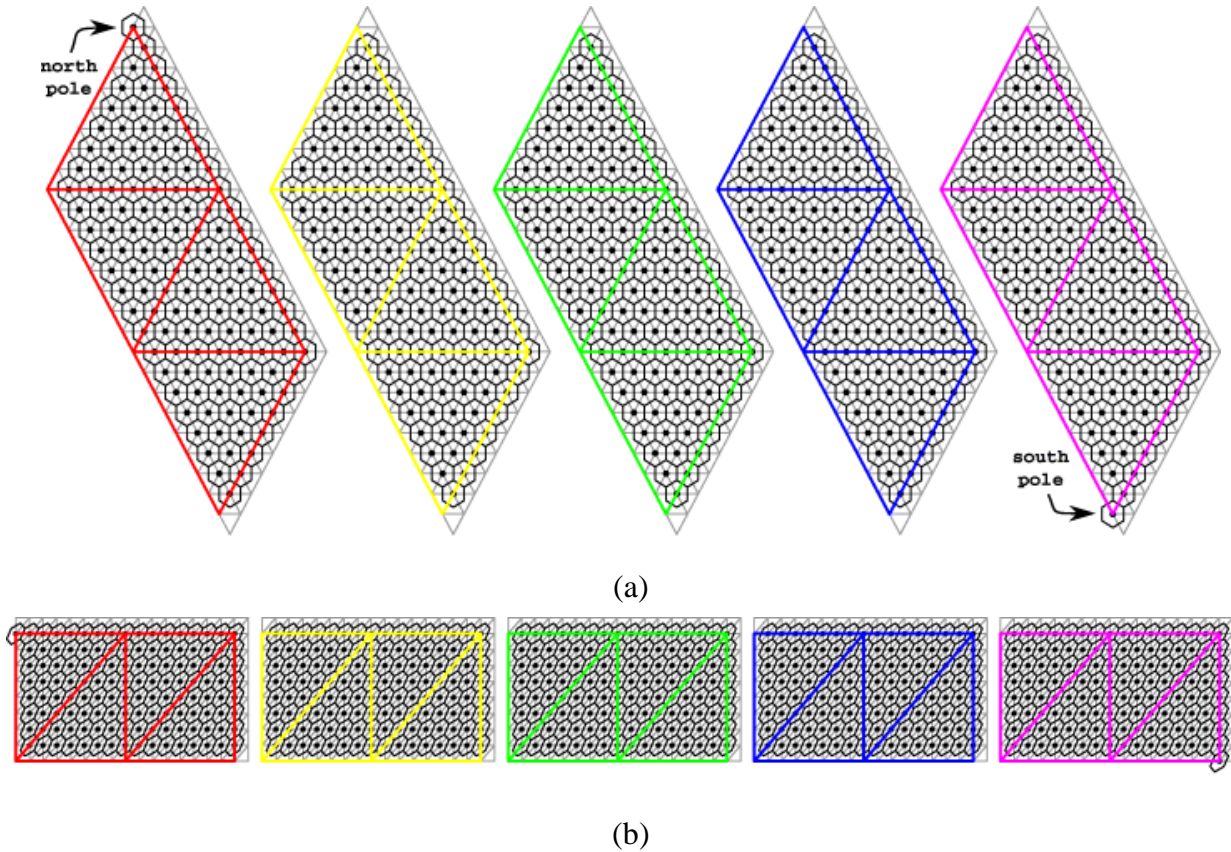
Figure 10 (a) The five ($im5 = 18$, $jm = 10$) grid panels of Fig. 9 after unwrapping and stretching them flat. The ($i = 1$, $j = jm$), ($i = im5$, $j = jm$), and ($i = im5$, $j = 1$) cells are dead cells, and the remainder of the cells in the $i = 1$ and $i = im5$ rows and in the $j = 1$ and $j = jm$ columns of each of the five panels correspond to ghost cells. Although shown as hexagons, the 12 pentagon cells are located at the North and South Poles, and at ($i = im5/2$, $j = jm - 1$) and ($i = im5 - 1$, $j = jm - 1$) on each of the five grid panels. (b) Illustration of how the cells in the five grid panels of Fig. 9 can be assigned logically Cartesian coordinates, and how all five panels can then be laid side-by-side to constitute an overall ($im = 90$, $jm = 10$) logically Cartesian grid (Figure courtesy of [69]).

Total Number of Cells	*im5*	*jm*	Distance between grid points (km)
10,242	66	34	250.1
40,962	130	66	125.1
163,842	258	130	62.55
655,362	514	258	31.27
2,621,442	1026	514	15.64
10,485,762	2050	1026	7.819

Table 1   The horizontal (*im5*) and vertical (*jm*) number of cells for the five panels at different resolutions along with the corresponding distances between adjacent grid points [71].

Regardless of the grid resolution, we note that all but 12 of the cells for the TM case are planar hexagons. Although shown as hexagons in Fig. 10, these 12 pentagon cells are located at the North and South Poles, and at $(i = im5/2, j = jm - 1)$ and $(i = im5 - 1, j = jm - 1)$ on each of the five grid panels. Each of the hexagonal cells has E and H components distributed as shown in Fig. 11a. Fig. 11b then illustrates how the E and H components are distributed about each of the 12 planar pentagons.

Reference [72] describes in detail an optimization procedure for selecting the areas and locations of the hexagonal and pentagonal grid cells on the sphere to insure numerical consistency and to maximize the order of accuracy in the context of the Laplace operator. We have found that this optimization procedure also maximizes the observed accuracy of wave propagation about the sphere as governed by the 2-D TM Maxwell's equations [70].

⊙ $E_r(i, j+1, k)$

area $S(i, j, k)$

$H_3(i, j+1, k)$

⊙
$E_r(i-1, j, k)$

$\Delta_{i, j+1, k}(3)$

⊙
$E_r(i+1, j+1, k)$

$H_1(i, j, k)$

$H_2(i+1, j+1, k)$

$\Delta_{i, j, k}(1)$

$\Delta_{i+1, j+1, k}(2)$

⊙
$E_r(i, j, k)$

$\Delta_{i+1, j, k}(1)$

$H_2(i, j, k)$

$\Delta_{i, j, k}(2)$

$H_1(i+1, j, k)$

$\Delta_{i, j, k}(3)$

⊙
$E_r(i-1, j-1, k)$

$H_3(i, j, k)$

⊙
$E_r(i+1, j, k)$

⊙ $E_r(i, j-1, k)$
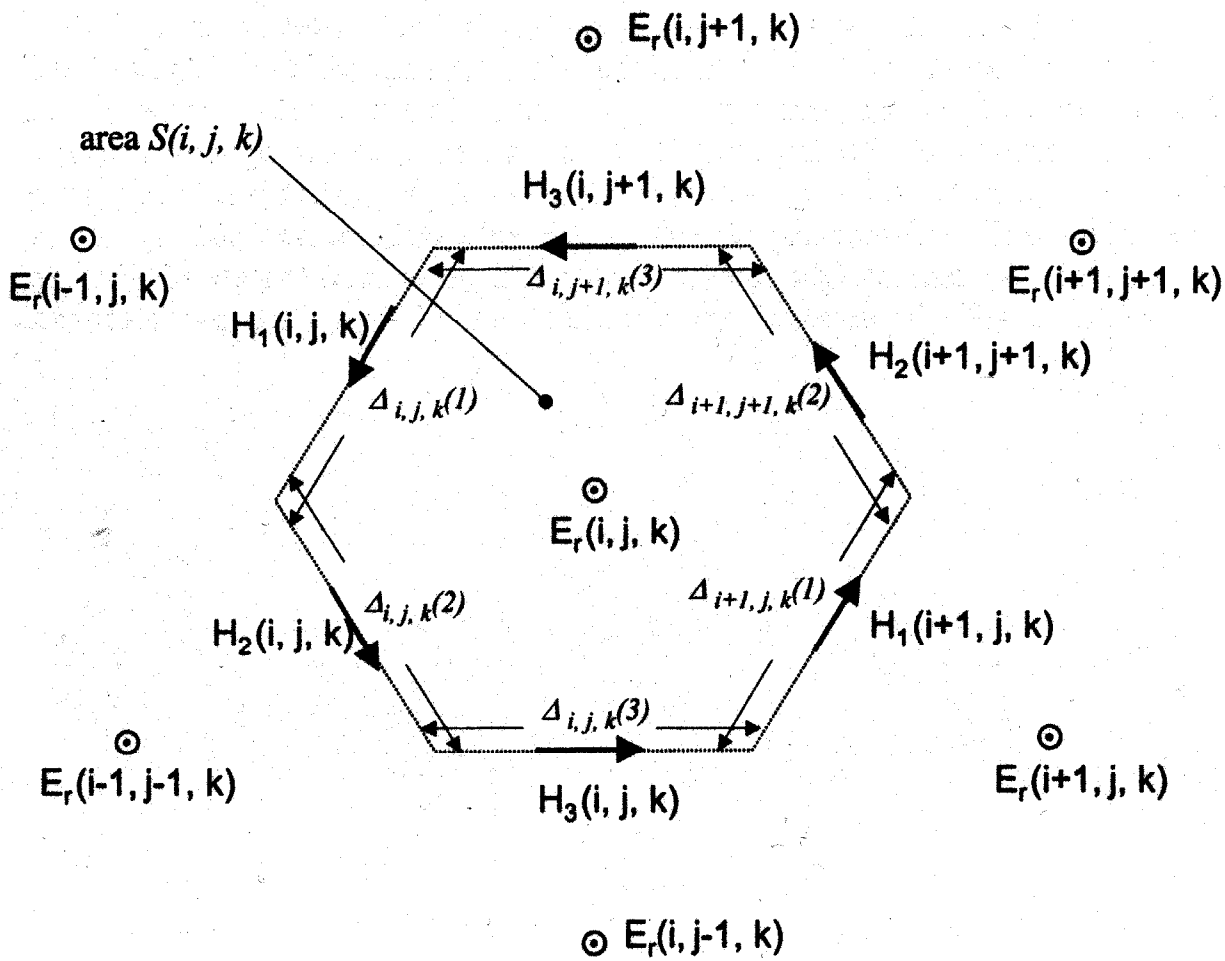
(a)
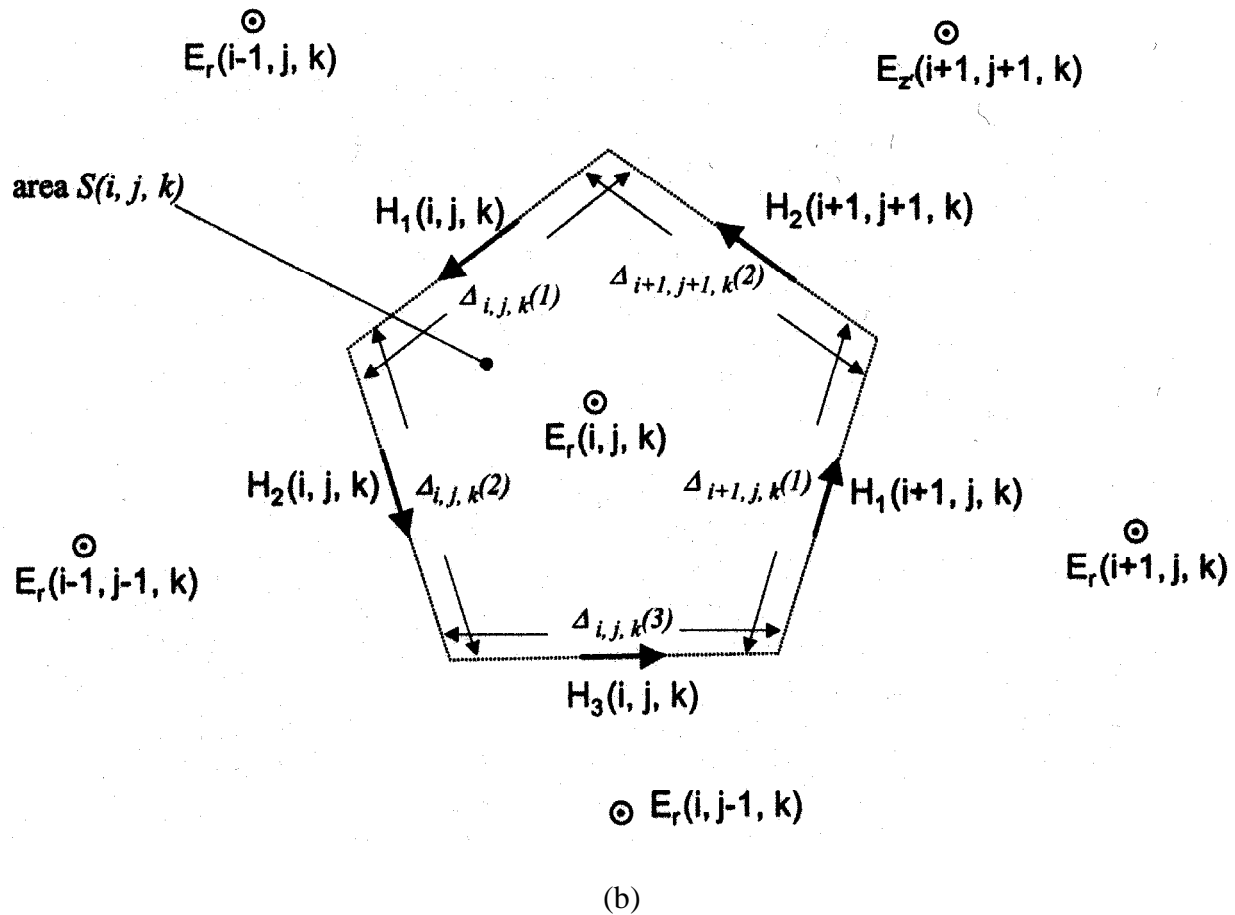
Figure 11 Details of the grid-cell geometry for the TM$_r$ case: (a) hexagon cell; (b) pentagon cell.

The complete FDTD algorithm for the 2-D geodesic spherical Earth grid is presented in [70]. Because this algorithm is incorporated into the fully 3-D formulation presented in the following Section, only the 2-D modeling results will be presented here.

First, the accuracy of the 2-D FDTD numerical model is tested using an impulsive circular cylindrical wave. The idea here is to track an impulsive circular cylindrical wave in time and space as it propagates radially outward from a filamentary current source, travels completely around the Earth-sphere model, and then propagates radially inward to the antipode. Results are shown for a lossless geodesic FDTD grid with 40,962 cells ($im5 = 130$ and $jm = 66$) spanning the Earth-sphere, with the time step $\Delta t = 25$ μs. For this simulation, implemented in Fortran 90 on a Dell 530 workstation running Linux, the required computer memory is 3.3 MB and the running time 2.5 minutes for a single wave circumnavigation of the Earth-sphere. In comparison, a comparably resolved latitude-longitude FDTD grid of the type introduced in Section 3.2.1 would require 2.4 MB and 34 minutes running time on the same computer. Thus, the geodesic FDTD grid executes about 14-times faster while requiring only about 1.4-times more data storage in two dimensions.

Fig. 12 is a snapshot visualization of the electric field calculated using the new geodesic FDTD grid model projected onto the surface of the Earth-sphere as the radiated wave converges to the antipode. Superimposed on this visualization is: (1) a sample computed contour of equal-amplitude electric field; and (2) a circle centered at the antipode that is drawn to have a radius matching as well as possible that of the equal-amplitude electric field contour. Fig. 12 shows that there is negligible deviation of the computed equal-amplitude electric field contour from the circle. This means that the impulsive numerical wave has propagated from its source point almost completely to the antipode in an azimuthally isotropic manner despite passing through

regions of hexagonal and pentagonal grid cells of varying areas. By way of comparison, using this same test, the azimuthal isotropy of wave propagation within the latitude-longitude FDTD grid introduced in Section 3.2.1 is poorer by approximately one order-of-magnitude for grids of comparable spatial resolution.
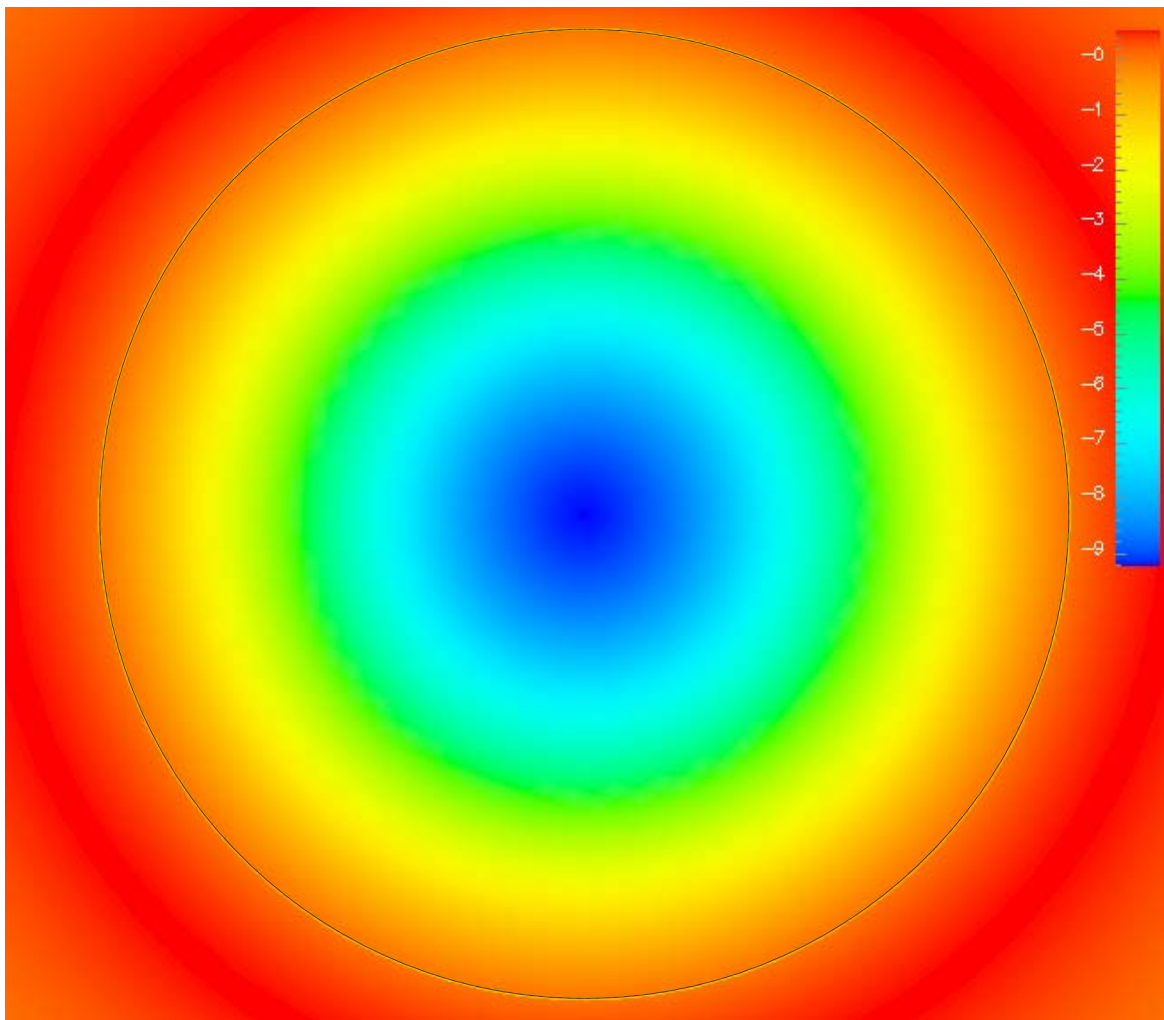
Figure 12 Visualization of the electric field projected onto the surface of the Earth-sphere as the radiated wave converges to the antipode. Note that the white contour of calculated equal-amplitude electric field coincides almost exactly with a black dotted circle centered on the antipode.

Fig. 13 graphs the calculated time-waveform of the electric field at the antipode for the first two circumnavigations of the Earth-sphere. This figure shows the 180° phase reversals of the electric-field at the antipode first calculated by Wait [4]. Further, this figure shows a 0.134-second circumnavigation period, corresponding to a 7.46-Hz fundamental resonance of the lossless 2-D Earth model. This is virtually the same as that obtained previously by a comparably resolved latitude-longitude FDTD grid of Section 3.2.1.
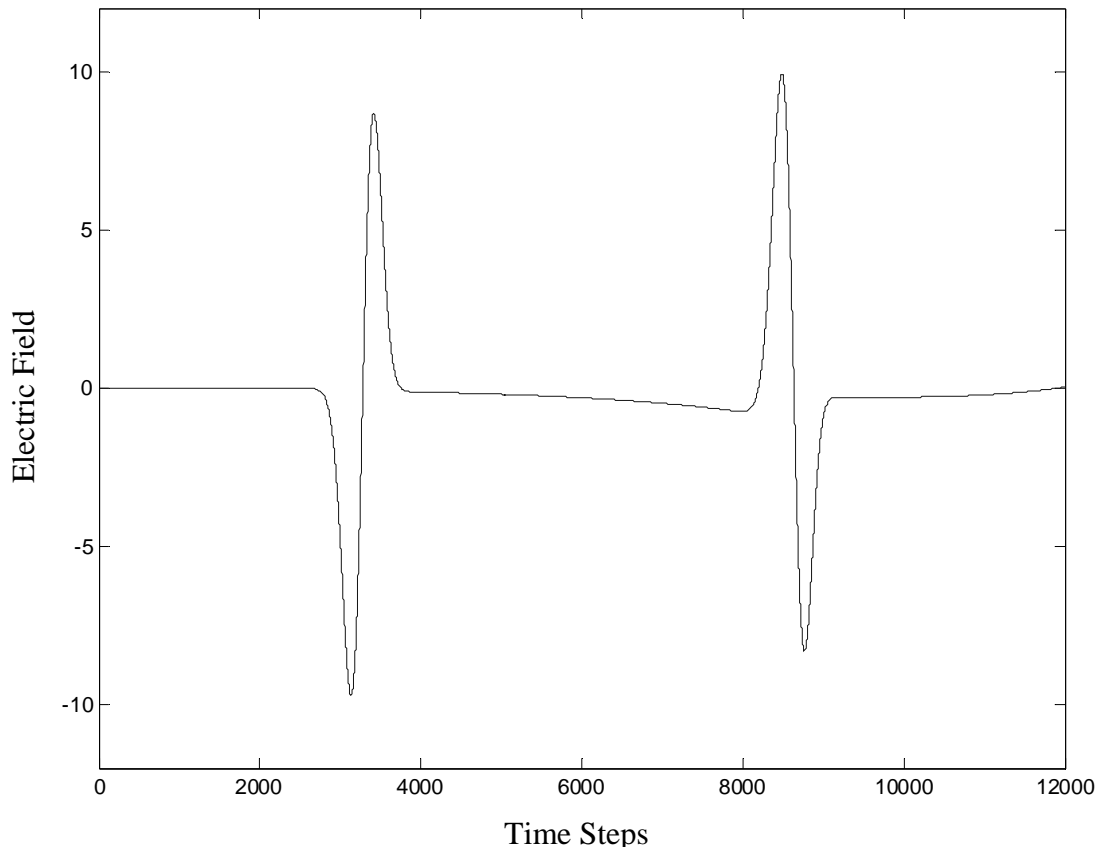
Figure 13 Calculated time-waveform of the electric field at the antipode for the first two circumnavigations of the Earth-sphere.

3.3.2 3-D Model

The 2-D work of Section 3.3.1 is expanded here to create a fully 3-D FDTD model of the entire Earth-ionosphere cavity extending between ±100 km of sea level [73]. This new 3-D space lattice has a nominal resolution of about 63 x 63 x 5 km, however it is constructed to permit variable cell size in the radial (vertical) direction. There are 163,842 total cells at each of the 40 radial coordinates (see Table 1), yielding a total of over 6.5 million cells for the entire 3-D grid. Only a single-processor laboratory computer with 2 GB memory is needed to process the model.
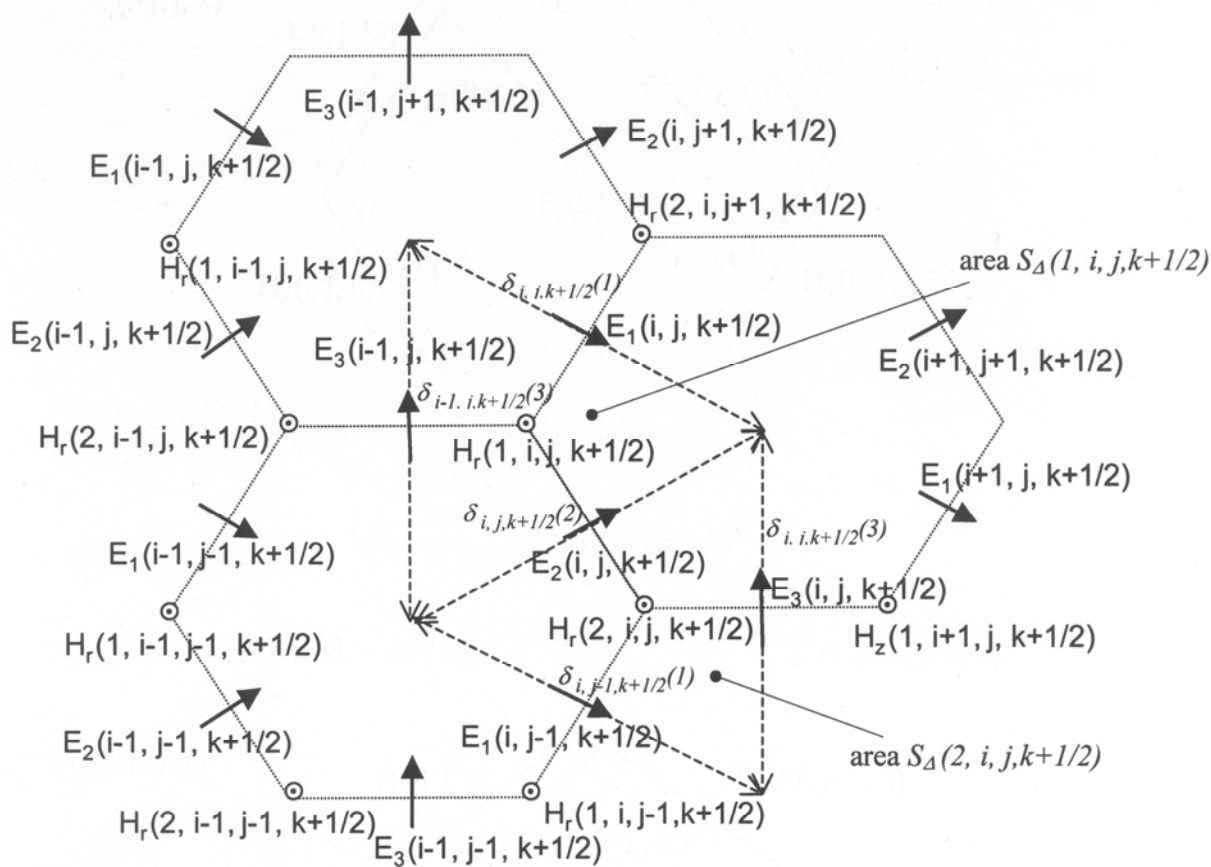
Figure 14 Details of the TE$_r$ triangular grid cell geometry centered one-half cell above the vertices of the TM$_r$ hexagon/pentagon cells of Fig. 11.

As for the 3-D latitude-longitude model, the complete 3-D geodesic model is comprised of alternating planes of TM and TE field components in the radial direction. Each TM plane is of the type discussed in Section 3.3.1 and shown in Fig. 9. That is, the TM planes are comprised of hexagonal and pentagonal cells (Figs. 11a and 11b). Similarly, each TE plane at a constant radial coordinate is comprised of triangular cells centered above and below the vertices of each hexagonal and pentagonal cell of the TM plane as shown in Fig. 14. Adjacent TE and TM planes are then coupled together via regular Yee-type updates. Below, the FDTD algorithm is provided for each of the eight field components of the 3-D geodesic FDTD grid.

Basic Algorithm, TM_r Components

Ampere's Law in integral form [14] can be applied to develop an FDTD time-stepping relation for the electric field E_r at the center of the $(i,\,j,\,k)$'th hexagonal grid cell. For example, referring to Fig. 11a, for a hexagonal cell we have

$$E_r^{n+1}(i,\,j,k) = E_r^n(i,\,j,k) + \frac{\Delta t}{\varepsilon_0\,S(i,j,k)}\left\{\begin{array}{l} H_1^{n+0.5}(i,\,j,\,k)\,\Delta_{i,j,k}(1)\ + \\[4pt] H_2^{n+0.5}(i,\,j,\,k)\,\Delta_{i,j,k}(2)\ + \\[4pt] H_3^{n+0.5}(i,\,j,\,k)\,\Delta_{i,j,k}(3)\ - \\[4pt] H_1^{n+0.5}(i+1,\,j,\,k)\,\Delta_{i+1,j,k}(1)\ - \\[4pt] H_2^{n+0.5}(i+1,\,j+1,\,k)\,\Delta_{i+1,j+1,k}(2)\ - \\[4pt] H_3^{n+0.5}(i,\,j+1,\,k)\,\Delta_{i,j+1,k}(3) \end{array}\right\} \tag{29}$$

where Δt is the time-step, $\Delta_{i,j,k}(n)$ is the nth wall length of the cell centered around $E_r\,(i,\,j,\,k)$ (where n is equal to one, two, or three), and $S(i,\,j,\,k)$ is the area of the cell centered around $E_r\,(i,\,j,\,k)$.

Similarly, referring to Fig. 11b, the update for E_r at the center of a pentagonal cell at mid-latitude is given by

$$E_r^{n+1}(i,\ j,\ k) = E_r^n(i,\ j,\ k) + \frac{\Delta t}{\varepsilon_0\ S(i,\ j,\ k)} \left\{ \begin{array}{l} H_1^{n+0.5}(i,\ j,\ k)\ \Delta_{i,j,k}(1)\ + \\ H_2^{n+0.5}(i,\ j,\ k)\ \Delta_{i,j,k}(2)\ + \\ H_3^{n+0.5}(i,\ j,\ k)\ \Delta_{i,j,k}(3)\ - \\ H_1^{n+0.5}(i+1,\ j,\ k)\ \Delta_{i+1,j,k}(1)\ - \\ H_2^{n+0.5}(i+1,\ j+1,\ k)\ \Delta_{i+1,j+1,k}(2) \end{array} \right\} \tag{30}$$

In the same manner, the updates for E_r at the center of a pentagonal cell at the North and South Poles are given respectively by

$$E_r^{n+1}(1,\ jm-1,\ k) = E_r^n(1,\ jm-1,\ k) +$$

$$\frac{\Delta t}{\varepsilon_0\ S(1,\ jm-1,\ k)} \left\{ \begin{array}{l} -H_1^{n+0.5}(2,\ jm-1,\ k)\ \Delta_{2,\,jm\text{-}1,\,k}(1)\ - \\ H_1^{n+0.5}(im5+2,\ jm-1,\ k)\ \Delta_{im5+2,\,jm\text{-}1,\,k}(1)\ - \\ H_1^{n+0.5}(im5*2+2,\ jm-1,\ k)\ \Delta_{im5*2+2,\,jm\text{-}1,\,k}(1)\ - \\ H_1^{n+0.5}(im5*3+2,\ jm-1,\ k)\ \Delta_{im5*3+2,\,jm\text{-}1,\,k}(1)\ - \\ H_1^{n+0.5}(im5*4+2,\ jm-1,\ k)\ \Delta_{im5*4+2,\,jm\text{-}1,\,k}(1) \end{array} \right\} \tag{31}$$

$$E_r^{n+1}(im-1,1,\ k) = E_r^n(im-1,\ 1,\ k) +$$

$$\frac{\Delta t}{\varepsilon_0\ S(im-1,1,\ k)} \left\{ \begin{array}{l} -H_3^{n+0.5}(im5-1,\ 2,\ k)\ \Delta_{im5\text{-}1,\,2,\,k}(3)\ - \\ H_3^{n+0.5}(im5*2-1,\ 2,\ k)\ \Delta_{im5*2\text{-}1,\,2,\,k}(3)\ - \\ H_3^{n+0.5}(im5*3-1,\ 2,\ k)\ \Delta_{im5*3\text{-}1,\,2,\,k}(3)\ - \\ H_3^{n+0.5}(im5*4-1,\ 2,\ k)\ \Delta_{im5*4\text{-}1,\,2,\,k}(3)\ - \\ H_3^{n+0.5}(im5*5-1,\ 2,\ k)\ \Delta_{im5*5\text{-}1,\,2,\,k}(3) \end{array} \right\} \tag{32}$$

where the $\Delta_{i,j,k}(n)$ and the H_1 or H_3 component having the indicated coordinates from each of the five panels are used.

The basic FDTD time-stepping algorithm for the TM$_r$ components is completed by specifying the updates for the H_1, H_2, and H_3 fields using Faraday's Law in integral form [14]. For example, referring to the grid cells shown in Figs. 11 and 14, we have

$$H_1^{n+1.5}(i,\,j,\,k) = H_1^{n+0.5}(i,\,j,\,k) + \frac{\Delta t}{\mu_0\,\delta_{i,j,k}(1)}\left[E_r^{n+1}(i-1,\,j,\,k) - E_r^{n+1}(i,\,j,\,k)\right]$$
$$+ \frac{\Delta t}{\mu_0\,\Delta r}\left[E_1^{n+1}(i,\,j,\,k+\frac{1}{2}) - E_1^{n+1}(i,\,j,\,k-\frac{1}{2})\right]$$

(33)

$$H_2^{n+1.5}(i,\,j,\,k) = H_2^{n+0.5}(i,\,j,\,k) + \frac{\Delta t}{\mu_0\,\delta_{i,j,k}(2)}\left[E_r^{n+1}(i-1,\,j-1,\,k) - E_r^{n+1}(i,\,j,\,k)\right]$$
$$+ \frac{\Delta t}{\mu_0\,\Delta r}\left[E_2^{n+1}(i,\,j,\,k+\frac{1}{2}) - E_2^{n+1}(i,\,j,\,k-\frac{1}{2})\right]$$

(34)

$$H_3^{n+1.5}(i,\,j,\,k) = H_3^{n+0.5}(i,\,j,\,k) + \frac{\Delta t}{\mu_0\,\delta_{i,j,k}(3)}\left[E_r^{n+1}(i,\,j-1,\,k) - E_r^{n+1}(i,\,j,\,k)\right]$$
$$+ \frac{\Delta t}{\mu_0\,\Delta r}\left[E_3^{n+1}(i,\,j,\,k+\frac{1}{2}) - E_3^{n+1}(i,\,j,\,k-\frac{1}{2})\right]$$

(35)

where Δr is the lattice space cell increment in the radial direction and $\delta_{i,j,k}(n)$ is the nth distance between adjacent E_r components as shown for one-half cell above the TM$_r$ plane in Fig. 14.

Basic Algorithm, TE$_r$ Components

Faraday's Law in integral form [14] can be applied to develop an FDTD time-stepping relation for the H_r field at the center of the $(i,\,j,\,k+\frac{1}{2})$'th triangular grid cell, one-half cell directly above the vertex v of the $(i,\,j,\,k)$'th hexagonal/pentagonal grid cell (where v is equal to one or two). For example, referring to Fig. 14, we have

$$H_r^{n+1.5}(1,i,j,k+\frac{1}{2}) = H_r^{n+0.5}(1,i,j,k+\frac{1}{2}) +$$

$$\frac{\Delta t}{\mu_0 S_\Delta(1,i,j,k+\frac{1}{2})} \left\{ \begin{array}{l} E_1^{n+1}(i,j,k+\frac{1}{2})\, \delta_{i,j,k+\frac{1}{2}}(1) \\[2ex] -E_2^{n+1}(i,j,k+\frac{1}{2})\, \delta_{i,j,k+\frac{1}{2}}(2) \\[2ex] +E_3^{n+1}(i-1,j,k+\frac{1}{2})\, \delta_{i-1,j,k+\frac{1}{2}}(3) \end{array} \right\} \qquad (36)$$

$$H_r^{n+1.5}(2,i,j,k+\frac{1}{2}) = H_r^{n+0.5}(2,i,j,k+\frac{1}{2}) +$$

$$\frac{\Delta t}{\mu_0 S_\Delta(2,i,j,k+\frac{1}{2})} \left\{ \begin{array}{l} E_2^{n+1}(i,j,k+\frac{1}{2})\, \delta_{i,j,k+\frac{1}{2}}(2) \\[2ex] -E_3^{n+1}(i,j,k+\frac{1}{2})\, \delta_{i,j,k+\frac{1}{2}}(3) \\[2ex] -E_1^{n+1}(i,j-1,k+\frac{1}{2})\, \delta_{i,j-1,k+\frac{1}{2}}(1) \end{array} \right\} \qquad (37)$$

where $\delta_{i,j,k+\frac{1}{2}}(n)$ is the nth wall length of the triangular cell centered around $H_z(v,i,j,k+1/2)$ and $S_\Delta(v,i,j,k+1/2)$ is the area of the triangular cell centered around $H_z(v,i,j,k+1/2)$.

The basic FDTD time-stepping algorithm for the TE_r components is completed by specifying the electric field updates using Ampere's Law in integral form [14]. For example, referring to Fig. 14, we have

$$E_1^{n+1}(i,j,k+\frac{1}{2}) = E_1^n(i,j,k+\frac{1}{2}) + \frac{\Delta t}{\varepsilon_0 \Delta_{i,j,k+\frac{1}{2}}(1)} \left[\begin{array}{l} H_r^{n+0.5}(2,i,j+1,k+\frac{1}{2}) \\[2ex] -H_r^{n+0.5}(1,i,j,k+\frac{1}{2}) \end{array} \right]$$

$$+ \frac{\Delta t}{\varepsilon_0 \Delta r} \left[\begin{array}{l} H_1^{n+0.5}(i,j,k+1) \\[2ex] -H_1^{n+0.5}(i,j,k) \end{array} \right] \qquad (38)$$

$$E_2^{n+1}(i,\,j,\,k+\frac{1}{2}) = E_2^n(i,\,j,\,k+\frac{1}{2}) + \frac{\Delta t}{\varepsilon_0 \Delta_{i,j,k+\frac{1}{2}}(2)} \left[\begin{array}{l} H_r^{n+0.5}(1,i,\,j,\,k+\frac{1}{2}) \\[2mm] -H_r^{n+0.5}(2,i,\,j,\,k+\frac{1}{2}) \end{array} \right]$$
$$+ \frac{\Delta t}{\varepsilon_0 \Delta r}\left[\begin{array}{l} H_2^{n+0.5}(i,\,j,\,k+1) \\[2mm] -H_2^{n+0.5}(i,\,j,\,k) \end{array} \right] \tag{39}$$

$$E_3^{n+1}(i,\,j,\,k+\frac{1}{2}) = E_3^n(i,\,j,\,k+\frac{1}{2}) + \frac{\Delta t}{\varepsilon_0 \Delta_{i,j,k+\frac{1}{2}}(3)} \left[\begin{array}{l} H_r^{n+0.5}(2,i,\,j,\,k+\frac{1}{2}) \\[2mm] -H_r^{n+0.5}(1,i+1,\,j,\,k+\frac{1}{2}) \end{array} \right]$$
$$+ \frac{\Delta t}{\varepsilon_0 \Delta r}\left[\begin{array}{l} H_3^{n+0.5}(i,\,j,\,k+1) \\[2mm] -H_3^{n+0.5}(i,\,j,\,k) \end{array} \right] \tag{40}$$

where $\Delta_{i,j,k+\frac{1}{2}}(n)$ is the nth distance between adjacent H_r components as shown for ½ cell below the TE_r plane in Fig 11.

Grid Wrap-Around (Periodic Boundary Condition)

All field components on each of the five panels for which $2 < i < (im5-1)$ and $2 < j < (jm-1)$, along with the components at the centers of the pentagons at the North and South Poles are updated according to the algorithm presented in above. The ghost E and H field components, i.e. for $(i=1,\ 1<j<jm-2)$, $(1<i<im5-2, j=1)$, $(i=im5, 2<j<jm-1)$, and $(2<i<im5-1,\ j=jm)$ on all five panels, as well as for $(i=1,\ j=jm-1)$ and $(i=im5-1,\ j=1)$ on the four panels not updating the North and South Poles, are filled after each time step by setting them equal to the corresponding component of the neighboring panel.

4　　FDTD Modeling of the Earth-Ionosphere Waveguide

4.1　　Model Parameters and Inputs

For both the 3-D latitude-longitude model of Section 3.2.2 and the 3-D geodesic model of Section 3.3.2, topographic and bathymetric data from the NOAA-NGDC "Global Relief CD-ROM" [74] are utilized. Lithosphere conductivity is then assigned according to Fig. 15 (courtesy of [75]), depending upon whether the space lattice point is located directly below an ocean or within a continent. Isotropic ionospheric conductivity is assigned according to the exponential profile used in [76], which permits the most straightforward comparison of the present FDTD modeling results with the data reported in [77] since propagation below 1 kHz is crucially affected by the ionosphere characteristics. Note that, however, the present model is capable of significantly greater ionospheric detail (i.e. day-to-night transitions, anisotropy, etc.) than that possible using the analysis of [77].

4.2　　Propagation Attenuation Validation Study

The 3-D latitude-longitude and geodesic Earth-ionosphere models are first validated by comparing their predicted EM propagation behavior with the data reported in [77], which were shown previously to have excellent agreement with experimentally determined values of daytime attenuation rates. For this study, both FDTD models are excited at the Equator at 47° W (off the coast of South America) with a vertical, 5-km-long current pulse having a Gaussian time-waveform having a 1/e full-width of $480\Delta t$, where $\Delta t = 3.0 \ \mu s$. To ensure a smooth onset of the excitation, the temporal center of this pulse is at $960\Delta t$. Propagation attenuation modeling results are obtained over the range of 50–500 Hz.
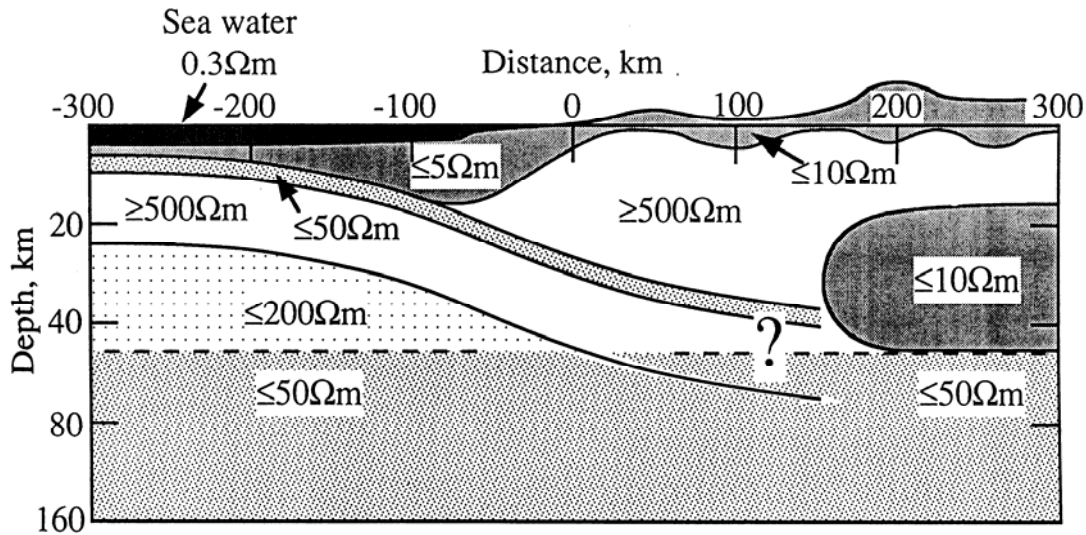
Figure 15 Conductivity values used for the lithosphere according to whether the space lattice point is located directly below an ocean or within a continent (courtesy of [75]).

Latitude-Longitude Model Validation Study

Fig. 16 presents snapshot visualizations of the FDTD-calculated global response as an EM wave propagates radially outwards from the Gaussian current source off the coast of South America, completely around the Earth, and then radially inwards towards the antipode. Fig. 17(a) graphs time-waveforms of the FDTD-calculated radial E-field at two observation points *A* and *A'* on the Earth's surface at the equator directly east and west of the source at ¼ of the distance to the antipode. Fig. 17(b) graphs the FDTD-calculated time-waveforms at points *B* and *B'* at the equator directly east and west of the source at ½ of the distance to the antipode. Note that waveform pair *A*, *A'* is not identical; similarly, waveform pair *B*, *B'* is not identical. The observed lack of symmetry is caused by a corresponding lack of symmetry of the lithosphere geometry in this region. Further, note the evolution of a "slow-tail" response similar to that predicted in [78].
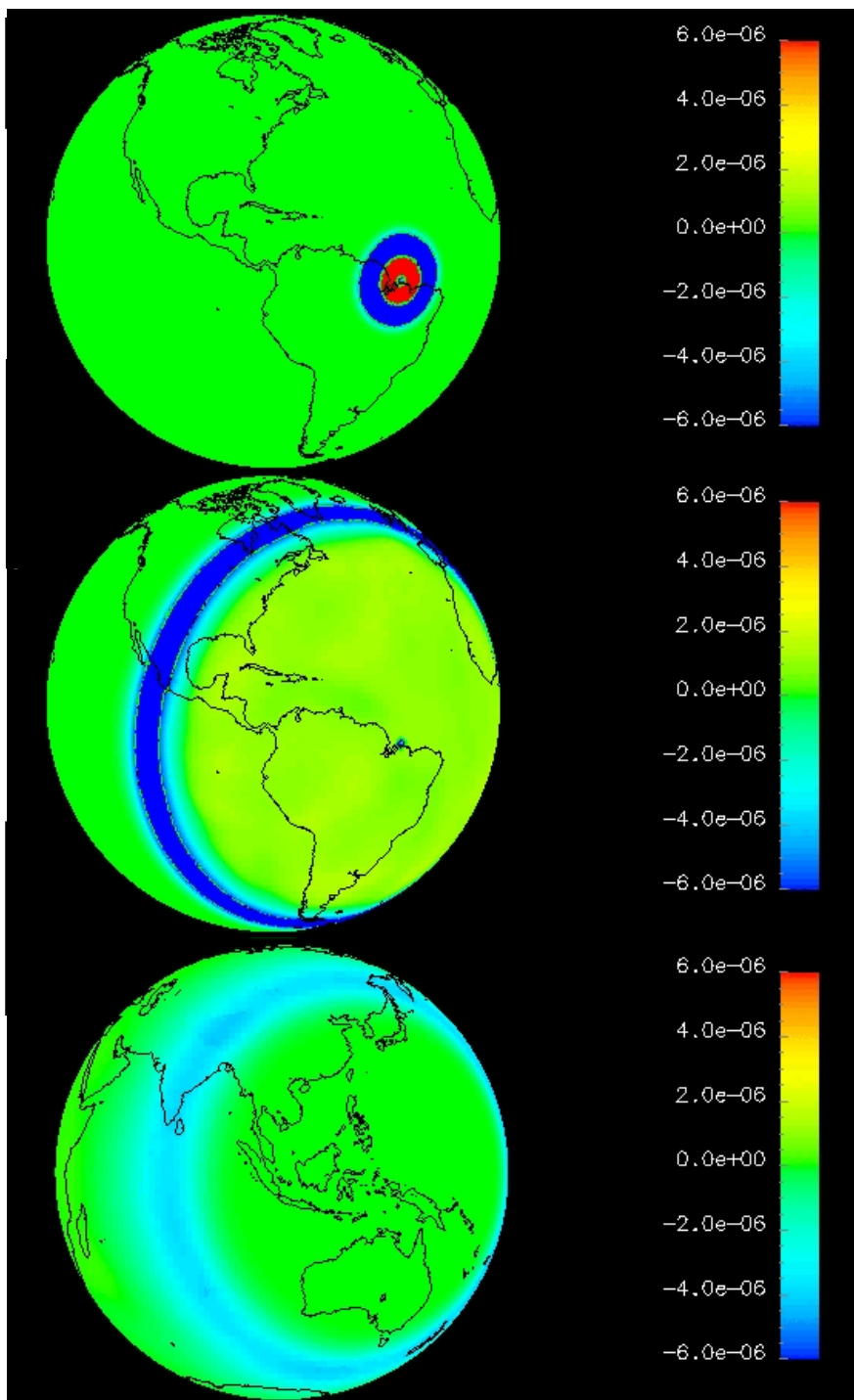
Figure 16 Snapshot visualizations of the FDTD-computed global propagation of an ELF

EM pulse generated by a 5-km-long Gaussian current pulse at the Equator off

the coast of South America.
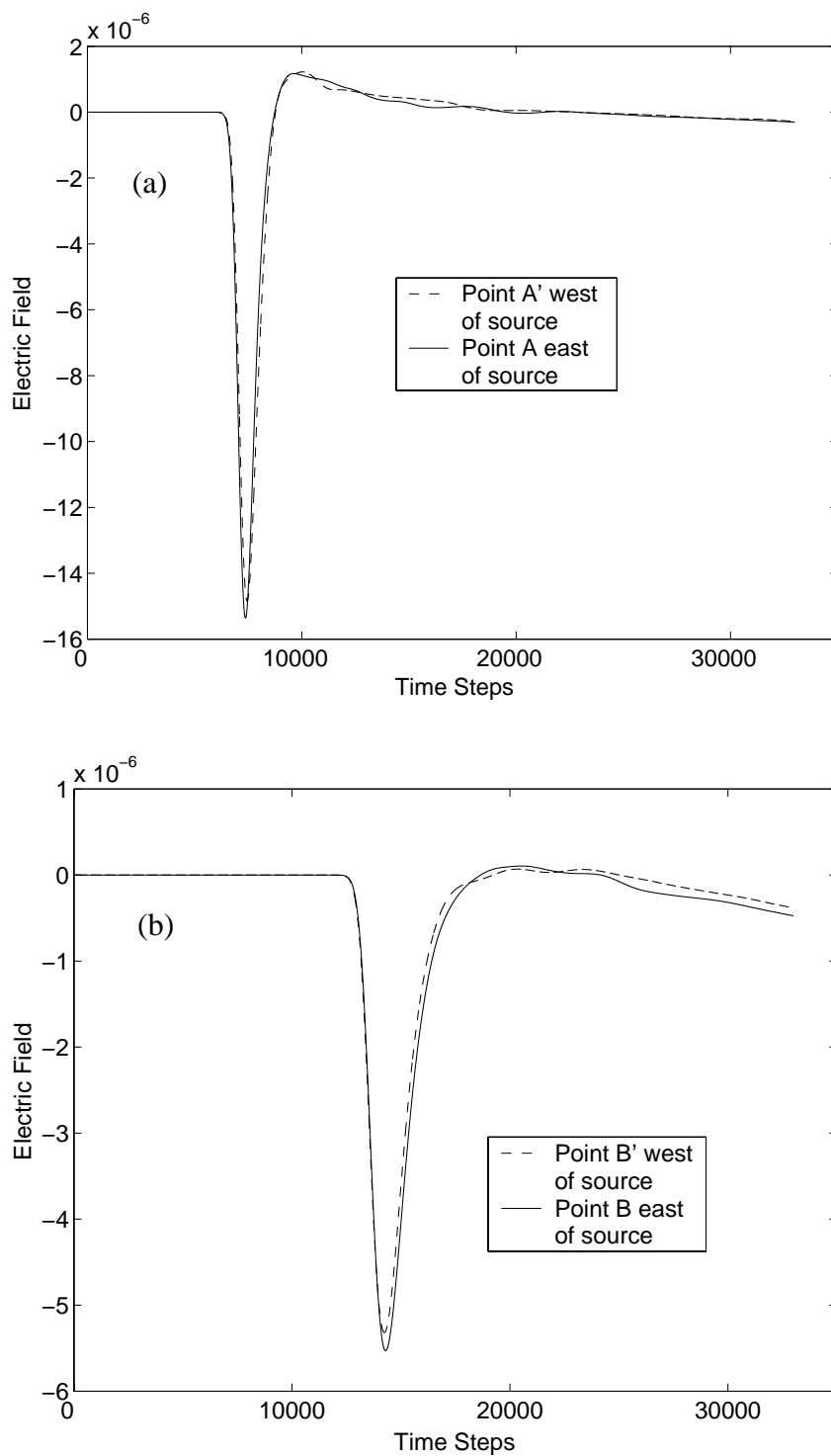
Figure 17 FDTD-calculated temporal response observed at the equator directly east and

west of the source: (a) at Points *A* and *A'* located ¼ of the distance to the

antipode; (b) at Points *B* and *B'* located at ½ of the distance to the antipode.

Fig. 18 compares the FDTD-calculated ELF propagation attenuation versus frequency over paths $A\,B$ and $A'\,B'$ with the results reported in [77]. The FDTD data are obtained by forming the ratio of the discrete Fourier transforms (DFTs) of the time-waveforms shown in Figs. 17(a) and 17(b). The time-waveforms at points A and B are truncated at 22,849 and 24,165 time steps, respectively; and the time-waveforms at points A' and B' are truncated at 22,737 and 25,023 time steps, respectively (i.e., at each zero-crossing preceding the slow-tail response).[1] Over the frequency range 50 – 500 Hz, the FDTD-computed propagation attenuation values agree with the results of [77] to within about ±0.5 dB/Mm over path $A\,B$ and within about ±1.0 dB/Mm over path $A'\,B'$.

Geodesic Model Validation Study

Fig. 19 graphs time-waveforms of the FDTD-calculated radial E-field at four observation points: A and A' on the Earth's surface directly east and west of the source at ¼ of the distance to the antipode along the equator, respectively; and points B and B' directly east and west of the source at ½ of the distance to the antipode along the equator, respectively. Although the east and west waveforms are similar in appearance for both cases (A and A'; B and B'), they are not identical because of the lack of symmetry of the lithosphere geometry. Note that the differences between the four waveforms here in Fig. 19 and those shown in Fig. 17 for the latitude-longitude grid are due to the lower resolution of the geodesic grid (65 km versus 40 km between adjacent grid points in the east-west direction) and therefore uses different topographical data values. Further, a higher-degree of isotropic wave propagation is achievable with the geodesic grid [70, 73], and the waveforms of Fig. 19 are normalized.

---

[1] The FDTD-calculated time-waveforms are windowed in this manner because the slow-tail response persists after the appearance of the signal arriving over the equatorial long path. Therefore, the slow-tail response cannot be time-stepped to its conclusion in isolation. The required windowing process in time results in a frequency window of approximately 50 - 500 Hz within which our FDTD results can be validly compared with the benchmark data of [77]. This is because errors in the DFTs occur below about 50 Hz due to the absence of the slow-tail response, while errors occur above about 500 Hz due to the truncation of the data records.

Fig. 20 compares the daytime FDTD-calculated ELF propagation attenuation versus frequency over paths $A\,B$ and $A'\,B'$ with the theoretical results reported in [77]. The FDTD data are obtained by forming the ratio of the discrete Fourier transforms (DFTs) of the time-waveforms shown in Fig. 19, with each of the waveforms truncated near 0.08 seconds (i.e., at each waveform's zero-crossing).[1] Over the frequency range 50 – 500 Hz, the FDTD-computed propagation attenuation values agree with the results of [77] to within about ±0.5 dB/Mm over both paths $A\,B$ and $A'\,B'$.
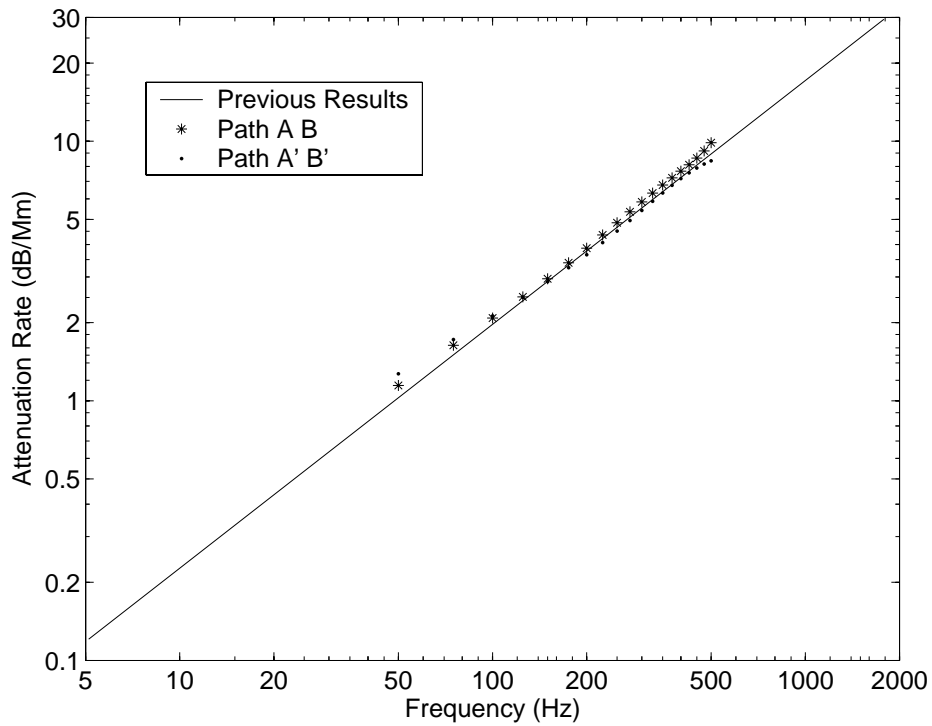
Figure 18 Comparison between the FDTD-calculated ELF propagation attenuation versus frequency over paths $A\,B$ and $A'\,B'$ with the results reported in [77].
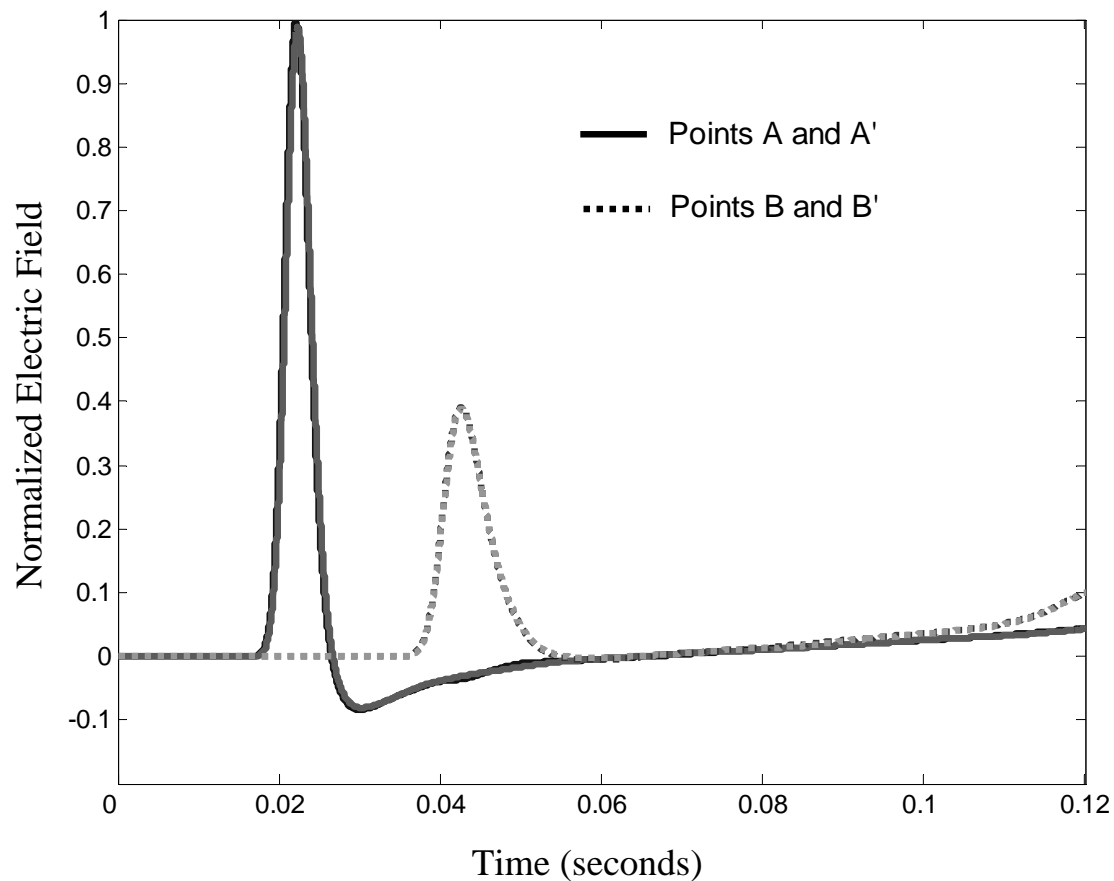
Figure 19 FDTD-calculated temporal response observed at the equator directly east and

west of the source for daytime ionosphere conductivity: (a) at points *A* and

A' located ¼ of the distance to the antipode; (b) at points *B* and *B'* located

at ½ of the distance to the antipode.
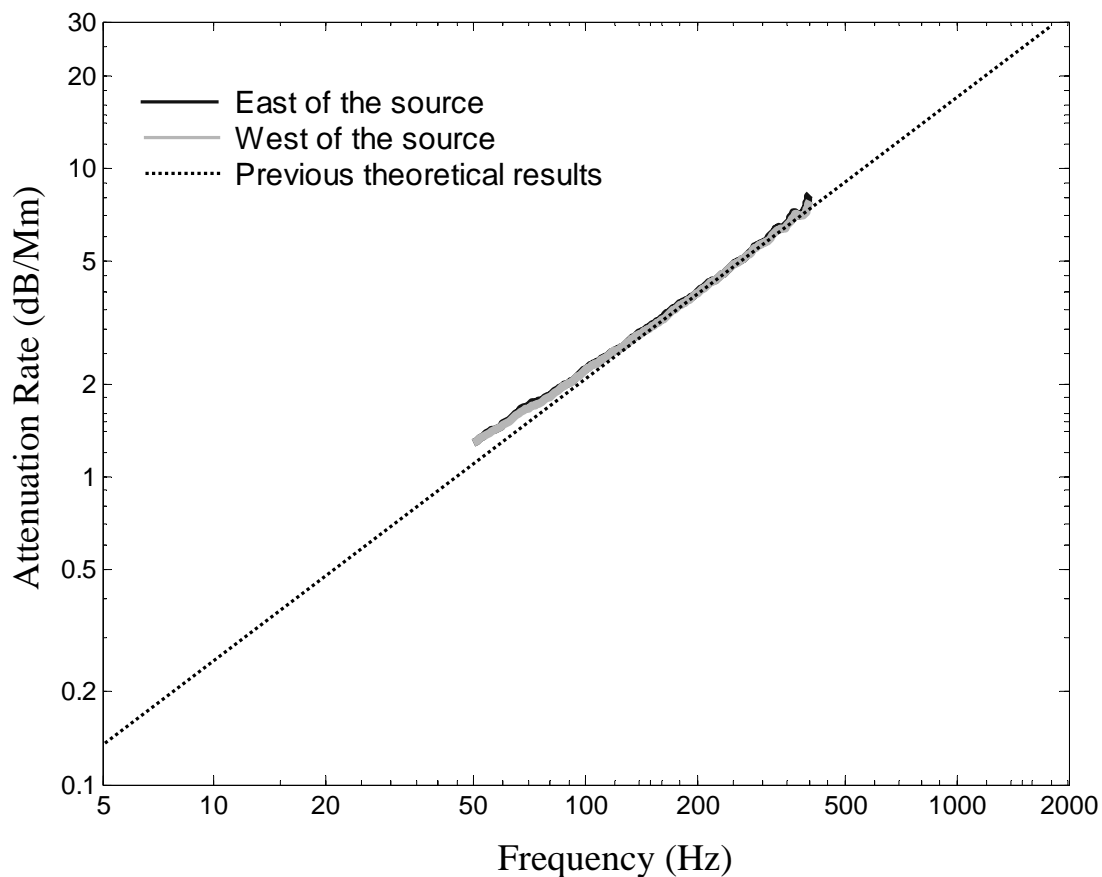
Figure 20 Comparison between the FDTD-calculated daytime ELF propagation attenuation versus frequency between the ¼ and ½-way points to the antipode both east and west of the source along the equator with the theoretical results reported in [77]. For both propagation paths, agreement to within about ±0.5 dB/Mm is achieved over the frequency range of 50 – 500 Hz.

5   FDTD Earth-Ionosphere Waveguide Model Applications

5.1   Hypothesized Pre-Seismic Lithosphere Sources and Radiation

This Section reports the application of the global latitude-longitude FDTD model presented in Section 3.2 and validated in Chapter 4, to modeling hypothetical pre-seismic EM phenomena. First, details and results of FDTD modeling of horizontal electrokinetic currents in the Earth's crust are presented. That study represents the first computational solution of the full-vector Maxwell's equations for pre-seismic EM phenomena and has been published in *Geophysical Research Letters* [79]. Subsequently, FDTD modeling of both horizontal and vertical (radial) current sources in the Earth's crust are compared. A journal article including details and results of this latter study is currently being prepared for submission to *IEEE Geoscience and Remote Sensing Letters*.

Anomalous EM wave phenomena occurring prior to major earthquakes have been of particular interest for many years [12, 13]. A number of physical mechanisms related to hypothetical earthquake precursors have been proposed to explain the origin of such observations [12]. The existence and nature of any EM signatures associated with these mechanisms currently remains unproven and unclear, however. For example, analyses of potential signatures were presented in [80, 81], but [80] neglected wave propagation and [81] was a simple, scalar 2-D analysis that neglected the Earth's curvature. Therefore, the goal for the EM modeling work of this Section is to provide a more rigorous analysis of the hypothetical EM earthquake precursors than previously published, thus placing such phenomena on a firmer physical basis.

For this investigation, the entire-Earth FDTD numerical model calculates EM emissions generated by electrokinetic currents located near the hypocenter of the 1989 Loma Prieta earthquake along the San Andreas Fault. Such currents have been proposed to explain one of the primary examples of hypothetical precursory EM phenomena to date: the anomalous magnetic fields reported by Fraser-Smith et. al. prior to the Loma Prieta earthquake [82]. In this study, the FDTD surface magnetic field calculations are compared to analytical results and measurements previously reported in the literature. In particular, the FDTD-calculated spectra are shown to agree qualitatively with those reported by Fraser-Smith et. al [82].

Details of the Electrokinetic Study

The proposed electrokinetic currents sources modeled in this study in the Earth's crust are believed to arise when fluid flows through a porous medium in the presence of an electrical double layer at a solid-liquid interface [12]. Fenoglio et al. [83] previously modeled electrokinetic currents using a Biot-Savart model to explain the behavior of the anomalous precursory EM data reported by Fraser-smith et al. prior to the Loma Prieta earthquake [82]. For their study, they used a layered half-space geometry to characterize the surface magnetic fields directly above the electrokinetic currents. Subsequently, Majaeva et. al. modeled electrokinetic currents using a layered cylindrical model that also accounted for diffusion [84].

The FDTD results presented here are a more rigorous calculation of electrokinetic EM emissions relative to [83, 84]. This is because the full-vector Maxwell's equations are solved taking into account the complete physics introduced by impulsive wave propagation through a conductive Earth and subsequent round-the-world propagation. This reverberation within the Earth-ionosphere cavity has been shown to make an important contribution at frequencies below

1 kHz [9]. As for the validation study of Chapter 4, the model utilizes topographic and bathymetric data from the NOAA-NGDC "Global Relief CD-ROM" [74]. These data are mapped onto our 3-D space lattice with an assumed resolution of 40 x 40 x 5 km at the equator.

For the lithosphere, conductivity values are assigned according to [75] (see Fig. 15), depending upon the location of the E component (i.e., below an ocean or within a continent). For the atmosphere, both day- and nighttime exponential conductivity profiles used in [76] are assumed, with early evening (the timing of the Loma Prieta earthquake) occurring along the San Andreas Fault.

In [83], Fenoglio et. al. modeled a current associated with fluid flow into a 200 m by 1000 m shear fracture at a depth of 17 km. According to their model, repeated pulses are generated by successive 25-m fractures along the 200 m-long compartment. In the present study, one such pulse is simulated to occur along a 17-km-deep horizontal electric field at 121.88° W, 37.04° N, near the hypocenter of the Loma Prieta earthquake. This is essentially the space-time Green's function of the global Earth-ionosphere waveguide as excited at the hypocenter. To ensure a smooth onset of the excitation, the current is assumed to linearly increase to its maximum value at $1000\Delta t$, where $\Delta t = 3.0\ \mu s$.

The present grid resolution at 40 x 40 x 5 km requires the 25-m current source to be modeled onto a 40-km-long electric field component. This does not, however, upset the calculated surface magnetic field values after normalization. In fact, the resulting surface magnetic field due to successive 25-m fractures along the 200 m-long compartment can be found by modeling multiple current signals on the same buried horizontal electric field component. This is due to the alignment of the current sources along the same general direction, allowing each to contribute linearly in the far-field to the overall dipole moment. The total surface

magnetic field due to any number of cascading, parallel pulses occurring within the span of one grid-cell component is therefore simply the superposition of multiple time-delayed versions of the response caused by a single electrokinetic current source.

Discussion of Electrokinetic Modeling Results

The results of the FDTD model are now presented. Fig. 21 shows the time-waveforms of the horizontal surface *H*-field component generated by a single electrokinetic pulse at a depth of 2.5 km and 17 km. Using the Lemieux parallel processing supercomputer at the Pittsburgh Supercomputing Center, the initial 25 seconds are calculated using the FDTD model, and thereafter Prony's method [85] is applied to extend the tail of the response to its ultimate decay. The time waveform generated by the 17-km-deep source is subsequently used as an equivalent Green's function in the discussion below. Interestingly, the late-time response of the deeper source is higher due to the longer diffusion time within the lossy crustal medium.

Fig. 22 compares the normalized time waveform of the response of the horizontal surface *H*-field component due to eight successive 17-km-deep electrokinetic current pulses as reported in [83] (calculated using a simple Biot-Savart model), with the predictions of the FDTD Maxwell's equations model. For both sets of results, each current source pulse occurs after a time delay of about 1.65 seconds. As shown in Fig. 22, the Maxwell's equations model yields a vastly different temporal response. This difference is likely to have two primary and interlinked causes: (i) The FDTD Maxwell's equations model properly accounts for temporal integration due to EM diffusion through 17 km of lithosphere; (ii) The FDTD Maxwell's equations model properly accounts for reverberation within the Earth-ionosphere waveguide, which has low propagation loss below 0.2 dB/Mm for frequencies below 10 Hz [77]. In this manner, the

instantaneous response of the surface *H*-field is properly influenced by current sources occurring

much earlier in time.
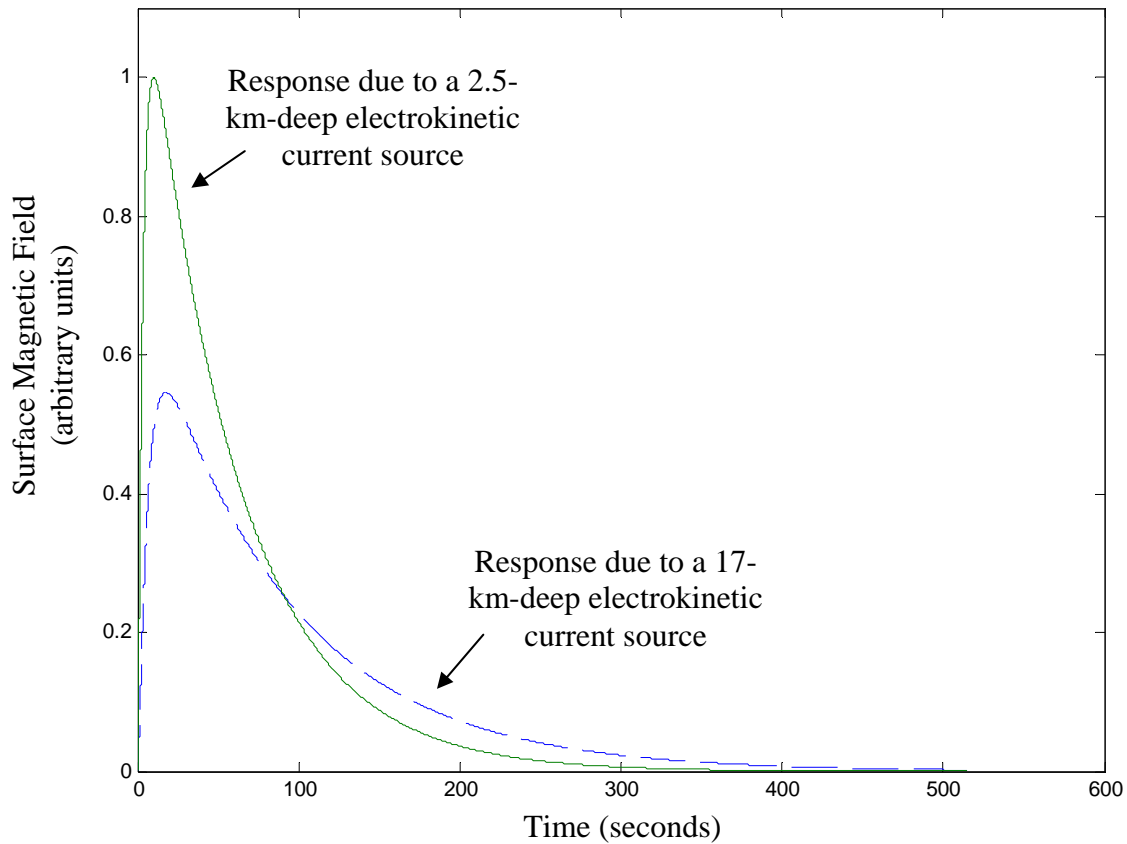
Figure 21 Comparison of the FDTD-calculated time waveforms for the horizontal surface *H*-field component resulting from one electrokinetic current source: (1) 17-km-deep; and (2) 2.5-km-deep.
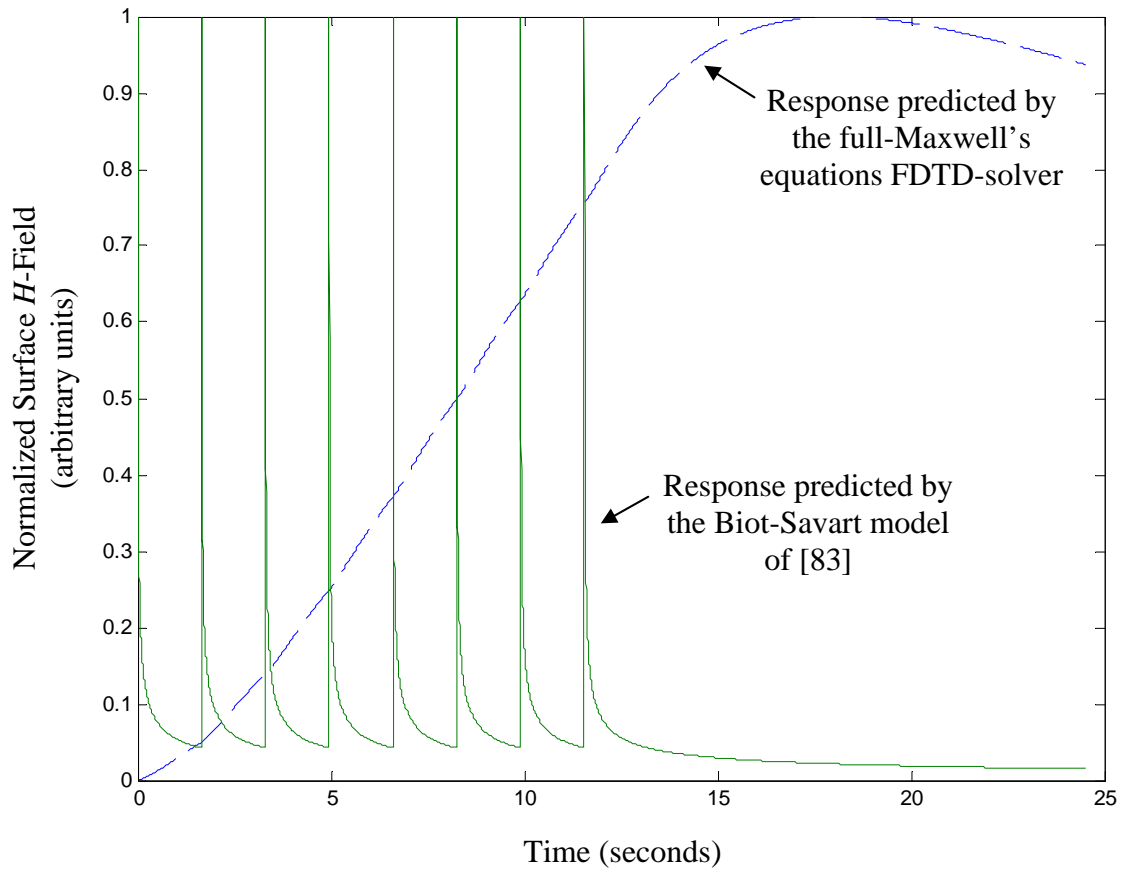
Figure 22 Comparison of the time waveforms for the horizontal surface magnetic field component due to 17-km deep electrokinetic currents associated with eight successive 25-m fractures occurring 1.65 seconds apart along a 200 m-long compartment: (1) as predicted by the Biot-Savart model of [83]; and (2) as predicted by the 3-D FDTD Maxwell's equations model.
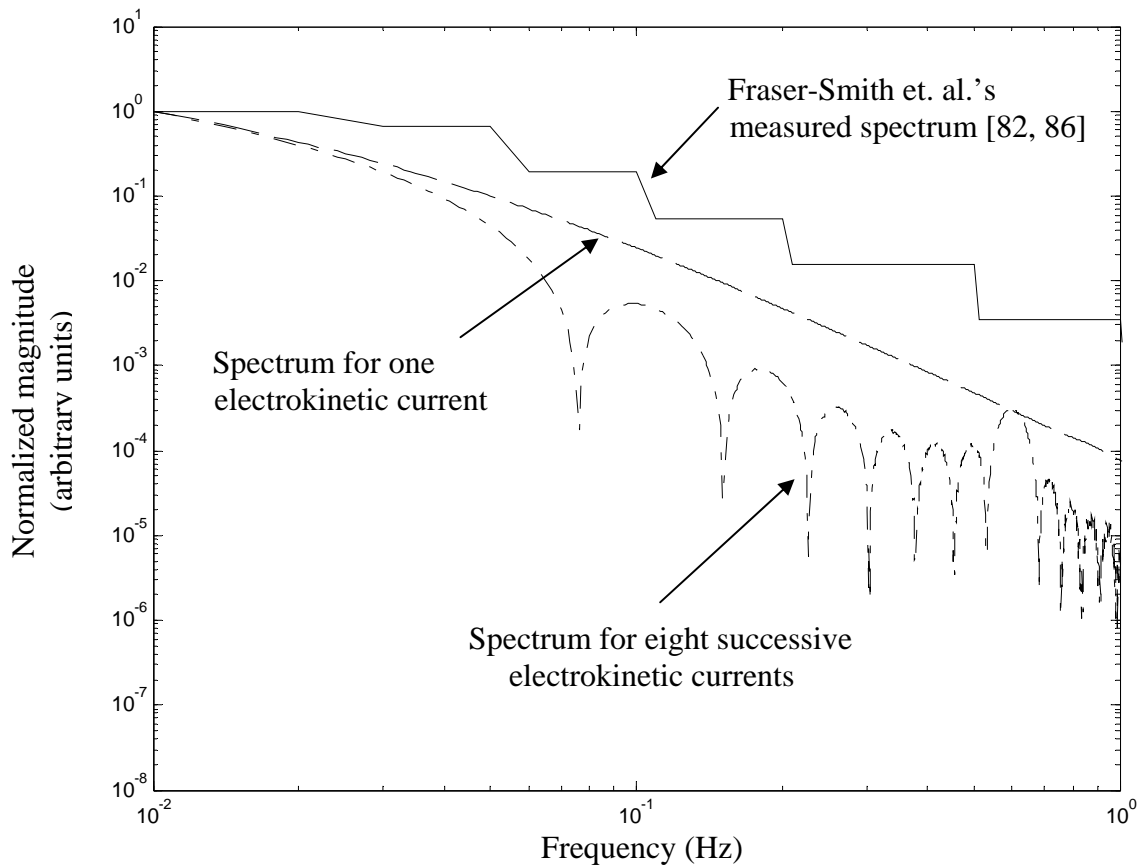
Figure 23 Comparison of the spectra for the horizontal surface *H*-field component: (1)
measured by Fraser-Smith et al. [82, 86]; (2) FDTD result for eight
electrokinetic currents associated with successive 25-m fractures occurring
1.65 seconds apart (corresponding to the comparatively large spectral peak at
0.61 Hz) along a 200 m-long compartment and at a depth of 17-km-deep; and
(3) FDTD result for one electrokinetic current at 17-km depth.

Fig. 23 compares *H*-field frequency spectra from 0.01 – 1.0 Hz for three sets of data: (i) measurements reported by Fraser-Smith et. al. [82, 86]; (ii) FDTD calculation for one electrokinetic current pulse located at a depth of 17 km, as shown in Fig. 2; and (iii) FDTD calculation for eight successive electrokinetic current pulses (at intervals of 1.65 seconds) located at a depth of 17 km. All three spectra are normalized at 0.01 Hz to illustrate their relative rates of decay with increasing frequency, and are graphed on a common logarithmic frequency and amplitude scale. There is qualitative agreement of the measured and calculated results. Assuming that the hypothesized electrokinetic current actually underlies the Fraser-Smith et. al. observations, the deviations between the FDTD-calculated spectra and the measurements have two probable causes: (i) assumption of a lithospheric conductivity in the FDTD model that exceeds the actual value; and (ii) a measurement artifact reported by Fraser-Smith et. al. wherein instrumentation saturation likely occurred at the lowest observed frequencies [82]. In the first case, an excessive lithospheric conductivity would cause the FDTD-calculated spectra at higher frequencies to be unduly attenuated, thereby bending the calculated curves downward below the Fraser-Smith et. al. data. In the second case, the Fraser-Smith et. al. data point at 0.01 Hz would have too small a value, thereby unduly flattening their measured spectra.

Details of the Horizontal / Vertical Lithosphere Current Sources Study

In recent publications [87, 88, 89], the orientation of proposed pre-seismic lithospheric current sources has been called into question. Some of the proposed mechanisms of EM phenomena prior to earthquakes require vertical (radial) electric currents in the Earth's crust, rather than a horizontal orientation as assumed above for the electrokinetic study. For example, the orientation may depend on the direction of the stick-slip plane [87]. Or, as laboratory rock-

crushing experiments by Dr. Freund at NASA Ames Research Center has suggested, holes could be produced in the Earth's crust due to increasing stress that propagate towards the Earth's surface, while electrons flow down into the Earth's hot mantle, yielding a vertically-oriented current [88, 89].

In this study, propagation characteristics for different orientations of a lithospheric current source are investigated. Specifically, the surface horizontal magnetic field is recorded and compared for both horizontal and vertical current sources at a depth of 17 km in the Earth's crust. The source function used in the above electrokinetic study is employed (that of a single electrokinetic current), and the current source is again assumed to occur at 121.88° W, 37.04° N, near the hypocenter of the Loma Prieta earthquake.

Discussion of Horizontal / Vertical Current Modeling Results

Fig. 24 presents the surface horizontal magnetic field time-waveform for three cases of the lithospheric current source: (a) 2.5-km deep, horizontally-aligned (as also shown in Fig. 21); (b) 17-km deep, horizontally-aligned (as also shown in Fig. 21); (c) 17-km deep, vertically-aligned. All three are normalized relative to the peak of the 2.5-km deep, horizontally-aligned waveform. Also, Prony's method [85] is applied, as in the above electrokinetic study, to extend the tail of the response to its ultimate decay. As shown in Fig. 24, the observed time-waveform at the Earth's surface varies significantly depending upon the depth and the orientation of the current source. For example, the peak of the received waveform is delayed not only for deeper sources, but also for vertically aligned sources relative to horizontal sources.

Fig. 25 compares *H*-field frequency spectra from 0.01 – 1.0 Hz for the three data sets from Fig. 24. All three spectra are normalized at 0.01 Hz relative to the 2.5-deep, horizontally aligned

current source results. As seen in Fig. 25, propagation through the Earth's crust yields a low-pass filtered waveform at the Earth's surface. Further, orienting the current in the vertical direction introduces additional losses.
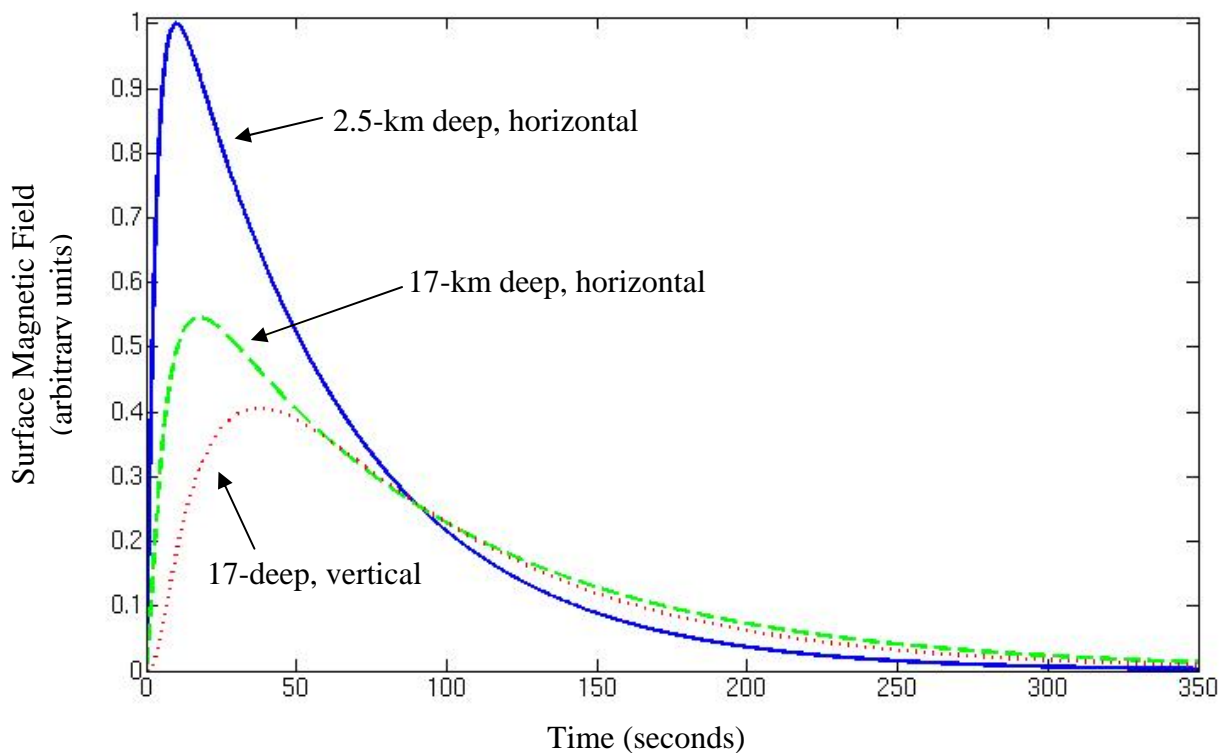
Figure 24 Comparison of the FDTD-calculated time waveforms for the horizontal surface *H*-field component resulting from one current source: (a) 2.5-km-deep and horizontally aligned; and (b) 17-km deep and horizontally aligned; and (c) 17-km deep and vertically aligned.
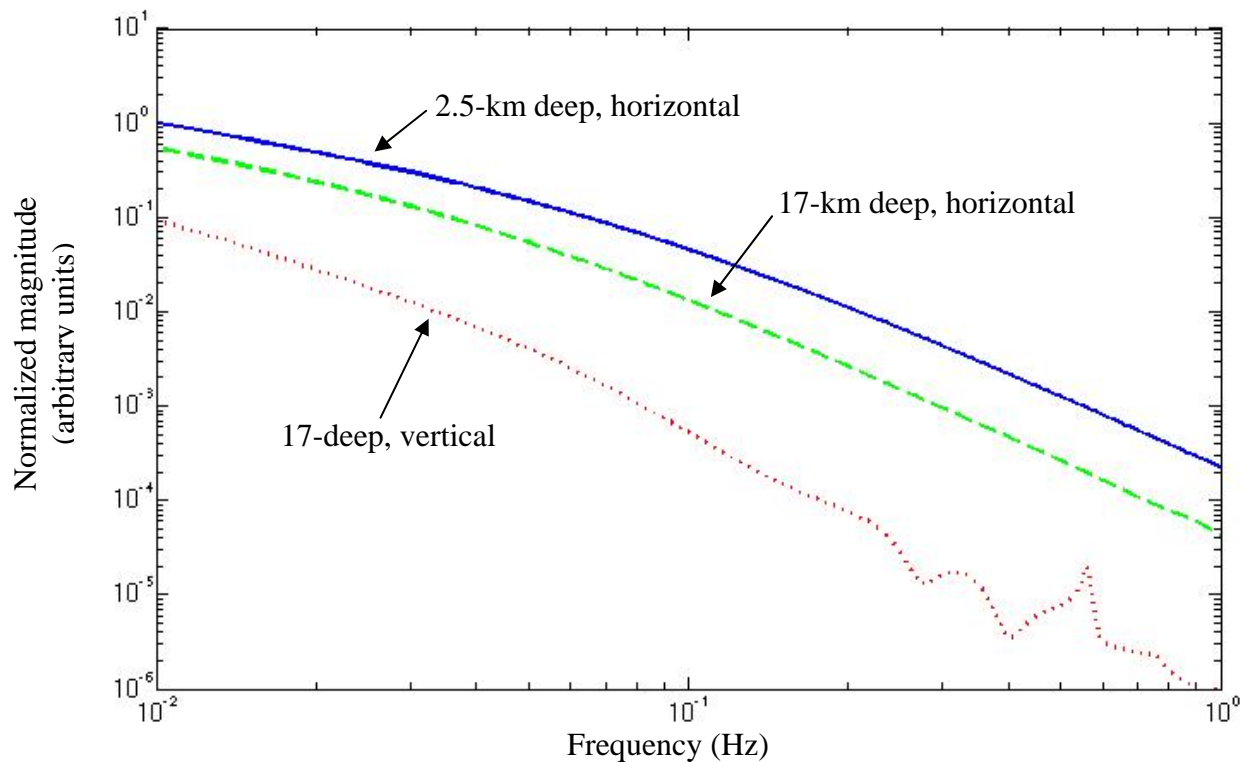
Figure 25 Comparison of the spectra for the horizontal surface *H*-field component: (a) one current source 2.5-km deep and horizontally aligned; (b) one current source 17-km deep and horizontally aligned; and (c) one current source 17-km deep and vertically aligned.

5.2   Detection of Underground Resource Formations

This Section reports the application of the global geodesic FDTD model presented in Section 3.3 and validated in Chapter 4, to modeling remote sensing of a hypothetical Alaskan oil field. This study has been published in *IEEE Transactions on Antennas and Propagation* [73], as well as in *IEEE Geoscience and Remote Sensing Letters* [90] using the latitude-longitude FDTD model

Over many decades, several methods have been developed to perform subsurface conductivity measurements for locating and characterizing natural resources (see for example the extensive survey in Ref [91]). Only very few of the existing methods, however, can probe very deep into the Earth's crust, and fewer still employ controlled sources. In this paper, we are interested in techniques capable of exploring deep within the Earth's crust (up to ~15 km) using well-characterized controlled (man-made) sources, as opposed to natural sources having a random occurrence and random properties. Previously, controlled sources such as power lines, electrified railroads, and pulsed magnetohydrodynamic (MHD) generators have been used for such probing [9]. However, the data obtained from these methods exhibits an unsatisfactory, wide variance [9]. Further, the above techniques can only be applied at considerable cost and effort, making their implementation infeasible in many regions of the world. As a result, new approaches to deep EM geophysical prospecting are desirable. If a superior technique applicable on a global scale were developed, it could permit both rapid and inexpensive surveying of the entire Earth's crust. Such a method would be of particular interest for locating anomalous conductivity structures such as mineral deposits and major oilfields.

Since the early 1990's a promising new system for global remote sensing at frequencies below 300 Hz has been under investigation [9, 10]. The advantages of using sub-300 Hz frequencies for this type of application are as follows:

(1) Sufficiently large skin depth for deep probing (100 m in ocean and 10-15 km in crystalline shields).

(2) Low propagation attenuation, which could provide global remote sensing of the Earth with a single source.

(3) Good stability compared to higher frequency methods that are more influenced by ionospheric disturbances.

Due to these favorable properties, Velikhov et. al. introduced the idea of simultaneously performing studies around the globe involving oil-bearing rock, seismic regions, ionospheric wave propagation, and other areas of geophysics using one powerful source [9].

The sounding methodology described in [9, 10], however, involves electromagnetic field impedance measurements to determine the resistivity of the underlying rock. This requires measurement of both the tangential electric field, E_{tan}, and the tangential magnetic field, H_{tan}, near the Earth's surface. In this Section, a novel subsurface radar requiring detection of only the radial magnetic field, H_r, is proposed for detecting the presence of major oil deposits. This new radar assumes operation of a powerful distant antenna transmitting pulses at frequencies below 76 Hz.

To illustrate the capabilities of the proposed oilfield radar, FDTD calculations for radar returns are performed for a hypothetical Alaskan oilfield excited by a 20-Hz pulse emitted from the former U.S. Navy transmitting site in Wisconsin. The goal for this study is to determine how the presence of a major oil field influences the surface H-field components. The surface H_r is shown to exhibit an unexpected and very high degree of sensitivity to the presence of deeply buried conductivity anomalies of the lithosphere, much more so than H_{tan} [90]. This

phenomenon may be exploited to establish a means to rapidly and inexpensively conduct aerial surveys of thousands of square km for significant oilfields [73, 90].

Details of the Oil Field Remote-Sensing Study

For this study, an oil field is modeled as a lithosphere conductivity anomaly having lateral area of 4800 km^2 and thickness 1.25 km located in Alaska at 156° W, 69° N (subgridding [14] is used to refine the radial grid resolution in the lithosphere near the Earth's surface to 1.25 km, a factor of 4 times finer than the nominal radial resolution of 5 km used in the atmosphere and deeper within the lithosphere). The anomaly is assumed to have a conductivity that is ten times lower than that of the surrounding strata. By way of comparison, Alaska's Kuparuk River oil field spans a lateral area of about 1000 km^2 [92], but this radar technique has been shown to be successful for detecting conductivity anomalies of that size [90].

For the distant transmitter, the Wisconsin Transmitting Facility (WTF) is employed at a distance of about 4.4 Mm from the lithosphere conductivity anomaly in Alaska. The WTF is a section of the former Navy's submarine communication system (in operation until September 2004 [93]) near Clam Lake, WI (90.9° W, 46.5° N). Nominal operation of this facility is assumed, with two orthogonal ground lines, each 22.5 km long and carrying a current of 300 A, one oriented in the north-south direction and the other in the East-West direction. However, the assumed carrier frequency is 20 Hz, rather than the 75-Hz Navy frequency. Further, the transmitted signal is a pulse generated by double-sideband amplitude modulation of the 20-Hz carrier by a Gaussian envelope waveform of full-width at half-maximum 42.5 msec. Below the WTF, the Laurentian Plateau (or Canadian Shield), a large region of low-conductivity rock of

2.4E-4 S/m that extends northward from the Great Lakes toward the Arctic Ocean and includes much of Canada and Greenland, is modeled.

Two separate FDTD models are used to calculate the time-waveforms of the H_{tan} and H_r components at a point P at the Earth's surface directly above the conductivity anomaly. Model A serves to provide the reference time-waveforms (i.e., no conductivity anomaly present). Model B provides the time-waveforms for the case of the conductivity anomaly assumed to be located at a median depth of 1.2 km. As for the validation study of Chapter 4, both models utilize topographic and bathymetric data from the NOAA-NGDC "Global Relief CD-ROM" [74]. These data are mapped onto the 3-D space lattice with a resolution of about 63 x 63 x 5 km. For the lithosphere, conductivity values are assigned according to [75] (see Fig. 15), depending upon the location of the E component (i.e., below an ocean or within a continent). For the atmosphere, both day- and nighttime exponential conductivity profiles used in [76] are assumed. In addition, both models include conductivity values for the Laurentian Plateau mapped into the North American continental model.

Discussion of Results

The results of the FDTD models are now presented. First, the normalized field-perturbation waveform $\Delta H(t)$ due to the conductivity anomaly is defined as the absolute value of the difference between the time-waveforms of Models A and B divided by the peak value of the Model-A waveform. Using a decibel scale, Fig. 26 shows the calculated results for $\Delta H(t)$ at surface observation point P due only to the 4800 km^2 conductivity anomaly at a median depth of 1.2 km. The following two cases are illustrated: (a) $\Delta H_{tan}(t)$; (b) $\Delta H_r(t)$. It is shown

that $\Delta H_{tan}(t)$ is weaker than the reference H_{tan} by more than 25 dB at almost every time point. On the other hand, $\Delta H_r(t)$ can be as much as 20 dB stronger than the reference H_r. Combined with the FDTD calculations showing that $\Delta H_{tan}(t)$ and $\Delta H_r(t)$ are comparable in strength for the modeled conductivity anomaly, measuring H_r perturbations can yield an approximate 45 dB improvement in sensitivity relative to measuring H_{tan} perturbations. Therefore, since H_{tan} is required for the impedance measurement technique reported in [9, 10], Fig. 26 indicates that the sensitivity of the impedance technique is considerably less than afforded by a measurement of the H_r perturbation. Furthermore, analogous FDTD studies involving deeper conductivity anomalies show that measuring the H_r perturbation becomes increasingly superior for such structures located at greater depths. Given the present results and those of [10], it appears possible to detect H_r perturbations for conductivity anomalies located as deep as 10 – 20 km.

Implications for a Possible Detection System

One implication of the results shown in Fig. 26 is that a powerful, distant antenna operating at frequencies below 76 Hz can be used to locate oil-bearing rock within several km of the Earth's surface by measuring the highly sensitive surface H_r. Therefore, it is proposed here that a source such as the WTF can be used in conjunction with an airborne magnetometer having sufficient sensitivity to H_r to rapidly and inexpensively detect oilfields over thousands of square km [73, 90]. In fact, considering the very low propagation attenuation of electromagnetic waves in this frequency range (as shown in Figs. 18 and 20), employing a sufficiently powerful antenna permits use of this sounding technique on a global scale.
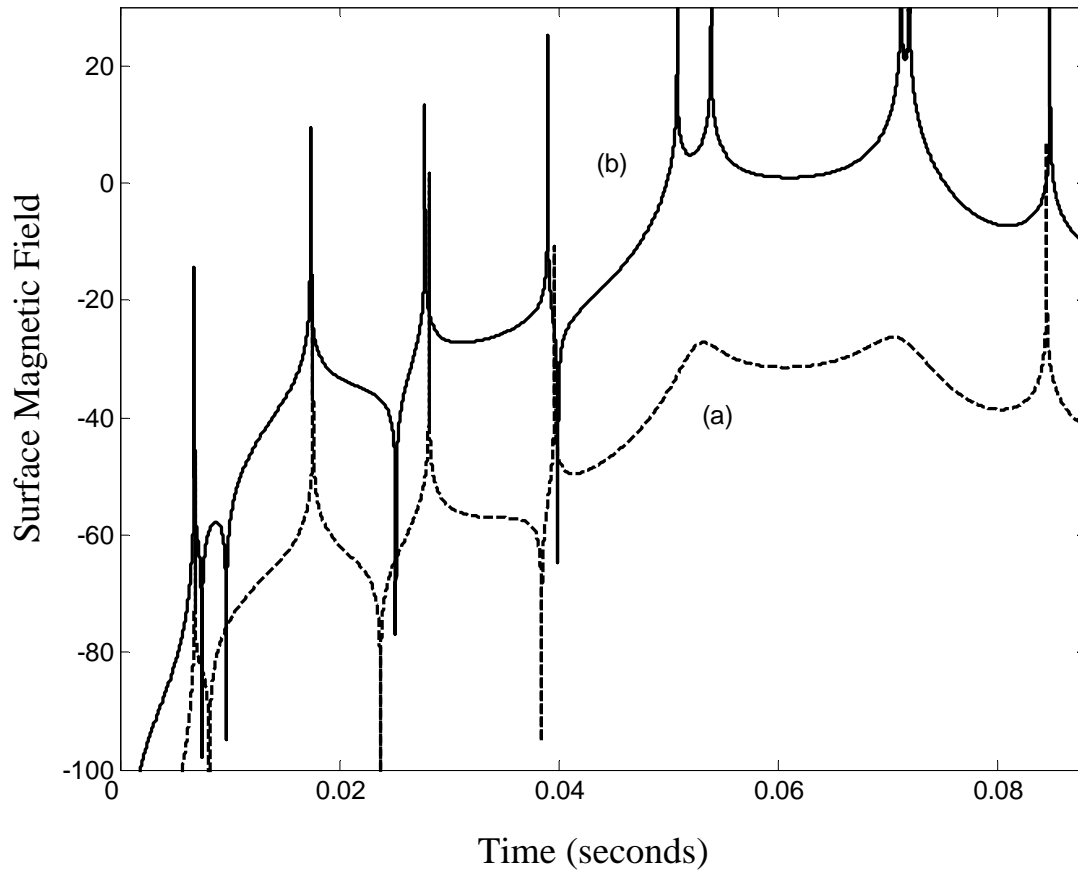
Figure 26 Comparison of the FDTD-calculated results for the absolute values of the normalized field-perturbation waveform ΔH(t) at surface observation point P due only to the 4800 km^2 conductivity anomaly at a median depth of 1.2 km. The following two cases are illustrated: (a) ΔH_{tan}(t); (b) ΔH_r(t). The spikes are due to zero-crossings of the reference time-waveforms (i.e. without the conductivity anomaly present) used to normalize the field-perturbation waveforms.

SQUID magnetometers are proposed for the aerial surveys described here because they: (1) measure the magnetic field directly; (2) offer higher sensitivity at frequencies less than 150 Hz than other receiver technologies, and (3) provide higher bandwidths [94]. Further, they have already been successfully implemented in aerial surveys [94].

5.3   Remote Sensing of Localized Ionospheric Anomalies

This Section reports the application of the global geodesic FDTD model presented in Section 3.3 and validated in Chapter 4, to modeling remote sensing of localized ionospheric conductivity depressions above Los Angeles, CA. This study has been submitted for publication to *IEEE Geoscience and Remote Sensing Letters* [95].

Despite substantial ground and satellite-based technology for studying the upper ionosphere, extracting the electron densities versus height in the D-region (< 95 km) is still a difficult problem, particularly at night [96]. As a result, monitoring and understanding anomalous behavior of the D-region due to geophysical, solar, or other phenomena is not a well-developed field of science. To date, techniques for studying the D-region have included in-situ measurements by rockets [97], or studying the spectrum from uncontrolled (random, naturally occurring) sources, such as intense lightning discharges [96]. These methods, however, have limited range, do not offer a practical means of continuously monitoring the lower ionosphere, and are difficult or impossible to implement in many regions of the world.

A few examples exist of probing the D-region using controlled (man-made) radio frequency sources. For example, continuous-wave signals propagating in the Earth-ionosphere waveguide from communication and navigation systems have been analyzed to infer if any ionospheric anomalies exist between the source and receiver [98, 99].

In this Section, a novel radar working at 76 Hz is proposed for locating and characterizing localized ionospheric anomalies that have been formed within ~100 km of the Earth's surface by natural geophysical processes. This system assumes operation of the former U.S. Navy WTF as a distant, well-characterized, impulsive source to illuminate the ionospheric anomaly, and passive detection of the resulting vertical electric (E_r) field time-waveform at the Earth's surface

in the vicinity of the ionospheric anomaly. (Note that the ELF illumination is assumed to be of sufficiently low power to have negligible heating or any other effects upon the ionospheric anomaly.) Employing a man-made impulsive source such as the WTF could allow a continuous and systematic monitoring scheme that avoids variabilities arising from naturally occurring sources such as lightning, which have random properties.

To illustrate the operation of the proposed radar, the vertical *E*-fields are calculated using FDTD at the Earth's surface in Los Angeles, CA below three cases of bowl-shaped ionospheric conductivity depressions. The depressions are assumed to have a depth of 20 km and a radius of either 100 km, 200 km, or 380 km. Remote excitation is provided by a 76-Hz electromagnetic-wave pulse launched essentially isotropically from the WTF. The calculated results show that a simple measurement of the vertical *E*-field signal below a localized ionospheric depression could provide not only its location, but also its size, shape, and depth.

Details of the Ionospheric Anomaly Remote-Sensing Study

For this study, the ionospheric anomalies are located above Los Angeles at 118° W, 34° N. These are assumed to be bowl-shaped ionospheric conductivity depressions having a depth of 20 km and a radius of either 100 km, 200 km, or 380 km.

For the distant transmitter, the WTF is employed at a distance of ~2.8 Mm from the ionospheric depression above Los Angeles. Nominal operation of the WTF is assumed, with two orthogonal ground lines, each 22.5 km long and carrying a current of 300 A, one oriented in the North-South direction and the other in the East-West direction. The transmitted signal is a pulse generated by the double-sideband amplitude modulation of a 76-Hz carrier by a 43-msec Gaussian envelope waveform (full-width at half-maximum). Below the WTF, the Laurentian

Plateau (or Canadian Shield), a large region of low-conductivity rock of 2.4E-4 S/m that extends

northward from the Great Lakes toward the Arctic Ocean and includes much of Canada and

Greenland, is modeled.

Two separate FDTD models are used to calculate the time-waveforms of the surface E_r

component. Model A serves to provide the reference time-waveforms (i.e., no ionospheric

anomaly present). Model B provides the time-waveforms for the case of the ionospheric

anomaly present. As for the validation study of Chapter 4, both Models A and B utilize

topographic and bathymetric data from the NOAA-NGDC "Global Relief CD-ROM" [74].

These data are mapped onto each 3-D space lattice with a resolution of about 63 x 63 x 5 km.

For the lithosphere, conductivity values are assigned according to [75] (see Fig. 15),

depending upon the location of the E component (i.e., below an ocean or within a continent). In

addition, both models include conductivity values for the Laurentian Plateau mapped into the

North American continental model.

For the atmosphere, both day- and nighttime exponential conductivity profiles used in [76]

are assumed, with dawn occurring at 0° longitude. The effective waveguide height of reflection

for these profiles is approximately 48 km at day and 76 km at night [76] for the unperturbed

conditions. At the center of the ionospheric depression occurring during the night above Los

Angeles, the effective waveguide height of reflection is about 56 km.

Discussion of Results

The results of the FDTD models are now presented. First, the percent increase in the peak

vertical E-field power ΔP due to the ionospheric depression is defined as the absolute value of

the difference between the square of the peak surface E_r value of Models A and B divided by the

square of the peak surface E_r value of the Model-A waveform. Fig. 27 is a map of the calculated

ΔP for the 100-km radius, 20-km deep ionospheric depression above Los Angeles. From Fig.

27, we observe an ~4.5% maximum perturbation of the incident signal due to the ionospheric

depression. Fig. 27 also illustrates that both the size and shape of the ionospheric anomaly can

be determined using an array of passive E-field detectors at the Earth's surface.
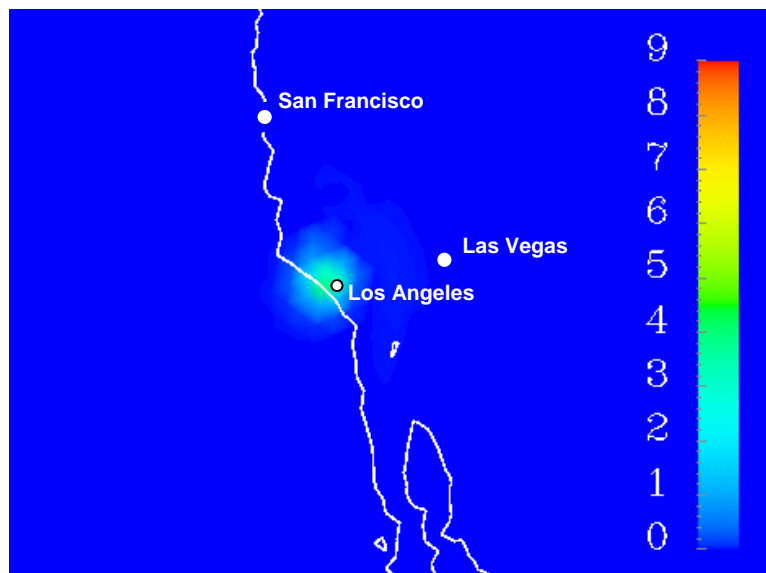
Figure 27 Map of the percent increase in the peak vertical E-field power ΔP for the
bowl-shaped, 100-km radius, 20-km deep ionospheric depression above Los
Angeles at 118° W, 34° N.

Fig. 28 is a map of the calculated ΔP for the 200-km radius, 20-km deep ionospheric

depression above Los Angeles. We see that there is an ~7.5% maximum perturbation of the

incident signal due to this anomaly. Similarly, Fig. 29 is a map of ΔP for the 380-km radius, 20-

km deep ionospheric anomaly above Los Angeles. Here, we see that there is an ~8% maximum

perturbation of the incident signal due to this anomaly. As for the case of Fig. 27, the ionospheric depressions of Figs. 28 and 29 can be characterized using passive E-field detectors for spatial extent. Further, at any location the downward extent of the depression from the regular ionospheric conditions can be extracted from the perturbation level occurring at that point.
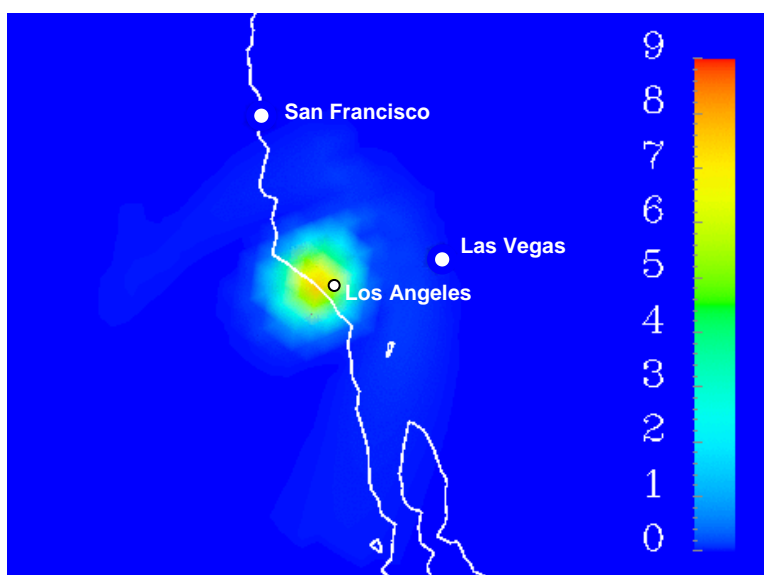
Figure 28 Map of the percent increase in the peak vertical E-field power ΔP for the bowl-shaped, 200-km radius, 20-km deep ionospheric depression above Los Angeles at 118° W, 34° N.

Finally, Figs. 30 and 31 illustrate the calculated surface E_r time-waveform at Los Angeles at 118° W, 34° N for the case of: (1) no ionospheric depression present; (2) a 100-km radius, 20-km deep ionospheric depression above Los Angeles; (3) a 200-km radius, 20-km deep ionospheric depression above Los Angeles; (4) a 380-km radius, 20-km deep ionospheric

depression above Los Angeles. Fig. 30 shows the first 40 msec as the pulse propagates through Los Angeles after radiating from the WTF. Fig. 31 shows an enlarged version of the four cases of Fig. 30 between 22 and 30 msec. For ionospheric depressions of larger radii, the delay of the slow-tail response increases monotonically, as can be seen in Fig. 31. This is yet a second indication of the existence and radius of the ionospheric depression, which can be used in conjunction with measurement of ΔP to strengthen the observation.
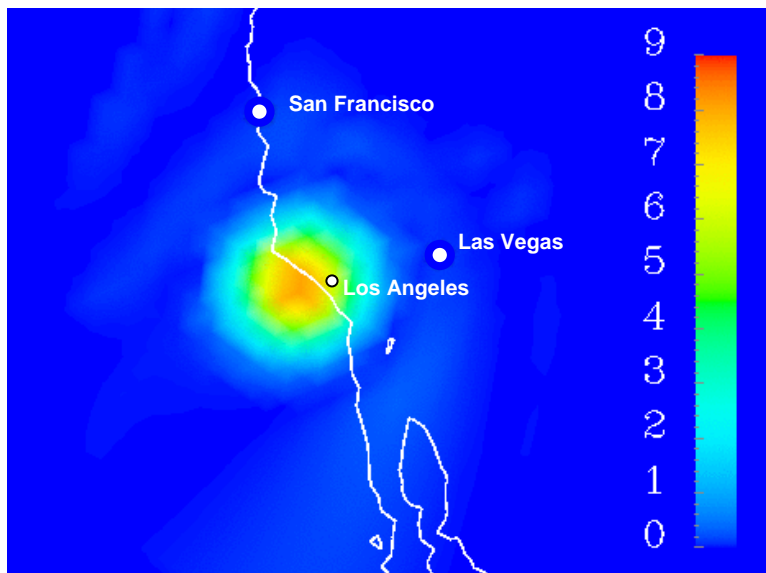
Figure 29 Map of the percent increase in the peak vertical E-field power ΔP for the bowl-shaped, 380-km radius, 20-km deep ionospheric depression above Los Angeles at 118° W, 34° N.
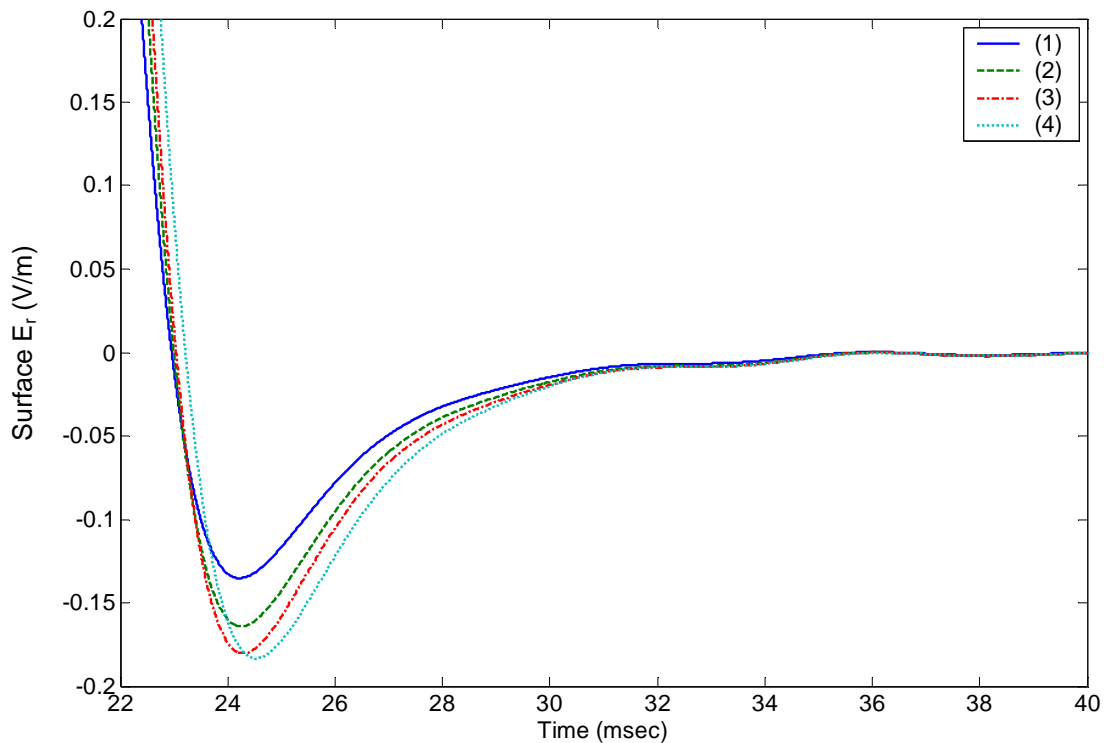
Figure 30 Surface E_r time-waveform at Los Angeles at 118° W, 34° N for the case of: (1) no ionospheric depression present; (2) a 100-km radius, 20-km deep ionospheric depression above Los Angeles; (3) a 200-km radius, 20-km deep ionospheric depression above Los Angeles; (4) a 380-km radius, 20-km deep ionospheric depression above Los Angeles.
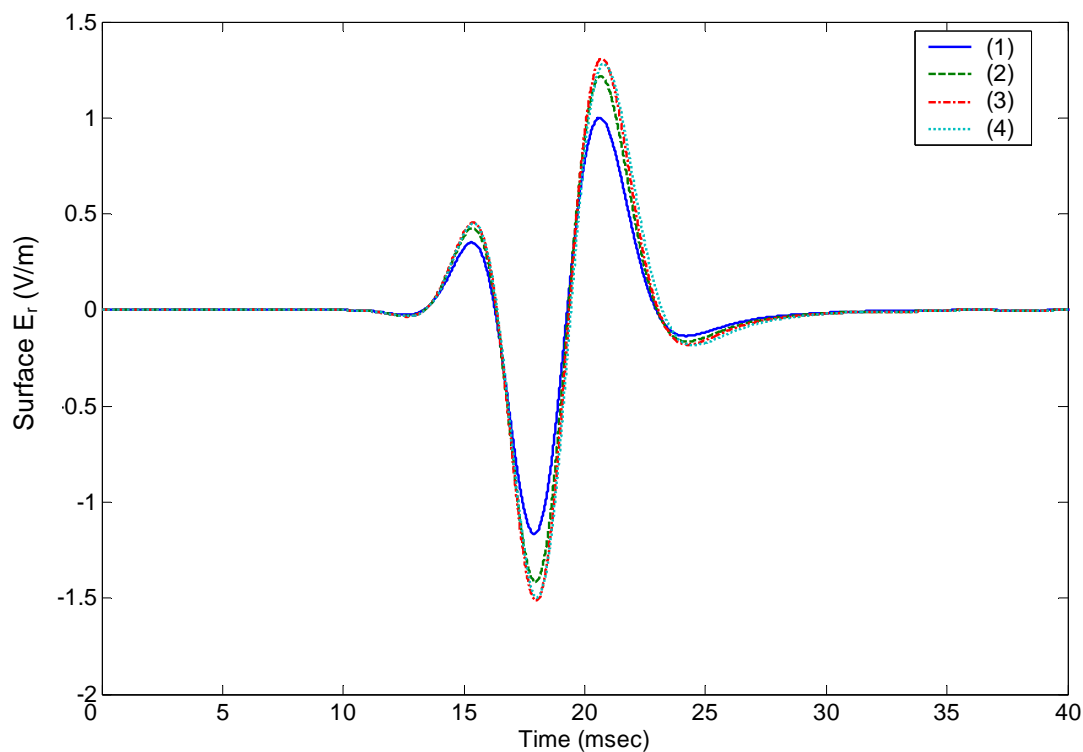
Figure 31 Enlargement of the surface E_r time-waveform slow-tail response at Los Angeles for the four cases shown in Fig. 30. We observe that for ionospheric depressions of larger radii, the delay of the slow-tail response increases monotonically.

Applications of the Proposed Radar System

Several practical applications exist for the proposed radar system for ionospheric anomalies. For example, it has been proposed that the electron density at altitudes of the nighttime ionospheric D region increases considerably above earthquake preparation zones (see for example [100, 101]. This increase in electron density, hypothesized to exist prior to earthquakes

having magnitude $M \geq 5$, can be equated to a lowering of the effective height of the ionosphere, with the radius of the anomaly dependent upon the magnitude of the impending earthquake [100]. However, although there is much literature on this subject, there is no current understanding of potential interactions between earthquake preparation processes and the lower ionosphere. The radar system proposed here could therefore provide useful information regarding localized ionospheric depressions hypothesized to occur as earthquake precursors. Additional applications include remote sensing of ionospheric conditions related to other geophysical processes as well as radio propagation. Further, this application involving the WTF complements (could be used in conjunction with) the radar for major oil deposits discussed in Section 5.2.

5.4   Propagation from Lightning with a Gyrotropic Ionosphere Plasma

This Section reports the first full-vector 3-D FDTD model of the Earth-ionosphere waveguide incorporating a magnetized gyrotropic ionosphere plasma influenced by the Earth's magnetic field. This work represents a major advance over the isotropic ionosphere model employed in all of the previous work discussed in this Chapter, and is being prepared for submission to *IEEE Transactions on Antennas and Propagation* [102].

The ionosphere is known to be highly anisotropic due to the action of the Earth's geomagnetic field upon its constituent plasma of electrons (and to a lesser degree, its constituent plasma of positive ions) [23]. As shown in the previous work discussed in this dissertation, an isotropic ionosphere having an exponential conductivity profile appears to be adequate in calculating the average propagation of EM waves of frequencies less than 1 kHz over many thousands of km [67]. However, its inability to incorporate such effects as Faraday rotation limits its accuracy in calculating details of higher-frequency EM fields radiated by lightning and sprites within a range of 1000 km of the atmospheric excitation. Such details are important since they allow, in principle, remote sensing and characterization of these phenomena.

In this Section, sub-30 kHz electromagnetic wave propagation is simulated in a 3-D latitude-longitude FDTD grid having a frequency-dispersive, anisotropic ionosphere plasma. Specifically, wave propagation characteristics are obtained for an electromagnetic pulse radiated over a distance of 500 km by a vertical lightning channel for three different cases: (a) Earth's magnetic field transverse to the direction of propagation; (b) Earth's magnetic field parallel to the direction of propagation; and (c) Earth's magnetic field parallel to the direction of propagation but with a 100-km radius, 20-km deep bowl-shaped lowering of the ionosphere interposed between the lightning channel and the observation point.

Details of the Gyrotropic Ionospheric Plasma Study

To generate a 3-D Earth-plasma ionosphere model, data for the geomagnetic field must be integrated into an FDTD code capable of simulating an inhomogeneous, frequency-dispersive, anisotropic magnetized plasma. Working towards that goal, a standard 3-D FDTD model is coupled to the plasma algorithm published by Lee and Kalluri [103]. This integrated software is first validated for a rectangular grid, and subsequently adapted to the latitude-longitude formulation described in Section 3.2 with a resolution of 1 x 1 x 1 km.

The latitude-longitude FDTD-plasma algorithm is next adapted to model EM wave propagation radiated from a lightning strike over a 500-km segment of the Earth-ionosphere waveguide. Here, the restricted 500-km spatial extent of the grid is necessary because of the need for more significant computational resources when including ionosphere plasma phenomena. Specifically, the anisotropic plasma algorithm of [103] requires for numerical stability a time step approximately three orders of magnitude below that of the numerical stability condition for the latitude-longitude FDTD Earth-ionosphere model of Chapter 4. Thus, as part of future research, the algorithm of [103] will be critically examined to explore alternatives that potentially allow a much larger time step and permit simulations to run significantly faster. The eventual goal will be to extend the Earth-plasma ionosphere model presented in this Section to a global scale, and to also use a time step comparable to that used in the previous work of this chapter and Chapter 4.

In the meantime, for the present study, a 500-km of the Earth-ionosphere system within ±100 km of sea level is modeled using the integrated FDTD-plasma model. The topography is set to sea level at all locations. A constant topography is chosen because EM propagation over a

only 500-km distance is considered, and because it permits isolation of the affects of the ionosphere on the EM propagation characteristics.

For the lithosphere, conductivity values are assigned according to [75] (see Fig. 15), depending upon the depth of the E component below a continent. For the plasma ionosphere, the electron density profile of [104, 105] is employed:

$$N_e(h) = 1.43 \times 10^{13} \exp(-0.15h') \exp[(\beta - 0.15)(h - h')] \qquad (41)$$

where $\beta = 0.5$ km^{-1} and $h' = 84.2$ km are obtained by ionosphere remote sensing [96]. This electron density profile corresponds with that used in Cummer's published 2-D study [23] of lightning generated EM fields using a cylindrical-coordinate FDTD model treating the ionosphere as a cold plasma. Additionally, the electron collision frequency profile versus altitude from [106] is employed:

$$v_e(z) = 1.816 \times 10^{11} \exp(-0.15z) \qquad (42)$$

where z is the altitude measured in km, and v is in units of sec^{-1}.

As the source, the lightning return stroke current waveform of [107] is employed:

$$I(t) = I_0 \frac{v_0}{\gamma} [\exp(-at) - \exp(-bt)][1 - \exp(-\gamma t)] / L \qquad (43)$$

where $I_0 = 20$ kA, $v_0 = 8$ x 10^7 m/s, $\gamma = 3$ x 10^4 s^{-1}, $a = 2$ x 10^4 s^{-1}, $b = 2$ x 10^5 s^{-1}, and L is the lightning discharge channel length [107]. For the present study, L is set to the length of one grid cell, 1 km.

Discussion of Results

To study the wave propagation characteristics of an EM pulse radiated by a vertical lightning channel, the radial (vertical) *E*-field is recorded at a distance of 500 km for separate conditions of the ionosphere and geomagnetic field between the lightning source and the receiver. The three cases considered here are: (a) the Earth's magnetic field transverse to the direction of propagation; (b) the Earth's magnetic field parallel to the direction of propagation; and (c) the Earth's magnetic field parallel to the direction of propagation but with a 100-km radius, 20-km deep bowl-shaped lowering of the ionosphere interposed between the lightning channel and the observation point. Fig. 32 shows the calculated surface radial E-field at the receiver for each of the three cases. The results of Fig. 32 indicate that the received waveform is influenced significantly by the conditions of the Earth's ionosphere and the direction / magnitude of the geomagnetic field.

While conducting the above wave propagation study, it was found that a very late-time instability arises from the plasma algorithm of [103] when modeling the ionosphere plasma. Therefore, various spatial and time-averaging, attenuation, and filtering techniques are currently being applied to the FDTD-plasma model to eradicate this instability.
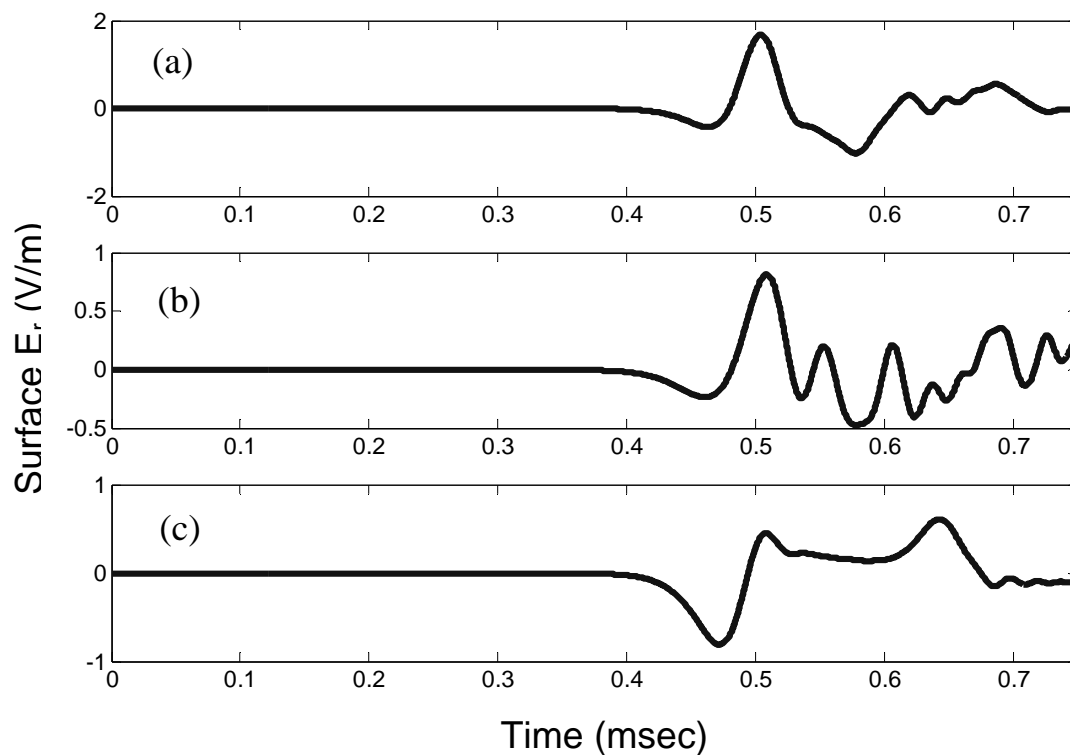
Figure 32 Surface radial E-field time-waveform 500 km from a lightning strike for three different cases: (a) Earth's magnetic field transverse to the direction of propagation; (b) Earth's magnetic field parallel to the direction of propagation; and (c) Earth's magnetic field parallel to the direction of propagation but with a 100-km radius, 20-km deep bowl-shaped lowering of the ionosphere interposed between the lightning channel and the observation point.

6   Summary and Future Research

6.1   Summary

This dissertation addressed FDTD modeling of EM wave propagation below 30 kHz in the Earth-ionosphere waveguide. Both latitude-longitude and geodesic 3-D high-resolution FDTD grids were developed and implemented. Further, using these two generations of grids, four applications were investigated: hypothesized pre-seismic lithosphere sources and radiation, detection of deep underground resource formations, remote sensing of localized ionospheric anomalies, and EM propagation studies including ionospheric plasma phenomena.

The models described in this work represent a major advance over the analytical techniques used for many decades to study EM wave propagation in the Earth-ionosphere cavity. With grid-based FDTD models, significantly more details and complexities can be accommodated than using analytical methods. Thus, as highlighted by Sevgi, Akleman, and Felsen in their article on groundwave propagation [108], FDTD models provide "more realistic approaches" to studying EM propagation within the Earth-ionosphere waveguide over "idealized" analytical techniques. And, as a result, with the increasing "availability of massive computational resources" [108], FDTD modeling of the Earth-ionospohere waveguide will undoubtedly continue to create many new avenues of research beyond those discussed in this dissertation.

6.2   Future Research

This dissertation concludes with a prospectus for future research. One of the primary advantages of FDTD is its ability to model complex, continuously varying, non-homogeneous, and anisotropic media. Thus, an advantageous avenue of research in this area would be to expand the localized Earth-plasma ionosphere model discussed in Section 5.4 to a global model. This could permit inclusion of the worldwide geomagnetic data, and the possibility of integrating the FDTD grid with global ionosphere data models based on satellite and ground-based measurements.

First, advancing to a global Earth-plasma ionosphere model could permit inclusion of an entire-Earth geomagnetic field model, such as that provided by the National Geophysical Data Center and based on spherical harmonics [109]. With the model of [109], the magnetic field vector and its intensity, or the anomaly of the total intensity of the field, can be obtained at any location on the Earth's surface. Its inclusion would yield the first global 3-D EM propagation solver that includes a realistic, continuously-varying anisotropic model of the ionosphere subjected to the Earth's magnetic field.

Second, advancing to a global Earth-plasma ionosphere model could permit inclusion of more comprehensive and detailed grid-based (even time-variable) ionosphere data derived from satellite and earth-based measurements. An integrated model of this type could then be extended into higher regions of the atmosphere, well above the current FDTD model height in the work presented in this dissertation of approximately 100 km, to provide additional advantages. One possibility would be to self consistently link a global FDTD EM simulator to a sophisticated ionosphere model such as the U.S. Naval Research Lab's SAMI3 [110], which tracks the plasma and chemical evolution of seven ion species (H^+, He^+, N^+, O^+, NO^+_2, and O^+_2) in the altitude range of 85 km to 20,000 km. Additional possibilities include linking the FDTD grid to the

ionosphere models of [11, 112]. Realization of such multi-physics EM wave / ionospheric physics models on a global scale would be a valuable tool for advancing the applications discussed in this proposal, as well as additional future applications, and represent a fundamental advancement in geophysics.

References

[1]   J. R. Wait, "Terrestrial propagation of very-low-frequency radio waves, a theoretical investigation," *J. Res. Nat. Bureau Stand.*, vol. 64D, p. 153, 1960.

[2]   K. G. Budden, "The influence of the Earth's magnetic field on radio propagation by wave-guide modes," *Proc. Royal Society A*, vol. 265, p. 538, 1962.

[3]   J. R. Wait, "Earth-ionosphere cavity resonances and the propagation of ELF radio waves," *Radio Science*, vol. 69D, p. 1057, 1965.

[4]   J. R. Wait, "Distortion of ELF pulses after propagation through an antipode," *J. Geophys. Res.*, vol. 74, pp. 2982–2986, 1969.

[5]   J. R. Wait, *Electromagnetic Waves in Stratified Media.* New York: Pergamon Press, 1970.

[6]   J. R. Wait, "Reflection of VLF radio waves at a junction in the earth-ionosphere waveguide," *IEEE Trans. Electromagn. Compat.*, vol. 34, p. 4, 1992.

[7]   L. Liebermann, "Extremely low-frequency electromagnetic waves 1. Reception from lightning," *Journal of Applied Physics*, vol. 27, no. 12, pp. 1473 – 1476, 1956.

[8]   E. R. Williams, "The Schumann Resonance – a global tropical thermometer," *Science*, vol. 256, p. 1184, 1992.

[9]   E. P. Velikhov, A. A. Zhamaletdinov, A. N. Shevtsov, A. D. Tokarev, Yu. M. Kononov, L. B. Pesin, G. M. Kadyshevich, M. I. Pertel, and A. V. Veshchev, "Deep electromagnetic studies with the use of powerful ELF radio installations," *Isvestiya, Physics of the Solid Earth*, vol. 34, no. 8, pp. 615-632, 1998.

[10]   Y. B. Bashkuev and V. B. Khaptanov, "Deep radio impedance sounding of the crust using the electromagnetic field of a VLF radio installation," *Izvestiya – Phys. of the Solid Earth*, vol. 37, no. 2, pp. 157-165, 2001.

[11]   J. R. Wait, "Project Sanguine," *Science*, vol. 178, pp. 272-275, 1972.

[12]   S. K. Park, M. J. S. Johnston, Th. R. Madden, F. D. Morgan, and H. F. Morrison, "Electromagnetic precursors to earthquakes in the ULF band: a review of observations and mechanisms," *Rev. Geophys.*, vol. 31, p. 117-132, 1993.

[13]   M. J. S. Johnston, "Review of electric and magnetic fields accompanying seismic and volcanic activity," *Surv. Geophys.*, vol. 18, p. 441-475, 1997.

[14]   A. Taflove and S. C. Hagness, *Computational Electrodynamics: The Finite-Difference Time- Domain Method, 3rd. ed.* Norwood, MA: Artech House, 2005.

[15]   D. F. Morfitt and R. F. Halley, "Comparison of waveguide and wave hop techniques for VLF propagation modeling," *NWC Techniques Publication 4952*, Naval Weapons Center, China Lake, CA, 1970.

[16]   R. A. Pappert and F. A. Ferguson, "VLF/LF mode conversion model calculations for air to air transmissions in the Earth-ionosphere waveguide," Radio Science, vol. 21, no. 551, 1986.

[17]   M. Thevenot, J. P. Berenger, Th., Monediere, F. Jecko, "A FDTD scheme for the computation of VLF-LF Propagation in the Anisotropic Earth-ionosphere Waveguide," Annals of Telecommunications, vol. 54., no. 5-6, pp. 297-310, 1999.

[18]   J. J. Simpson and A. Taflove, "A review of progress in FDTD Maxwell's equations modeling of impulsive sub-ionospheric propagation below 300 kHz," *IEEE Transactions on Antennas and Propagation*, in press.

[19]   J. P. Berenger, "Finite-difference computation of VLF-LF propagation in the Earth-ionosphere waveguide," EUROEM Symposium, Bordeaux, France, June 1994.

[20]   J. P. Berenger, "Reduction of the angular dispersion of the FDTD method in the Earth-ionosphere waveguide," Journal Electromagnetic Waves and Applications, vol. 17, no. 8, pp. 1225-1235, 2002.

[21]   J. P. Berenger, "FDTD computation of VLF-LF propagation in the Earth-ionosphere waveguide," Annals of Telecommunications, vol. 57, no. 11-12, pp. 1059-1090, 2002.

[22]   S. A. Cummer, "Modeling electromagnetic propagation in the Earth-ionosphere waveguide," *IEEE Trans. Antennas Propagation*, vol. 48, no. 9, pp. 1420, 2000.

[23]   W. Hu and S. A. Cummer, "An FDTD model for low and high altitude lightning-generated EM fields," *IEEE Trans. Antennas Propag.*, vol. 54, no. 5, pp. 1513-1522, 2006.

[24]   Maloney and G. S. Smith, "The use of surface impedance concepts in the finite-difference time-domain method," *IEEE Trans. Antennas Propag.*, vol. 40, pp. 38-48, 1992.

[25]   S. Kellali, B. Jecko, and A. Reineix, "Implementation of a surface impedance formalism at oblique in FDTD method," *IEEE Trans. Electromagn. Compat.*, vol. 35, pp. 347-356, 1993.

[26]   C. Yang and B Zhou, "Calculation methods of electromagnetic fields very close to lightning," *IEEE Transactions on Electromagnetic Compatibility*, vol. 46, no. 1, pp. 133-141, 2004.

[27]   V. Cooray, "Horizontal fields generated by return strokes," Radio Sci., vol. 27, pp. 529-537, 1992.

[28]   M. Rubinstein, "An approximate formula for the calculation of the horizontal electric field from lightning at close, intermediate, and long range," *IEEE Trans. Electromagn. Compat.*, vol. 38, pp. 531-535, 1996.

[29]   H. J. Strangeways, "Lightning, Trimpis, and Sprites," *Review Radio Science, 1993-1996*, ed. by R. Ross Stone, Oxford Univ. Press, pp. 741-780, 1996.

[30]   A. M. Poussard and Y. Corcuff, "Numerical simulation of LEP Trimpis observed at Poitiers France, on signals from VLF transmitters," Journal of Atmospheric and Solar-Terrestrial Physics, vol. 62, pp. 207-224, 2000.

[31]   T. Otsuyama and M. Hayakawa, "FDTD simulation and experimental result on VLF scattering by ionospheric perturbations in Earth-ionosphere waveguide," *T. IEE. Japan*, vol. 122-A, no. 1, pp. 59 – 63, 2002.

[32]   M. S. Sarto, "Innovative absorbing-boundary conditions for the efficient FDTD analysis of lightning-interaction problems," *IEEE Trans. Electromagnetic Compatibility*, vol. 43, no. 3, pp. 368, 2001.

[33]   J. P. Berenger, "Long-range propagation of lightning pulses using the FDTD method," IEEE Transactions on Electromagnetic Compatibility, vol. 47, no. 4, pp. 1008 – 1012, 2005.

[34]   T. Otsuyama and M. Hayakawa, "FDTD Analysis of ELF wave propagation for realistic subionospheric waveguide models," IEEJ Trans. FM, vol. 124, no. 12, pp. 1203-1209, 2004.

[35]   M. Hayakawa and T. Otsuyama, "FDTD analysis of ELF wave propagation in inhomogeneous subionospheric waveguide models," ACES Journal, vol. 17, no. 3, pp. 239-244, 2002.

[36]   R. Holland, "THREDS: A finite-difference time-domain EMP code in 3-D spherical coordinates," *IEEE Trans. Nucl. Sci.,* vol. NS-30, no. 6, pp. 4592-4595, 1983.

[37]   A. P. Nickolaenko and M. Hayakawa, "*Resonances in the Earth-Ionosphere Cavity*, Kluwer Academic Publishers, Dordrecht, 2002.

[38]   C. E. R. Bruce and R. H. Golde, "The lightning discharge," J. Inst. Electr. Eng., vol. 88, pp. 487-505, 1941.

[39] A. P. Nickolaenko, M. Hayakawa, I. G. Kudintseva, S. V. Myand, and L. M. Rabinowicz, "ELF sub-ionospheric pulse in time domain," *Geophys. Res. Lett.*, vol. 26, pp. 999-1002, 1999.

[40] A. P. Nickolaenko and M. Hayakawa, "Natural electromagnetic pulses in the ELF range," *Geophys. Res. Lett.*, vol. 25, no. 16, pp. 3101-3106, 1998.

[41] W. O. Schumann, "On the radiation free self-oscillations of a conducting sphere, which is surrounded by an air layer and an ionospheric shell [in German]," *Zeitschrift fuer Naturforschung*, vol. 7a, pp. 149-154, 1952.

[42] C. Polk, "Relation of ELF noise and Schumann resonances to thunderstorm activity," *Planetary Electrodynamics*, Ed. By Coronoti and Hughes, vol. 2, pp. 55-83, Gordon and Breach, New York, 1969.

[43] O. Pechony and C. Price, "Schumann resonance parameters calculated with a partially uniform knee model on Earth, Venus, Mars, and Titan," *Radio Sci.*, vol. 39, no. 5, 2004.

[44] T. Otsuyama, D. Sakuma, and M. Hayakawa, "FDTD analysis of ELF wave propagation and Schumann resonances for a subionospheric waveguide model," *Radio Sci.,* vol. 38, no. 6, 1103, doi: 10.1029/2002RS002752, 2003.

[45] D. D. Sentman, "Schumann resonances," in *Handbook of Atmospheric Electrodynamics*, Ed. by H. Volland, vol. 1, pp. 267-310, CRC Press, 1995.

[46] A. Soriano, E. A. Navarro, D. L. Paul, J. A. Porti, J. A. Morente, and I. J. Craddock, "Finite-difference time domain simulation of the Earth-ionosphere resonant cavity: Schumann resonances," *IEEE Trans. Antennas and Propagation*, vol. 53, no. 4, pp. 1535-1541, April 2005.

[47] J. Morente, J. Molina-Cuberos, J. Porti, B. Besser, A. Salinas, K. Schwingenschuch, and H. Litchengger, "A numerical simulation of Earth's electromagnetic cavity with the transmission line matrix method: Schumann resonances," *J. Geophys. Res.*, vol. 108, no. A5, 2003.

[48] K. Schlegel and M. Fuellekrug, "Schumann resonance parameter changes during high-energy particle precipitation," *J. Geophys. Res.*, vol. 104, no. A5, pp. 10111-10118, 1999.

[49] D. D. Sentman, "Approximate Schumann resonance parameters for two-scale height ionosphere," *J. Atmospheric Terrestrial Phys.*, vol. 52, no. 1, pp. 35-46, 1990.

[50] H. Yang, and V. P. Pasko, "Three-dimensional finite difference time domain modeling of the Earth-ionosphere cavity resonances," *Geophys. Res. Lett.*, *32*, L03114, doi:10.1029/2004GL021343, 2005.

[51]   D. D. Sentman, "Schumann resonance effects of electrical conductivity perturbations in an exponential atmospheric/ionospheric profile," J. Amtos. Terr. Phys., vol. 45, pp. 55, 1983.

[52]   C. Greifinger and P. Greifinger, "Approximate method for determining ELF eigenvalues in the Earth-ionosphere cavity," Radio Sci., vol. 13, p. 831, 1978.

[53]   D. D. Sentman, "Schumann resonance effects of electrical conductivity perturbations in an exponential atmospheric/iononspheric profile," *J. Atmos. Terr. Phys.*, vol. 45, no. 1, pp., 55-65, 1983.

[54]   V. C. Mushtak and E. Williams, "ELF propagation parameters for uniform models of the Earth-ionosphere waveguide," J. Atmos. Sol. Terr. Phys., vol. 64, 1989.

[55]   M. Ishaq and D. L. Jones, "Method of obtaining radiowave propagation parameters for the Earth-ionosphere duct at ELF," *Electron. Lett.*, vol. 13, p. 254, 1977.

[56]   V. C. Roldugin, Y. P. Maltsev, G. A. Petrova, and A. N. Vasiljev, "Decrease of the first Schumann resonance frequency during solar proton events," *J. Geophys. Res.*, vol. 106, p. 18,555, 2001.

[57]   V. C. Roldugin, Y. P. Maltsev, A. N. Vasiljev, A. V. Shvets, and A. P. Nikolaenko, "Changes of Schumann resonance parameters during the solar proton event of 14 July 2000," *J. Geophys. Res.*, vol. 108, no. A3, pp. 1103, doi:10.1029/2002JA009495, 2003.

[58]   V. C. Roldugin, Y. P. Maltsev, A. N. Vasiljev, A. Y. Schokotov, and G. G. Belyajev, "Schuamnn resonance frequency incrase during solar X-ray bursts," *J. Geophys. Res.*, vol. 109, no. A01216, doi:10.1029/2003JA010019, 2004.

[59]   H. Yang and V. Pasko, "3-D FDTD modeling of the variations of the Schumann resonance parameters in the Earth-ionosphere cavity," *Proc. USNC/URSI National Radio Science Meting*, p. 723, Albuquerque, NM, July 2006.

[60]   D. Bilitza, "IRI 2000," *Radio Science*, vol. 36, no. 2, p. 261-276, 2001.

[61]   Price and Melnikov, "Diurnal, seasonal, and inter-annual variations of the Schumann resonance parameters," *Journal Atmospheric Solar-Terrestrial Physics*, vo. 66, no. 13- 14, pp. 1179-1185, 2004.

[62]   H. Yang, V. P. Pasko, Y. Yair, "Three-dimensional finite difference time domain modeling of the Schumann resonance parameters on Titan, Venus, and Mars," *Radio Science*, vol. 41, RS2S03, doi:10.1029/2005RS003431, 2006.

[63]   K. S. Yee, "Numerical solution of initial boundary value problems involving Maxwell's equations in isotropic media," *IEEE Trans. Ant. Prop.*, vol. AP-14, pp. 302-307, 1966.

[64]   A. Taflove, "Application of the finite-difference time-domain method to sinusoidal steady-state electromagnetic penetration problems," *IEEE Trans. On Electromagnetic Compatibility*, vol. 22, pp. 191-202, 1980.

[65]   J. J. Simpson and A. Taflove, "Two-dimensional FDTD model of antipodal ELF propagation and Schumann resonance of the Earth," *IEEE Antennas and Wireless Propagation Lett.*, vol. 1, no. 2, pp. 53-56, 2002.

[66]   A. Taflove and J. J. Simpson, "Introduction to Maxwell's equations and the Yee algorithm," in *Computational Electrodynamics: The Finite-Difference Time-Domain Method, 3rd ed.*, A. Taflove and S. C. Hagness, Norwood, MA: Artech House, 2005.

[67]   J. J. Simpson and A. Taflove, "Three-dimensional FDTD modeling of impulsive ELF propagation about the Earth-sphere," *IEEE Trans. Antennas and Propagation*, vol. 52, pp. 443–451, Feb. 2004.

[68]   R. A. Sadourny, Arakawa, and Y. Mintz, "Integration of the nondivergent barotropic vorticity equation with an icosahedral-hexagonal grid for the sphere," *Mon. Wea. Rev.*, vol. 96, pp. 351-356, 1968.

[69]   D. A. Randall, T. D. Ringler, and R. P. Heikes, "Climate modeling with spherical geodesic grids," *Computing in Science and Engineering*, vol. 4, no. 5, pp. 32 – 41, Sept./Oct. 2002.

[70]   J. J. Simpson and A. Taflove, "Efficient modeling of impulsive ELF antipodal propagation about the Earth sphere using an optimized two-dimensional geodesic FDTD grid," *IEEE Antennas and Wireless Propagation Lett.*, vol. 3, no. 11, pp. 215-218, 2004.

[71]   R. P. Heikes, "A Comparison of Vertical Coordinate Systems for Numerical Modeling of the General Circulation of the Atmosphere," *Ph. D. Dissertation*, Colo. State Univ., Fort Collins, CO, 2001.

[72]   M. Brewer, L. Freitag-Diachin, P. Knupp, T. Leurent, and D. Melander, "The Mesquite Mesh Quality Improvement Toolkit," *Proc. of the 12th Intl. Meshing Roundtable*, pp. 239-250, Santa Fe, NM, 2003.

[73]   J. J. Simpson, R. P. Heikes, and A. Taflove, "FDTD modeling of a novel ELF radar for major oil deposits using a three-dimensional geodesic grid of the Earth-ionosphere waveguide," *IEEE Transactions on Antennas and Propagation*, vol. 54, no. 6, pp. 1734-1741, June 2006.

[74]   NOAA-NGDC "Global Relief CD-ROM"

[75]   J. Hermance, "Electrical conductivity of the crust and mantle," *Global Earth Physics: A Handbook of Physical Constants*, AGU, 1995.

[76]   P. Bannister, "The determination of representative ionospheric conductivity parameters for ELF propagation in the Earth-ionosphere waveguide," *Radio Sci.*, vol. 20, no. 4, pp. 977 - 984, 1985.

[77]   P. Bannister, "ELF propagation update*," IEEE Journal of Oceanic Eng.*, vol. 0E-9, no. 3 pp. 179 - 188, 1984.

[78]   J. R. Wait, "On the theory of the slow tail portion of atmospheric wave forms", *J. Geophys. Res.,* 65 (7), pp. 1939-1946, 1960.

[79]   J. J. Simpson and A. Taflove, "Electrokinetic Effect of the Loma Prieta Earthquake calculated by an entire-Earth FDTD solution of Maxwell's equations," *Geophysical Research Lett.,* vol. 32, L09302, doi:10.1029/2005GL022601.

[80]   O. A. Molchanov, M. Hayakawa, and V. A. Rafalsky, "Penetration characteristics of electromagnetic emissions from an underground seismic source into the atmosphere, ionosphere, and magnetosphere," *J. Geophysical Res. – Space Phys.*, vol. 100, no. A2, pp. 1691 – 1712, Feb. 1995.

[81]   A. V. Kulchitsky, Y. Ando, and M. Hayakawa, "Numerical analysis on the propagation of ULF/ELF signals in the lithosphere with highly conductive layers," *Phys. and Chem. of the Earth*, vol. 29, pp. 495-500, 2004.

[82]   A. C. Fraser-Smith, A. Bernardi, P. R. McGill, M. E. Ladd, R. A. Helliwell, and O. G. Villard Jr., "Low-frequency magnetic field measurements near the epicenter of the Ms 7.1 Loma Prieta earthquake," *Geophys. Res. Lett.*, vol. 17, p. 1465-1468, 1990.

[83]   M. A. Fenoglio, M. J. S. Johnston, J. D. Byerlee, "Magnetic and electric fields associated with changes in high pore pressure in fault zones: application to the Loma Prieta ULF emissions," *J. Geophs. Res.*, vol. 100, p. 12951-12958, 1995.

[84]   O. Majaeva, Y. Fujinawa, and M. E. Zhitomirsky, "Modeling of non-stationary electrokinetic effect in a conductive crust," *J. Geomag. Geoelectr.*, vol. 49, p. 1317-1326, 1997.

[85]   MATLAB: The Language of Technical Computing, Version 6.5.0.180913a Release 13, June 18, 2002.

[86]   A. C. Fraser-Smith, personal communication to J. J. Simpson.

[87]   A. Takeuchi and H. Nagahama, "Electric dipoles perpendicular to a a stick-slip plane," *Physics of the Earth and Planetary Interiors*, vol. 155, pp. 208-218, 2006.

[88]   A. Takeuchi, B. W.S. Lau, F. T. Freund, "Current and surface potential induced by stress-activated positive holes in igneous rocks," *Physics and Chemistry of the Earth*, vol. 31, pp. 240-247, 2006.

[89]   F. T. Freund, A. Takeuchi, and B. W.S. Lau, "Electric currents streaming out of stressed igneous rocks—A step towards understanding pre-earthquake low frequency EM emissions," *Physics and Chemistry of the Earth*, vol. 31, pp. 389-396, 2006.

[90]   J. J. Simpson and A. Taflove, "A Novel ELF Radar for Major Oil Deposits," *IEEE Geoscience and Remote Sensing Lett.*, vol. 3, no. 1, pp. 36-39, 2006.

[91]   M. A. Meju, "Geoelectromagnetic exploration for natural resources: Models, case studies and challenges," Surveys in Geophysics, vol. 23, no. 2-3, pp. 133-205, 2002.

[92]   U. S. Congress, Office of Technology Assessment, *Oil Production in the Arctic National Wildlife Refuge: The Technology and the Alaskan Oil Context*, OTA-E-394, Washington, DC: U.S. Government Printing Office, Feb. 1989.

[93]   J. R. Wait, "Project Sanguine," *Science*, vol. 178, pp. 272-275, 1972.

[94]   J. B. Lee, D. L. Dart, R. J. Turner, M. A., Downey, A. Maddever, G. Panjkovic, C. P. Foley, K. E. Leslie, R. Binks, C. Lewis, W. Murray, "Airborne TEM surveying with a SQUID magnetometer sensor," *Geophysics*, vol. 67, no. 2, pp. 468-477, Mar.-Apr. 2002.

[95]   J. J. Simpson and A. Taflove, "ELF radar system proposed for localized D-region ionospheric anomalies," *IEEE Geoscience and Remote Sensing Letters*, vol. 3, no. 4, pp. 500-503, Oct. 2006.

[96]   S. A. Cummer, U. S. Inan, and T. F. Bell, "Ionospheric D region remote sensing using VLF radio atmospherics," *Radio Sci.*, 33, 1781-1792, 1998.

[97]   C. F. Sechrist Jr., "Comparisons of techniques for measurement of D-region electron densities," *Radio Science*, vol. 9, p. 137, 1974.

[98]   O. A. Molchanov, M. Hayakawa, T. Oudah, E. Kawai, "Precursory effects in the subionospheric VLF signals for the Kobe earthquake," *Phys. Earth Planetary Interiors*, vol. 105 (3-4), pp. 239-248, 1998.

[99]   C. J. Rodger, M. A. Clilverd, and N. R. Thomson, Modeling of subionospheric VLF signal perturbations associated with earthquakes, *Radio Sci.*, vol. 34, no 5, pp. 1177-1185, 1999.

[100] S. Pulinets and K. Boyarchuk, *Ionospheric Precursors of Earthquakes*, 315 pp., Berlin, Germany: Springer, 2004.

[101] V. P. Kim, S. A. Pulinets, and V. V. Hegai, Theoretical model of possible disturbances in the nighttime mid-latitude ionospheric D region over an area of strong-earthquake preparation, *Radiophysics and Quantum Electronics,* vol. 45, no. 4, pp. 262 – 268, 2002.

[102] J. J. Simpson and A. Taflove, "Full-vector 3-D FDTD model of radiated impulsive lightning waveforms influenced by the ionospheric plasma magnetized by the geomagnetic field," to be submitted to *IEEE Transactions on Antennas and Propagation*.

[103] J. H. Lee and D. K. Kalluri, "Three-dimensional FDTD simulation of electromagnetic wave transformation in a dynamic inhomogeneous magnetized plasma," *IEEE Trans. Antennas and Propagation*, vol. 47, no. 7, pp. 1146-1151, 1999.

[104] J. E. Bickel, J. A. Ferguson, and G. V. Stanley, "Experimental observation of magnetic field effects on VLF propagation at night," Radio Sci., vol. 5, pp. 19-26, 1970.

[105] N. R. Thomson, "Experimental daytime VLF ionospheric parameters," J. Atmos. Terr. Phys., vol. 5, pp. 173-184, 1993.

[106] J. R. Wait and K. P. Spies, "Characteristics of the Earth-ionosphere waveguide for VLF radio waves," Tech. Note 300, *National Bureau of Standards*, Boulder, CO, 1964.

[107] A. S. Dennis and E. T. Pierce, "The return stroke of the lightning flash to Earth as a source of VLF atmospherics," *Radio Sci.*, vol. 68D, p. 777, 1964.

[108] L. Sevgi, F. Akleman, and L. B. Felsen, "Groundwave propagation modeling: Problem-matched analytical formulations and direct numerical techniques," *IEEE Antennas and Propagation Magazine*, vol. 44, no. 1, pp. 55 – 75, 2002.

[109] URL: http://www.ngdc.noaa.gov/seg/geomag/models.shtml

[110] URL: http://www.nrl.navy.mil/content.php?P=04REVIEW105

[111] URL: http://www.ngdc.noaa.gov/stp/IONO/models.html

[112] URL: http://modelweb.gsfc.nasa.gov/ionos/ionos_index.html

Appendix A: Additional Doctoral Research

Substrate Integrated Waveguides for Ultrahigh-Speed Digital Interconnects

Abstract— As clock rates continue to rise, problems with signal integrity, cross-coupling, and radiation may render impractical the baseband metallic interconnects presently used in computers. In fact, because clock rates approaching microwave frequencies of 20 GHz are projected by 2010, attention is being drawn toward alternative technologies that have relatively favorable signal transmission characteristics. While optical interconnects could easily provide the necessary bandwidth, there are major difficulties in integrating the required GaAs laser sources into existing silicon chip technology. An alternate potential means to address this problem is to use bandpass wireless interconnects operating at millimeter-wave center frequencies. The text below reports an experimental and computational study of substrate integrated waveguides (SIWs) optimized for use as ultrahigh-speed bandpass waveguiding digital interconnects. The novelty of the present work resides in the successful design, fabrication, and testing of low-loss SIWs that achieve 100% relative bandwidths via optimal excitation of the dominant TE_{10} mode and avoidance of the excitation of the TE_{20} mode. Further, it is found that these optimal structures maintain their 100% relative bandwidth while transmitting around 45° and 90° bends, and achieve measured crosstalk of better than –30 dB over the entire passband. SIWs operating at center frequencies of 50 GHz are considered here, accommodating in principle data rates of greater than 50 Gb/sec. Because existing circuit-board technology permits dimensional reductions of the SIWs by yet another factor of 4:1 relative to

the ones discussed here, bandpass operation at center frequencies approaching 200 GHz with data rates of 200 Gb/sec are feasible. These data rates meet or exceed those expected eventually for proposed silicon photonic technologies, without requiring the integration of GaAs laser sources into existing silicon chip technology.

I. INTRODUCTION

Since the advent of digital computers in the 1940s, baseband metallic stripline circuit-board interconnects have been employed for transmitting data between processors. Until recently, such interconnects provided adequate bandwidths even while data rates increased according to Moore's Law. However, as clock speeds continue to rise in the microwave frequency range above 3 GHz, problems with signal integrity, cross-coupling, and radiation that are intrinsic to stripline interconnects are becoming increasingly difficult to overcome. This has led to significant research in silicon photonics [1], which would replace the metallic striplines with optical fibers. However, realization of the complete suite of required optoelectronic technologies will involve a complex set of tasks to implement a fundamental paradigm shift in chip and interconnect design. This will necessarily involve years of work.

This Appendix reports the computational and experimental studies which advance an attractive alternate possibility that relies upon evolutionary, rather than revolutionary, developments in interconnect technology. Specifically, the successful design, construction, and testing of ultrahigh-speed, low-loss, low-crosstalk, bandpass waveguiding interconnects implemented in conventional circuit boards is reported. While the measurements to date have been limited to bandwidths suitable for 50 Gb/s data transmission rates, it is clear that these interconnects can be scaled to permit operation at data rates of 200 Gb/sec with no improvements in circuit board manufacturing techniques. These data rates meet or exceed those expected eventually for proposed silicon photonic technologies.

The optimized bandpass waveguiding interconnects considered are based upon the substrate integrated waveguide (SIW) configuration [2 - 8]. Here, a waveguide mode is bounded vertically by two copper planes of a double-sided circuit board, and is bounded transversely by

single rows of cylindrical copper pins (vias) electrically bonded to the opposing ground planes. Input and output coupling is achieved using coaxial lines terminated with short vertical probes extending completely across the gap between the upper and lower ground planes. Each probe is electrically isolated from the ground planes by etching oversized holes through the ground planes at the probe locations.

In the context of bandpass wireless interconnects, the SIWs considered here are optimized for narrow transverse dimensions, low loss, low crosstalk, and maximum bandwidth with no multimoding [9]. The novelty of this work resides in the successful design, fabrication, and testing of low-loss SIWs that achieve 100% relative bandwidths via optimal excitation of the dominant TE_{10} mode and avoidance of the excitation of the TE_{20} mode. Furthermore, these optimal structures maintain their 100% relative bandwidth while transmitting around 45° and 90° bends, and achieve measured crosstalk of better than –30 dB over the entire passband. These results indicate that the optimized SIWs should have excellent utility when implemented in modern digital circuit boards having typically dense layouts [9].

The remainder of this Appendix is organized into six Sections. Section II provides background information relevant to the present work. Section III presents the computational and experimental study of a single, straight electromagnetic bandgap (EBG) waveguide [10, 11] embedded in standard double-sided circuit board comprised of FR4 dielectric and operating at a center frequency of 50 GHz. (EBG waveguides are similar to SIWs with the exception that each waveguide was bounded in the plane of propagation by double rows of vias.) This study forms the basis of the SIW investigations reported in later sections, and is included for purposes of comparison with these results and to demonstrate the capabilities and accuracy of the finite-difference time-domain (FDTD) [12] models. Section IV presents the computational and

experimental results for the more compact, optimized, single, straight SIW implemented in a double-sided circuit board comprised of Rogers RT/duroid® 5880 dielectric and operating at a 50 GHz center frequency. This section also illustrates FDTD modeling results for an SIW structure scaled to a center frequency of 130 GHz. Section V then presents the computational and experimental results for crosstalk between adjacent SIWs, and Section VI reports FDTD modeling results for optimized 45° and 90° SIW bends that are capable of maintaining the ultrawide relative bandwidth of ~100%. Section VII reports on second-generation SIW designs involving half-width folded geometry. Finally, Section VIII concludes and presents details of future work in this area.

II. BACKGROUND AND SUMMARY OF INITIAL WORK

Since the birth of the personal computer, Moore's Law [13] has had great success in predicting the performance growth of microprocessors and PC systems. Using such metrics as processor frequency and millions-of-instruction per second (MIPs) the trends show exponential growth, with a doubling in performance roughly every eighteen to twenty four months [14]. Fig. 1 represents the assessment by Intel Corporation of how such exponential performance growth also applies to rates of inter-chip data transmission. Contemporary host interface designs employ an eight byte wide data bus operating at 1.066 Gb/s with bi-directional, single ended signal to provide a peak bandwidth of ~8.5 GB/s. Extrapolating the trend in the figure, a bandwidth demand of more than 100 GB/s within ten years is predicted, which requires increasing the width of the interface, increasing the per signal data rate, or a combination of the two. In the cost-driven environment of the PC market place, typical desktop personal computers use low cost 4-

layer, FR4-based motherboards. Increasing the width of the host interface drives higher cost by requiring additional layers in the motherboard, making wider interfaces unattractive.
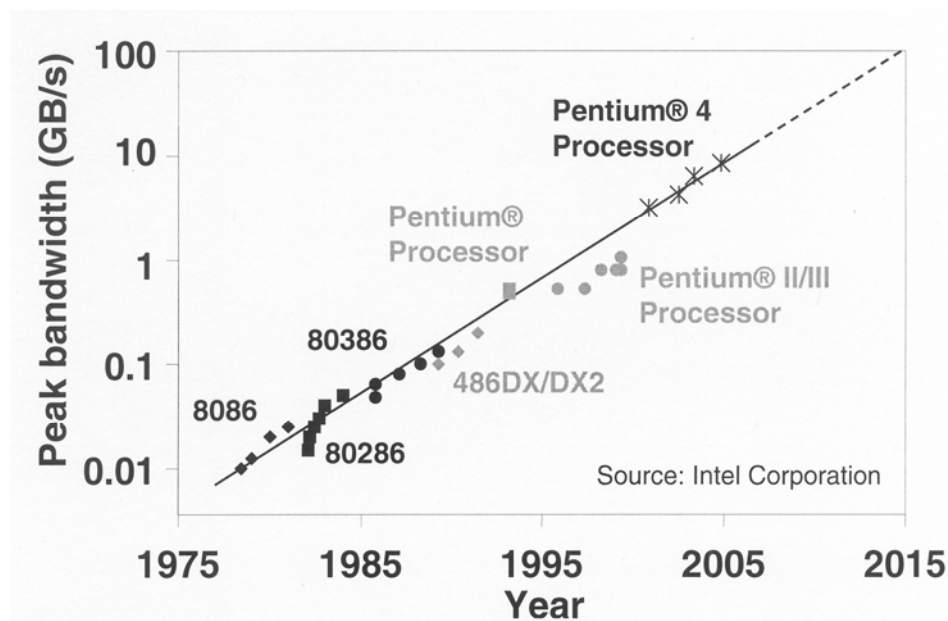
Figure 1   Host interface bandwidth demand trend for Intel microprocessors. Peak bandwidth demand has grown at a rate of 1.66x every two years since 1978.

Addressing the demand via scaling to higher data rates presents difficulties as well. Multi-Gb/s signaling solutions typically employ differential, uni-directional signaling, which limits the data bus width to two bytes in order to fit within a four-layer motherboard.   Under these conditions, the data rate demand becomes 50 Gb/s per differential pair, a requirement that exceeds the expected capability of PCB-based transmission line signaling by a factor of 2 [15].

Anticipating this difficulty in meeting the projected bandwidth demand of future microprocessors, an investigation was conducted of alternative waveguiding structures that have the promise of mitigating or even avoiding the problems associated with conventional metallic interconnects, and yet can be implemented using standard circuit board fabrication techniques.

Specifically, as reported in [16], an initial proof-of-concept work was performed, implementing EBG waveguides having a 10 GHz center frequency in standard printed circuit boards. This resulted in a measured passband extending from 6 to 14.1 GHz with an insertion loss over the passband ranging from 3.6 – 7.3 dB.

Success in this initial proof-of-concept led to an investigation of the scalability of the EBG structure, specifically to a 50 GHz center frequency as reported in [17]. Motivation for this was twofold. First, the dimensions of EBG structures scale inversely with frequency, reducing the transverse width of the EBG waveguide structure. Second, the higher center frequency is required in order to achieve higher data transmission rates. Section III below expands upon the work reported in [16, 17] by implementing a 14-pole Debye model for the FR4 dielectric dispersion characteristic at a 50 GHz center frequency.

III. SINGLE, STRAIGHT EBG INTERCONNECT WITH
80% RELATIVE BANDWIDTH

This section presents the computational and experimental study of a single, straight EBG waveguide embedded in standard double-sided circuit board comprised of FR4 dielectric and operating at a center frequency of 50 GHz. This study forms the basis of the SIW investigations to be presented in later sections, and is included for purposes of comparison with these results and to demonstrate the capabilities and accuracy of our FDTD models.

First, results are shown for an EBG waveguide analogous to those described in [16, 17]. As in [16, 17], the EBG waveguide is formed by removing two rows of a square lattice of pins having initially six rows. The same pin radius to center-to-center spacing ratio (r/a = 18%) and pin radius to waveguide width ratio (r/w = 6%) is used. Here, however, the EBG structure is

scaled to a center frequency of 50 GHz and uses FR4 as the dielectric material ($\varepsilon_r \sim 3.9$ and tan δ

~ 0.017 at 50 GHz).

For the FDTD simulations, a high-resolution three-dimensional (3-D) grid having a space-cell size of 4.4 x 4.4 x 76 μm and a stable time-step near the Courant limit is employed. A 14-pole Debye model is implemented to accurately simulate the dispersive characteristics of the FR4 dielectric. In addition, a frequency-dependent skin-effect model is implemented for all copper surfaces [18]. The waveguide spans about 8.6 cm between the input and output probes, has height $h = 0.76$ mm between the upper and lower ground planes, and distance $w = 2.8$ mm (center-to-center) between the rows of vias immediately bounding the waveguide. Each via has a radius $r = 0.17$ mm and is separated from its neighboring via with a center-to-center spacing $a = 0.93$ mm. Fig. 2 is a photo of the corresponding test structure used in the measurements.
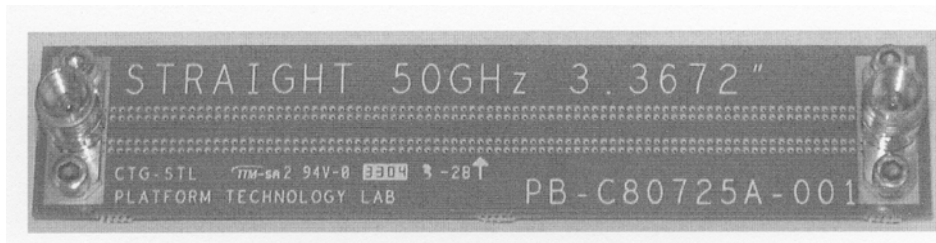
Figure 2   Photo of an 8.6-cm-long EBG interconnect scaled to a center frequency of 50 GHz. This test structure is comprised of FR4 dielectric material ($\varepsilon_r = 3.9$ and tan $\delta = 0.017$) and has $r = 0.93$ mm, $a = 0.17$ mm, $w = 2.8$ mm, and $h = 0.76$ mm.

Fig. 3 compares the measured and FDTD modeling results for the insertion loss (S_{21}) of the 8.6-cm-long structure of Fig. 2.   A standard Agilent microwave network analyzer (with capabilities to 67 GHz) having 50-ohm nominal source and load impedances was used in these

measurements. From Fig. 3, we first note that there exists a sharp transition from a deep stopband (below -80 dB) to a passband at approximately 30 GHz. This passband extends to approximately 70 GHz, above which the EBG structure can no longer effectively confine the propagating signal (yielding an upper stopband limit) [11]. This EBG waveguide therefore provides an approximately 80% fractional bandwidth.
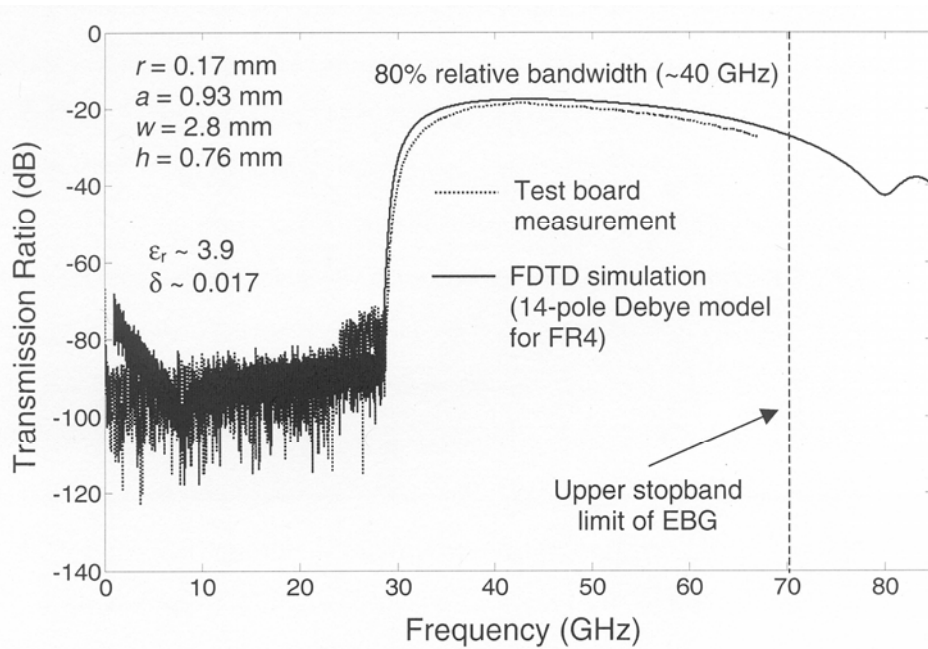
Figure 3 Comparison between the measured and FDTD-calculated S_{21} characteristics over the 8.6-cm-long EBG interconnect of Fig. 2.

Fig. 3 shows a very good agreement between the measured and FDTD-calculated S_{21} characteristics over a wide dynamic range. This agreement extends all the way to the upper stopband limit of the EBG structure despite the complicated dispersive properties of the FR4 dielectric. At midband (50 GHz), S_{21} for the 8.6-cm-long EBG waveguide is –20.4 dB. Comparison of this result with that of an identical, but longer (12.7 cm) waveguide indicates that

each coaxial transition introduces an input/output coupling loss of only about 0.6 dB. Combined with the flatness of the S_{21} characteristic in the passband, it is apparent that the simple probes used to excite and receive the waveguide mode provide excellent broadband matching. Since the remaining loss is caused by propagation attenuation in the FR4 dielectric, it is clear that migration of this technology to the millimeter-wave regime will require the use of dielectric materials having low loss up to several hundreds of GHz. Candidate materials for this application include aerogels [19]. For intermediate frequencies, alternative materials such as Rogers RT/duroid® 5880 dielectric may be used, as shown below.

IV. SINGLE, STRAIGHT SIW INTERCONNECT WITH

100% RELATIVE BANDWIDTH

This section presents the computational and experimental results for an optimized, single, straight SIW implemented in a double-sided circuit board comprised of glass reinforced PTFE dielectric, Rogers RT/duroid® 5880, and operating at a 50 GHz center frequency. For this structure as well as the remaining structures considered in this Appendix, comprehensive data for the frequency dependence of the Rogers RT/duroid® 5880 dielectric are not available at this time. As a result, a frequency-independent model is used when simulating the Rogers RT/duroid® 5880 dielectric (ε_r = 2.2, tan δ = 0.0009). This necessarily reduces the agreement between the measured and FDTD results, but not to the point where the computational modeling loses utility.

The EBG interconnect designs of the previous Section and [16, 17] employ r/a = 18% and r/w = 6%, and required at least two rows of pins bounding the waveguide to prevent significant leakage [16]. Since an interconnect design having the smallest possible dimensions transverse to

the direction of propagation is desired, waveguides bounded by a single row of pins (i.e. SIWs) will now be investigated. This involves numerous simulations for two classes of parametric studies: (a) varying a while maintaining constant r and w; and (b) varying r while maintaining constant a and w. From parametric study (a), relative to the EBG waveguides of Section III and [16, 17], it is found that in order to maintain a constant cutoff frequency of the fundamental mode, w must be increased by up to 8% as a decreases towards a value of $2r$ (forming a corrugated waveguide with adjacent pins touching and having zero leakage). Taking this into account, the widest bandwidth is obtained for $a = 2r$. From parametric study (b), it is found that the optimal r/w ratio remains 6%. For larger or smaller values of r/w, the bandwidth is reduced.
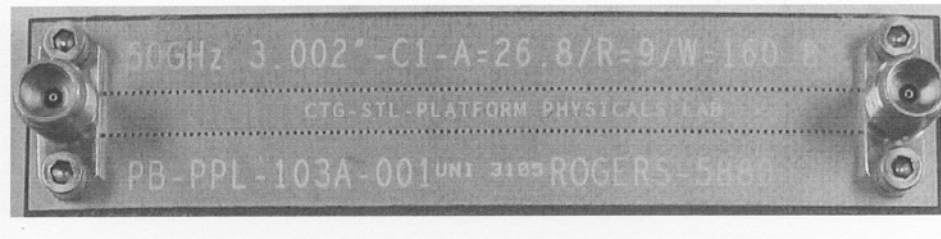
Figure 4   Photo of a 7.6-cm-long SIW interconnect scaled to a center frequency of 50 GHz. This test structure is comprised of Rogers RT/duroid® 5880 dielectric material ($\varepsilon_r = 2.2$ and $\tan \delta = 0.0009$) and has $r = 0.24$ mm, $a = 0.68$ mm, $w = 4.1$ mm, and $h = 0.76$ mm. Further, it is 35% smaller in the transverse direction than the EBG waveguide of Fig. 2.

Considering the above findings, the design criterion for an optimum SIW interconnect is: $r/w = 6\%$ and $a = 2r$. However, having adjacent via pins in contact poses a difficult fabrication problem. Consequently, in the results presented here, a small gap of $0.83r$ (0.20 mm) is introduced between adjacent vias. At present, this is approximately the minimum feasible gap

size in standard circuit boards. Fig. 4 is a photo of an optimized 7.6-cm-long SIW interconnect designed to these specifications. This interconnect is comprised of low-loss Rogers RT/duroid® 5880 dielectric for the case of $r = 0.24$ mm, $a = 0.68$ mm, $w = 4.1$ mm, and h = 0.76 mm. It is 35% narrower in the transverse direction than our previously reported EBG interconnects of Section III and [16, 17].
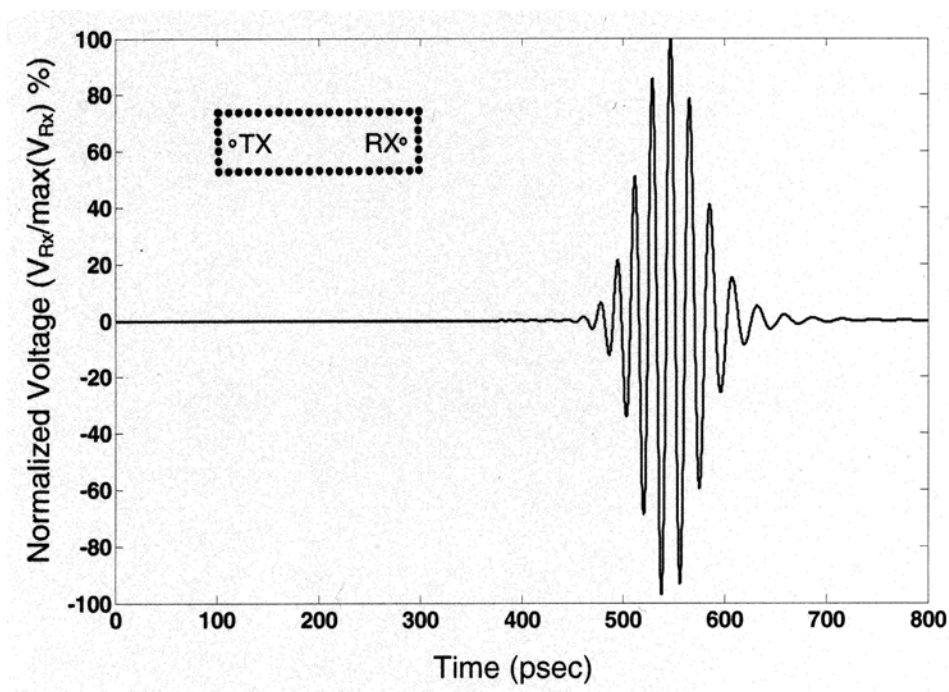
Figure 5   The FDTD-calculated normalized time-waveform of the received voltage of the interconnect of Fig. 4 for an assumed 134-psec (full-width at half-maximum) transmitted 50-GHz carrier pulse having a Gaussian envelope.

Fig. 5 shows the FDTD-calculated normalized time-waveform of the received voltage of the interconnect of Fig. 4 for an assumed 134-psec (full-width at half-maximum) transmitted 50-GHz carrier pulse having a Gaussian envelope. For this case, the spectrum of the transmitted pulse is centered at 50 GHz and falls to –22 dB at 27 GHz and 81 GHz, respectively the lower

and upper limits of the SIW passband. Fig. 5 shows that the received pulse exhibits little ringing. In fact, upon overlaying the received and transmitted pulses, there is an essential coincidence of the zero-crossings and very little distortion.
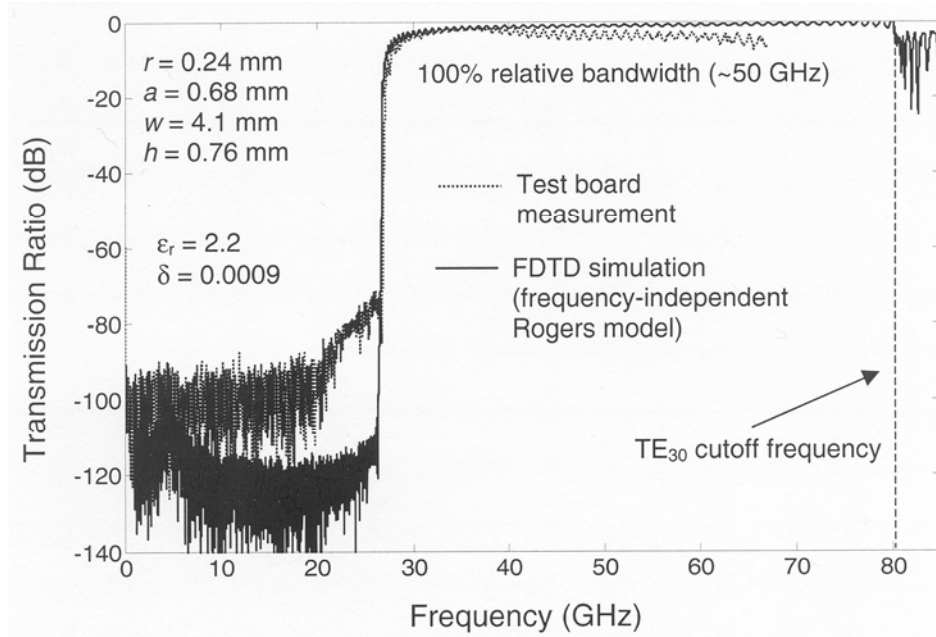
Figure 6   Comparison between the measured and FDTD-calculated S_{21} characteristics over the optimized 7.6-cm-long SIW interconnect of Fig. 4.

Fig. 6 compares the associated spectrum of the measured and FDTD-calculated S_{21} characteristics for the SIW structure of Fig. 4. From Fig. 6 shows a deep stopband of better than –80 dB below approximately 27 GHz. Above 27 GHz, the S_{21} characteristic transitions to an ultrawide passband extending to 81 GHz, providing an approximately 100% bandwidth. The 27-GHz cutoff frequency agrees with that calculated using the equation provided by [4] for the effective width of an equivalent rectangular waveguide:

$$w_{\mathrm{eff}} = w - 1.08 \ [(2r)^2/a] + 0.1(2r)^2/w$$

As explained previously, the deviation of the measured and FDTD results within the passband is caused by the assumption of frequency-independent dielectric properties of the Rogers RT/duroid® 5880 dielectric. The measured midband transmission loss is only 3.6 dB, a value which includes the coupling losses of the two probes and the wave propagation attenuation. Comparison of this result with those of identical, but longer (12.7 and 25.4 cm) waveguides yields 0.31 dB/cm propagation loss in the Rogers RT/duroid® 5880 dielectric at midband.

The ~100% relative bandwidth seen in Fig. 6 is larger than the ~80% bandwidths obtained in Section III and [16, 17] for two reasons: (1) the passband is not bounded by any stopband limit imposed by the bounding vias [16], and hence the passband can extend fully to the cutoff frequency of the second even transverse electric (TE) mode; and (2) for the case studied here, the transmitting and receiving probes are centered transversely in the waveguide and longitudinally positioned at what appears to be an optimum location of one-quarter wavelength at midband (~54 GHz) from the ends of the waveguide (whereas in Section III and [16, 17] the probes were positioned in-line with the 2nd column of vias). Both of these optimizations are discussed in more detail below.

Now reason (1) for the improved bandwidth of the SIW structures relative to the previous EBG results will be discussed. From [3], it is known that the TE-mode cutoff frequencies of the SIW are the same as for those of a flat-wall rectangular waveguide having the same effective waveguide width, w_{eff}. (The SIW considered here has $w_{eff} = 3.74$ mm.) Note that TM modes are not supported by the SIW structure [3], and therefore need not be considered. Fig. 7 illustrates the results of an investigation to see if odd TE modes can be excited in the SIW, especially the first odd TE mode which would arise at approximately midband and potentially disrupt the

desired fundamental-mode operation of the interconnect. This figure compares the measured S_{21} characteristics for two 7.6-cm-long SIW interconnects of the type shown in Fig. 4. The first characteristic is for the case of both transmitting and receiving probes at the optimum transverse and longitudinal locations, while the second characteristic is for the case of both probes shifted transversely by $0.25w$ towards the edge of the waveguide. Fig. 7 shows that the odd modes are negligible when the probes are centered transversely, whereas the single-mode passband is halved for the off-center case. Further results not shown here reveal that the much smaller transverse deviations of the probes from the center line caused by typical manufacturing tolerances generate an acceptably low level of odd modes. Hence, it appears feasible to manufacture SIW interconnects having passbands that extend from the cutoff frequency of the fundamental TE mode to the cutoff frequency of the second even TE mode, yielding ~100% relative bandwidth.

Now reason (2) for the improved bandwidth of the SIW structures discussed here relative to the previous EBG results will be discussed: the optimized longitudinal probe placement. Fig. 8 illustrates the effect of moving the transmitting and receiving probes longitudinally relative to the optimum position by $1.5r$. Compared to the optimum case, we find that the S_{21} characteristic at the lower end of the passband is degraded for probes shifted closer to the waveguide ends (Fig. 8(a)). Furthermore, destructive interference degrades the S_{21} characteristic at the upper end of the passband for probes shifted away from the waveguide ends (Fig. 8(b)).

Our final single, straight SIW structure under study is one scaled to a center frequency of 130 GHz. This example serves to illustrate the scalability of the SIW technology to center frequencies well above 100 GHz (reaching as high as 200 GHz with no required improvements in circuit board manufacturing techniques). The SIW structure of interest spans 0.76 mm

between the upper and lower ground planes and has $r = 0.10$ mm, and $a = 0.41$ mm, $w = 1.6$ mm.

Fig. 9 shows the FDTD-calculated S_{21} characteristic of this device, assuming a frequency-independent model for the Rogers RT/duroid® 5880 dielectric. Here, we see that an ~100% relative-bandwidth passband exists between 65 and 195 GHz, which is suitable for data rates well exceeding 100 Gb/sec. In ongoing work, this structure is being fabricated and tested in the laboratory.
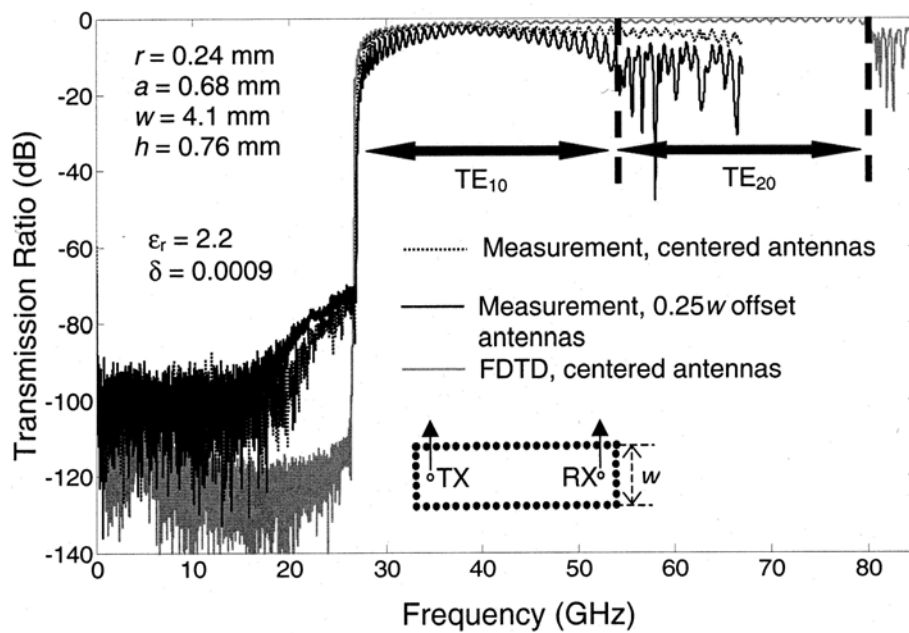
Figure 7 Comparison of the measured S_{21} characteristics for 7.6-cm-long SIW interconnects of the type shown in Fig. 4, for the case of both transmitting and receiving probes at the optimum transverse and longitudinal locations, and for the case of both probes shifted transversely by $0.25w$ towards the edge of the waveguide. To illustrate the full width of the passband for the centered case beyond the limitations of the 67-GHz network analyzer, the FDTD-calculated insertion loss for the centered case is also shown.
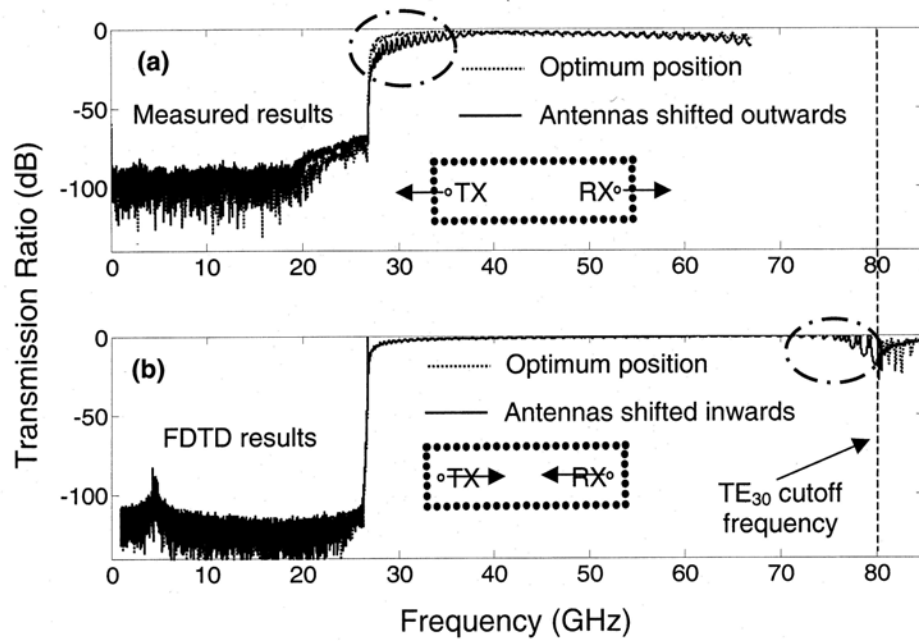
Figure 8 Comparison of the S_{21} characteristics for 7.6-cm-long SIW interconnects of the type shown in Fig. 4, one having transmitting and receiving probes at the optimum transverse and longitudinal locations, and one having both probes: (a) shifted longitudinally outwards toward the end of the waveguide by 1.5r; and (b) shifted longitudinally inwards towards the center of the waveguide by 1.5r. The effect of shifting the probes has on the bandwidth is highlighted with superimposed circles.
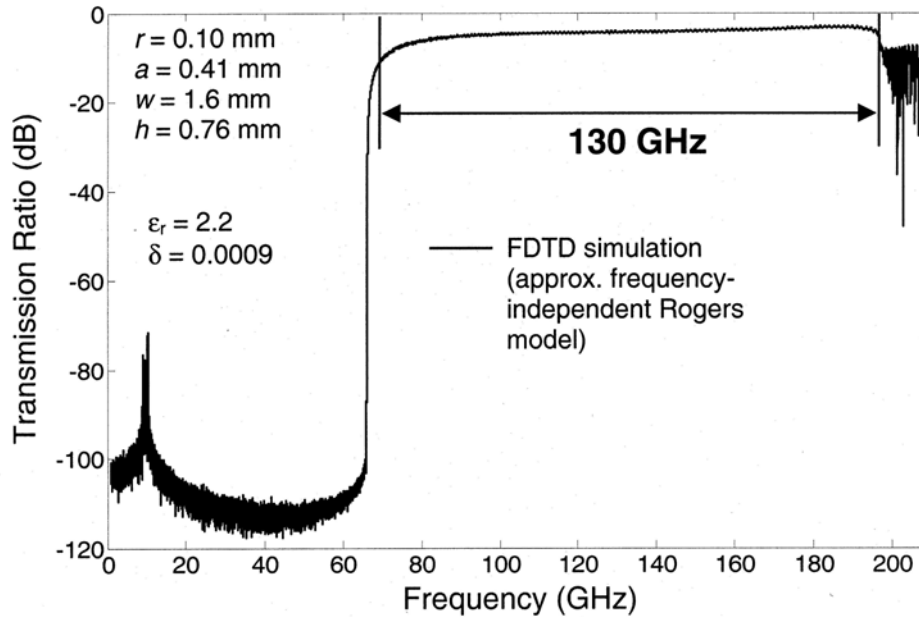
Figure 9 FDTD-calculated S_{21} characteristic over a 7.6-cm-long SIW interconnect analogous to that shown in Fig. 4, but scaled to a center frequency of 130 GHz.

V. CROSSTALK STUDY

This section presents the computational and experimental results for crosstalk between adjacent SIWs. Two waveguides of the type shown in Fig. 4 are arranged to share a row of pins along a common sidewall as shown in the insets of Figs. 10(a) and 10(b). Two types of crosstalk are considered: from TX to XT1 in a direction normal to the common sidewall; and from TX to XT2, representing a longitudinal coupling of the two waveguides. Each waveguide's dimensions are equivalent to the 50-GHz center-frequency waveguide considered in Section IV (pin radius r = 0.24 mm, pin center-to-center spacing a = 0.68 mm, waveguide width w = 4.1 mm, waveguide height h = 0.76 mm, and 0.20 mm gaps between adjacent pins). Excitation is provided at TX by the same 134-psec, 50-GHz carrier pulse described earlier in Section IV.

Figs. 10(a) and 10(b) show the FDTD-calculated crosstalk voltage time-waveforms at XT1 and XT2, respectively. These waveforms are normalized relative to the maximum received voltage time-waveform value at RX. The peak crosstalk voltages at XT1 and XT2 are on the order of 0.02% and 1%, respectively, relative to the peak voltage of the desired received signal.
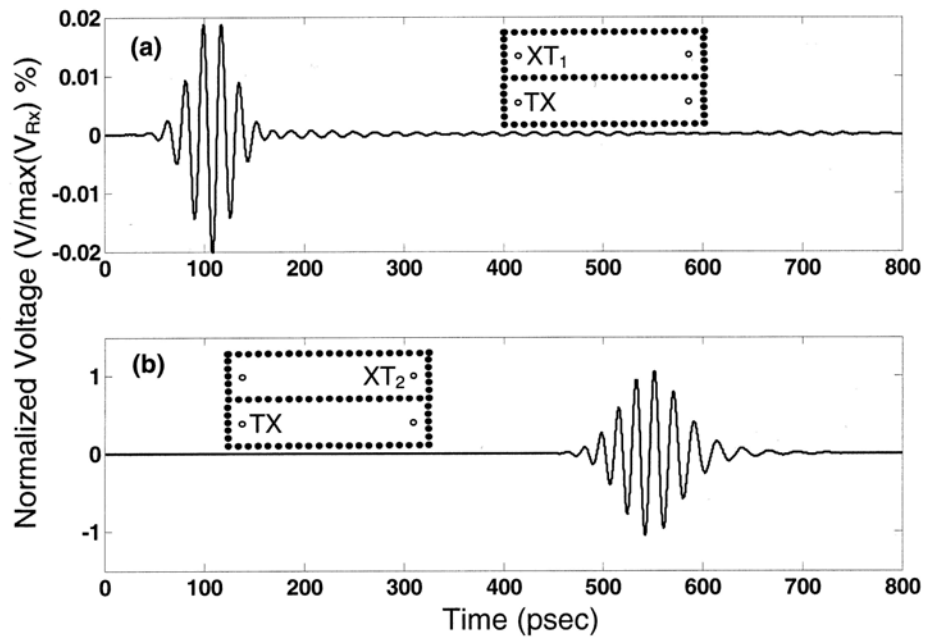
Figure 10 The FDTD-calculated crosstalk voltage time-waveforms at: (a) XT1; and (b) XT2. These waveforms are for an assumed 134-psec (full-width at half-maximum) transmitted 50-GHz carrier pulse having a Gaussian envelope, and are normalized relative to the maximum received voltage time-waveform value at RX.
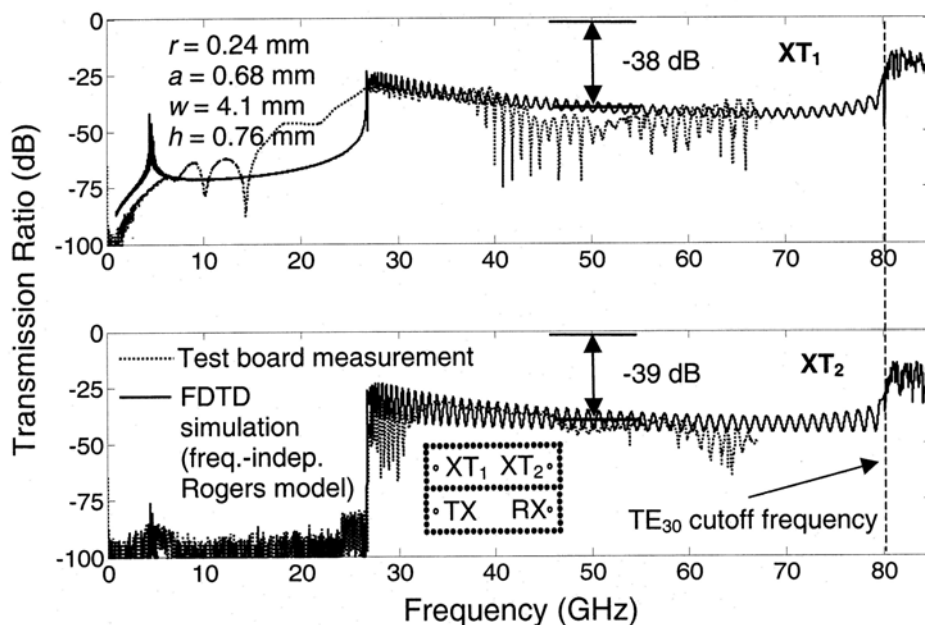
Figure 11 Comparison between the measured and FDTD-calculated crosstalk for two

adjacent 7.6-cm-long SIW interconnects of the type shown in Fig. 4. For both

XT 1 and XT 2, the crosstalk level is below -30 dB wherein 0.20-mm gaps

exist between the adjacent vias having $r = 0.24$ mm.

Fig. 11 shows the associated spectrum of the measured and FDTD-calculated crosstalk

between the SIWs of Fig. 10. For pin-to-pin gaps on the order of 42% of the size of each pin,

one row of pins can suppress the worst-case crosstalk to below -30 dB, which is well within

tolerable levels for interconnects.

VI. OPTIMIZED 45° AND 90° BENDS

This Section reports FDTD modeling results for optimized 45° and 90° SIW bends capable of

maintaining the ultrawide relative bandwidth of ~100%. Here, a design is sought after that

minimally degrades the ultrawideband characteristics of the straight SIW structures considered in

the previous sections. Extensive studies have shown that, without careful placement of the vias

in the vicinity of the bend, odd modes are generated which reduce the single-mode passband by

about 50 %, in the manner seen in Fig. 7.
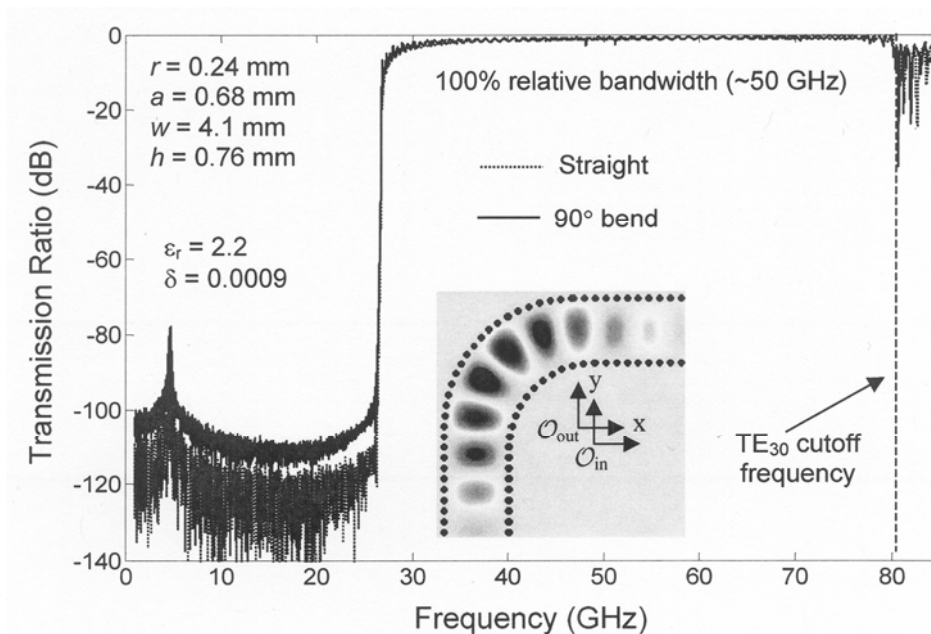
Figure 12 Comparison between the FDTD-calculated S_{21} characteristics of the straight

and 90° bend SIWs of the type shown in Fig. 4.

Fig. 12 illustrates the results for the most promising arrangement for a 90° bend. Here, the

outer circular arc of vias has a 4.1-mm radius of curvature, while the inner circular arc has a 5.4-

mm radius of curvature whose origin is displaced radially inward by 1.4 mm relative to the

origin of the outer arc. These differences between the two sidewall arcs counteract the differing

propagation lengths along the inside and outside edges of the bend. As seen in the graph of Fig.

12, there is very little difference between the calculated ultrawideband S_{21} characteristics for the

optimized 90°-bend and a straight SIW having the same overall length. Furthermore, as shown

in the inset of Fig. 12, there is little if any odd mode generation even for the worst case of a

propagating pulse localized within the bend.
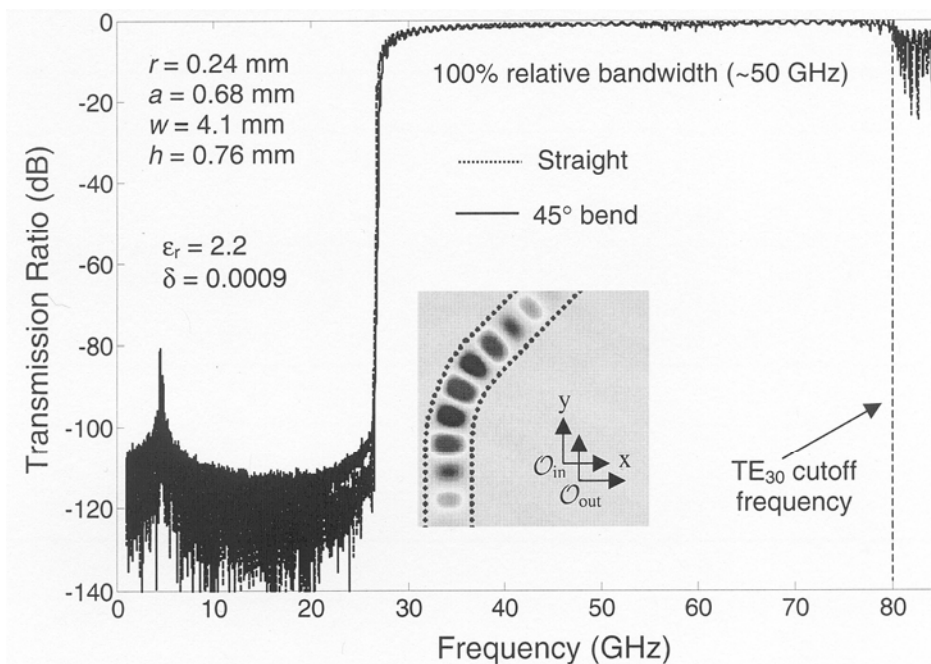
Figure 13 Comparison between the FDTD-calculated S_{21} characteristics of the straight

and 45° bend SIWs of the type shown in Fig. 4.

Fig. 13 illustrates the results for the most promising arrangement for a 45° bend. Here, the

outer elliptical arc of vias is described by $x^2 + y^2/1.2 = 9.5$ mm, while the inner circular arc has

an 8.2-mm radius of curvature whose origin is displaced radially outward by 1.4 mm relative to

the origin of the outer arc. As seen in the graph of Fig. 13, there is very little difference between

the calculated ultrawideband S_{21} characteristics for the optimized 45°-bend and a straight SIW

having the same overall length. Furthermore, as shown in the inset of Fig. 13, there is little if

any odd mode generation even for the worst case of a propagating pulse localized within the bend.

VII. SECOND-GENERATION HALF-WIDTH FOLDED SIWs

This section presents computational and experimental results for second-generation SIWs of half-width folded geometry [20]. Specifically, double-folded SIWs are discussed, wherein both sides of the waveguide are folded under in the direction of propagation as shown in Fig. 14. This folding of the waveguide provides a 50% narrower interconnect that is potentially more useful relative to the regular SIWs because it requires less circuit board space and therefore less cost. Figure 15 shows a photo of the lab prototype of the double-folded SIW. It is 2 mm wide, whereas the regular SIW considered in Section IV and shown in Figure 4 is 4.1 mm wide. Further, although the folded SIW shown in Figs. 14 and 15 is twice as thick, simulation results show that the thickness can be made arbitrarily small (limited only by manufacturing capabilities).
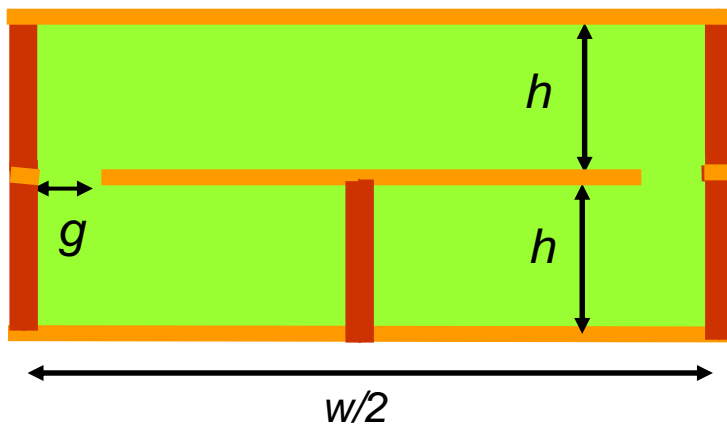
Figure 14 Cross-sectional view of a double-folded SIW.
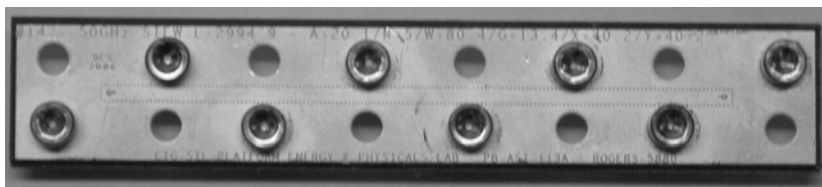
Figure 15 Photo of a 7.6-cm-long double-folded SIW interconnect scaled to a center frequency of 50 GHz. This test structure is comprised of Rogers RT/duroid® 5880 dielectric material ($\varepsilon_r = 2.2$ and tan $\delta = 0.0009$) and has $r = 0.12$ mm, $a = 0.51$ mm, $w = 2.0$ mm, and $h = 0.76$ mm. Thus, it is half as wide in the direction of propagation as the first generation SIWs considered in the above sections.
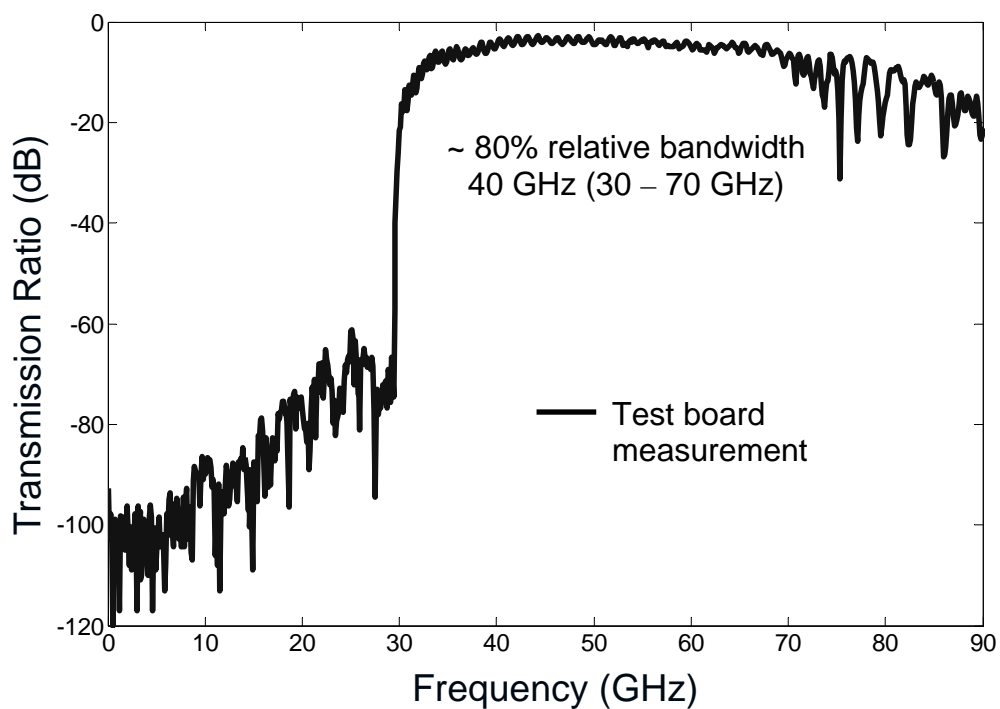
Figure 16 Measured S_{21} characteristic over the 7.6-cm-long double-folded SIW interconnect shown in Fig. 15.

Measured results for the 7.6-cm-long double-folded SIW of Fig. 15 are presented in Fig. 16. The second-generation half-width SIW is shown to provide ~80% relative bandwidth while requiring only half as much space in the transverse direction. Although this relative bandwidth is smaller than the regular SIW, it could still outperform present-day stripline interconnects as discussed in the Introduction and Section II.

VIII. CONCLUSIONS AND ONGOING WORK

This Appendix reported an experimental and computational study of SIWs optimized for use as ultrahigh-speed bandpass waveguiding digital interconnects. Specifically, it was shown how to design SIWs optimized for narrow transverse dimensions, low loss, low crosstalk, and maximum bandwidth with no multimoding. The novelty of this work resides in the successful design, fabrication, and testing of low-loss SIWs that achieve 100% relative bandwidths via optimal excitation of the dominant TE_{10} mode and avoidance of the excitation of the TE_{20} mode. Furthermore, these optimal structures maintain their 100% relative bandwidth while transmitting around 45° and 90° bends, and achieve measured crosstalk of better than –30 dB over the entire passband. The computational designs were supported with laboratory measurements of prototype SIWs that achieved ~100% relative bandwidths at center frequencies of 50 GHz, accommodating in principle data rates of 50 Gb/sec.

Second-generation SIWs were also demonstrated, providing 80% relative bandwidths while requiring only half as much space in the transverse direction.

Because existing circuit-board technology permits dimensional reductions of SIWs by a factor of 4:1 relative to the ones discussed here, bandpass operation at center frequencies approaching 200 GHz with data rates of 200 Gb/sec are feasible. These data rates meet or

exceed those expected eventually for proposed optical interconnects without requiring the development of a suite of essentially revolutionary silicon photonic technologies.

As future work, designs of structures for frequency-division multiplexing/demultiplexing of multiple data channels onto a single SIW will be designed, and working prototypes will be demonstrated, wherein SIWs are connected to actual Intel processors and memories.

REFERENCES

[1]   S. Coffa, "Light From Silicon," *IEEE Spectrum Magazine*, p. 44 – 49, Oct. 2005.

[2]   J. Hirokawa and M. Ando, "Single-layer feed waveguide consisting of posts for plane TEM wave excitation in parallel plates," *IEEE Trans. on Antennas and Propagation*, vol. 46, no. 5, May 1998.

[3]   H. Uchimura, T. Takenoshita, and M. Fujii, "Development of a 'laminated waveguide,'" *IEEE Trans. on Microwave Theory and Techniques*, vol. 46, no. 12, Dec. 1998.

[4]   F. Xu and K. Wu, "Guided-wave and leakage characteristics of substrate integrated waveguide," *IEEE Trans. on Microwave Theory and Techniques*, vol. 53, no. 1, Jan. 2005.

[5]   F. Capolino, D. R. Jackson, and D. R. Wilton, "Mode excitation from sources in two-dimensional SIW waveguides using the array scanning method," *IEEE Microwave and Wireless Components Lett.*, vol. 15, no. 2, Feb. 2005.

[6]   A. Zeid and H. Baudrand, "Electromagnetic Scattering by metallic holes and its applications in microwave circuit design," *IEEE Trans. on Microwave Theory and Techniques*, vol. 50, no. 4, April 2002.

[7]   L. Yan, W. Hong, K. Wu, T. J Cui, "Investigations on the propagation characteristics of the substrate integrated waveguide based on the method of lines," IEE Proceedings Microwaves, Antennas and Propagation, vol. 152, no. 1, pp. 35-42, 2005.

[8]   F. Xu, K. Wu, W. Hong, "Domain decomposition FDTD algorithm combined with numerical TL calibration technique and its application in parameter extraction of substrate integrated circuits," IEEE Trans. Microwave Theory and Techniques, vol. 54, no. 1, pp. 329-338, 2006.

[9]   J. J. Simpson, A. Taflove, J. A. Mix, and H. Heck, "Substrate integrated waveguides optimized for ultrahigh-speed digital interconnects," *IEEE Microwave Theory and Techniques*, in press.

[10]   E. Yablonovitch, "Photonic band-gap structures," *J. Optical Society of America B*, vol. 10, pp. 283-295, 1993.

[11]   J. D. Joannopoulos, R. D. Mead, and J. N. Winn, *Bandgap structures: Molding the Flow of Light*. Princeton, NJ: Princeton University Press, 1995.

[12]   A. Taflove and S. C. Hagness, *Computational Electrodynamics: The Finite-Difference Time-Domain Method*, 3rd ed. Norwood, MA: Artech House, 2005.

[13]   G.E. Moore, "Cramming more components onto integrated circuits," *Electronics*, vol. 38, no. 8, April 19, 1965.

[14]   G.E. Moore, "No exponential is forever: but 'forever' can be delayed," *Digest of Technical Papers IEEE solid-State Circuit Conference, 2003*, vol. 1, pp. 20-23, San Francisco, CA, February 2003.

[15] J.H. Sinsky, M. Duelk, A. Adamiecki, "High-speed electrical backplane transmission using duobinary signaling," IEEE Transactions on Microwave Theory and Techniques, vol. 53, no. 1, pp. 152-160, January 2005.

[16] J. J. Simpson, A. Taflove, J. A. Mix, and H. Heck, "Computational and experimental study of a microwave electromagnetic bandgap structure for potential use as a bandpass wireless interconnect," *IEEE Microwave and Wireless Components Lett.*, vol. 14, no. 7, pp. 343-345, July 2004.

[17] M. Piket-May, W. K. Gwarek, T.-L. Wu, B. Houshmand, T. Itoh, and J. J. Simpson "High-speed electronic circuits with active nonlinear components," in *Computational Electrodynamics: The Finite-Difference Time-Domain Method, 3rd ed.*, A. Taflove and S. C. Hagness, Norwood, MA: Artech House, 2005.

[18] M. Celuch-Marcysiak, W. K. Gwarek, and M. Sypniewski, "A simple and effective approach to FDTD modeling of structures including lossy metals," Proc. Asia-Pacific Microwave Conf., Yokohama, Japan, Dec. 1998, pp. 991-993.

[19] S.-K. Fan, J.-A. Paik, P. Patterson, M.C. Wu, B.Dunn, and C.-J. Kim, "MEMS with thin-film aerogel," IEEE Conf. Micro Electro Mechanical Systems (MEMS '01), Interlaken, Switzerland, Jan. 2001, pp. 122-125.

[20] Grigoropoulos et. al., "Substrate integrated folded waveguides and filters," *IEEE Micr. Wireless Comp. Lett.*, vol. 15, no. 12, pp. 829-831, Dec. 2005.

Jamesina J. Simpson

Electrical Engineering and Computer Science Department
2145 Sheridan Road, Northwestern University, Evanston IL 60208
Email: j-simpson@northwestern.edu, Tel: (847) 332-4750, Fax: (847) 491-4455
URL: http://www.ece.northwestern.edu/~jjs756/

Education

Northwestern University, Evanston, IL

- *B.S. in Electrical Engineering with Honors*   June 2003
  Specialization in Electromagnetics and Photonics

- *Ph.D. in Electrical Engineering*   *Degree Anticipated*: June 2007

Dissertation

Title: "Three-Dimensional FDTD Modeling of Impulsive Extremely Low-Frequency Electromagnetic Wave Propagation in the Global Earth-Ionosphere Waveguide"

Chair: Prof. Allen Taflove

Current Research Areas

- Computational electromagnetics theory and applications, especially finite-difference time-domain (FDTD) solutions of Maxwell's equations
- Novel ultrawideband waveguiding interconnects for ultrahigh-speed digital data buses
- Geophysically induced ultralow-frequency (ULF) and extremely low-frequency (ELF) electromagnetic phenomena in the Earth-ionosphere waveguide
- Photonic applications, including photonic interconnects and biophotonics

Honors, Awards, and Grants-in-Aid

- 2001 Summer Grant, Northwestern University Undergraduate Research Committee ($3,600)
- 2001-03 Undergraduate research assistantship funded by Intel Corporation (full tuition)
- 2002 German Academic Exchange Service (DAAD) Undergraduate Award ($2,500)
- 2003 Institute of Electrical and Electronics Engineers (IEEE) Antennas and Propagation Society (AP-S) International Symposium Student Paper Contest Finalist
- 2003-04 Northwestern University McCormick School of Engineering Murphy First-Year Graduate Fellowship (full tuition + stipend)
- 2004-05 IEEE AP-S Graduate Research Award ($2,500)
- 2004-05 Graduate research assistantship funded by Intel Corporation (full tuition + stipend)
- 2005-07 National Science Foundation (NSF) Graduate Fellowship (full tuition + stipend)
- 2006 IEEE Microwave Theory and Techniques Society (MTT-S) Graduate Fellowship ($6,000)
- 2006-07 Northwestern University McCormick School of Engineering Richter Dissertation-Year Fellowship (declined due to prior NSF Graduate Fellowship)

Academic Research Experience

Two distinct projects in Prof. Taflove's Computational Electromagnetics Lab., both starting from the freshman undergraduate year in March 2000 and continuing to the Ph.D.:

- **Ultrahigh-Speed Wireless Digital Bus Interconnects** (funded by Intel Corporation) Constructed and ported to NSF Teragrid supercomputers new three-dimensional (3-D) FDTD computational electromagnetics models of novel substrate integrated waveguides (SIWs) for board-level interconnects between advanced digital processors. Developed novel SIW designs based upon these FDTD models for subsequent testing at Intel Corporation; these SIWs potentially yield bit rates more than 10 times those currently available, and would thereby satisfy Intel's needs for at least the next decade.

- **ULF/ELF Worldwide Propagation Models** (supported by the NSF Graduate Fellowship) Constructed and ported to NSF Teragrid supercomputers new 3-D FDTD computational electromagnetics models of geophysically induced ULF/ELF electromagnetic phenomena within the global Earth-ionosphere waveguide. Proposed novel ULF/ELF remote-sensing techniques for major oil deposits and potential preseismic ionospheric anomalies based upon these FDTD models.

Internship Experience

June 2002 – Sept. 2002　　　　　Hannover, Germany
Undergraduate Research Assistant, Prof. Heyno Garbe's Electromagnetic Compatibility Lab
　Created original 3-D FDTD models of open area test sites for optimizing groundplane designs for electromagnetic compatibility testing; took antenna measurements for comparison (supported by a 2002 German Academic Exchange Service (DAAD) grant).

June 2003—Sept. 2003　　　　　Hillsboro, OR
Undergraduate Engineering Intern, Intel Corporation, Initiative Ingredient Development: Interconnect Technologies
　Performed proof-of-concept experimental and computational studies of moderate-speed electromagnetic bandgap (EBG) waveguiding interconnects in standard circuit boards.

June 2004—Sept. 2004　　　　　Hillsboro, OR
Graduate Engineering Intern, Intel Corporation, Corporate Technology Group (CTG): Systems Technology Lab (STL)
　Performed proof-of-concept experimental and computational studies of optimized ultrahigh-speed EBG waveguiding interconnects in standard circuit boards having five times the bit rate of those tested during the previous internship.

June 2005—Sept. 2005　　　　　Hillsboro, OR
Graduate Engineering Intern, Intel Corporation, CTG: STL
　Performed experimental and computational studies of ultrahigh-speed SIWs evolved from the EBG interconnects of the previous two internships; demonstrated straight and right-angle bend SIWs providing Intel's required values of loss, crosstalk, and bandwidth.

June 2006 – Sept. 2006　　　　　Hillsboro, OR
Graduate Engineering Intern, Intel Corporation, CTG: STL
　Performed experimental and computational feasibility studies of substrate integrated folded waveguides (SIFWs) optimized for use as ultrahigh-speed digital interconnects; demonstrated that SIFWs can provide Intel's required ultrawide bandwidths while using only half as much circuit board space as the SIWs tested during the previous internship.

Invited Talks

[1] **J. J. Simpson**, A. Taflove, J. A. Mix, and H. Heck, "Ultrahigh-speed wireless digital bus interconnects using electromagnetic bandgap (EBG) technology," *IEEE AP-S / MTT-S Chapter Meeting*, Chicago, IL, Nov. 2004.

[2] **J. J. Simpson** and A. Taflove, "Recent advances in FDTD modeling of ULF/ELF propagation within the global Earth-ionosphere waveguide," *U.S. National Committee (USNC) / International Union of Radio Science (URSI) Annual Meeting*, Boulder, CO, Jan. 2005.

[3] **J. J. Simpson**, A. Taflove, J. A. Mix, and H. Heck, "An experimental and computational study of bandpass wireless digital-bus interconnects using electromagnetic bandgap technology at 50 GHz," *IEEE AP-S International Symposium,* Washington, D.C., July 2005.

[4] **J. J. Simpson** and A. Taflove, "3-D FDTD modeling of ULF/ELF propagation within the global Earth-ionosphere cavity using an optimized geodesic grid," *IEEE AP-S International Symposium,* Washington, D.C., July 2005.

[5] **J. J. Simpson** and A. Taflove, "Progress in three-dimensional FDTD Maxwell's equations modeling of global impulsive ULF/ELF propagation," *Progress in Electromagnetics Research Symposium*, Tokyo, Japan, Aug. 2006.

Book Chapters

[1] A. Taflove and **J. J. Simpson**, "Introduction to Maxwell's Equations and the Yee Algorithm," Chap. 3 in *Computational Electrodynamics: The Finite-Difference Time-Domain Method, 3rd ed.*, A. Taflove and S. C. Hagness, Norwood, MA: Artech, 2005.

[2] M. Piket-May, W. K. Gwarek, T.-L. Wu, B. Houshmand, T. Itoh, and **J. J. Simpson** "High-Speed Electronic Circuits with Active and Nonlinear Components," Chap. 15 in *Computational Electrodynamics: The Finite-Difference Time-Domain Method, 3rd ed.*, A. Taflove and S. C. Hagness, Norwood, MA: Artech, 2005.

Refereed Journal Papers

[1] **J. J. Simpson** and A. Taflove, "Two-dimensional FDTD model of antipodal ELF propagation and Schumann resonance of the Earth," *IEEE Antennas and Wireless Propagation Letters*, vol. 1, no. 2, pp. 53-56, 2002.

[2] **J. J. Simpson** and A. Taflove, "Three-dimensional FDTD modeling of impulsive ELF antipodal propagation and Schumann resonance of the Earth-sphere," *IEEE Transactions on Antennas and Propagation*, vol. 52, no. 2, pp. 443–451, Feb. 2004.

[3] **J. J. Simpson**, A. Taflove, J. A. Mix, and H. Heck, "Computational and experimental study of a microwave electromagnetic bandgap structure for potential use as a bandpass wireless interconnect," *IEEE Microwave and Wireless Components Letters*, vol. 14, no. 7, pp. 343-345, July 2004.

[4] **J. J. Simpson** and A. Taflove, "Efficient modeling of impulsive ELF antipodal propagation about the Earth sphere using an optimized two-dimensional geodesic FDTD grid," *IEEE Antennas and Wireless Propagation Letters*, vol. 3, no. 11, pp. 215-218, 2004.

[5] **J. J. Simpson** and A. Taflove, "Electrokinetic effect of the Loma Prieta earthquake calculated by an entire-Earth FDTD solution of Maxwell's equations," *Geophysical Research Letters,* vol. 32, L09302, doi:10.1029/2005GL022601, 2005.

[6] **J. J. Simpson** and A. Taflove, "A novel ELF radar for major oil deposits," *IEEE Geoscience and Remote Sensing Letters*, vol. 3, no. 1, pp. 36-39, 2006.

[7]   **J. J. Simpson**, A. Taflove, J. A. Mix, and H. Heck, "Substrate integrated waveguides optimized for ultrahigh-speed digital interconnects," *IEEE Transactions on Microwave Theory and Techniques*, vol. 54, no. 5, pp. 1983-1990, May 2006.

[8]   **J. J. Simpson**, R. P. Heikes, and A. Taflove, "FDTD modeling of a novel ELF radar for major oil deposits using a three-dimensional geodesic grid of the Earth-ionosphere waveguide," *IEEE Transactions on Antennas and Propagation*, vol. 54, no. 6, pp. 1734-1741, June 2006.

[9]   **J. J. Simpson** and A. Taflove, "ELF radar system proposed for localized D-region ionospheric anomalies," *IEEE Geoscience and Remote Sensing Letters*, vol. 3, no. 4, pp. 500-503, Oct. 2006.

[10] **J. J. Simpson** and A. Taflove, "A review of progress in FDTD Maxwell's equations modeling of impulsive sub-ionospheric propagation below 300 kHz," *IEEE Transactions on Antennas and Propagation*, in press.

Refereed Conference Proceedings

[1]   **J. J. Simpson** and A. Taflove, "FDTD modeling of millimeter-wave photonic bandgap structures for potential use as ultrahigh speed bandpass wireless interconnects," *Proc. USNC/URSI National Radio Science Meeting*, San Antonio, TX, p. 82, June 2002.

[2]   **J. J. Simpson** and A. Taflove, "Two-dimensional FDTD modeling of impulsive ELF antipodal propagation about the Earth-sphere," *Proc. IEEE AP-S International Symposium*, San Antonio, TX, vol. 3, pp. 678-681, June 2002.

[3]   A. Taflove, **J. J. Simpson**, and G. Chang, "Two emerging multiphysics FDTD applications from the megameter scale at 3 Hz to the nanometer scale at 300 THz," *Proc. USNC/URSI National Radio Science Meeting*, Columbus, OH, June 2003.

[4]   **J. J. Simpson** and A. Taflove, "Global three-dimensional FDTD modeling of impulsive ELF propagation about the Earth," *Proc. IEEE AP-S International Symposium*, Columbus, OH, vol. 4, pp. 940-943, June 2003.

[5]   **J. J. Simpson** and A. Taflove, "Computational study of millimeter-wave metal-pin photonic bandgap waveguides for use as ultrahigh-speed bandpass wireless interconnects," *Proc. IEEE AP-S International Symposium*, Columbus, OH, vol. 4, pp. 871-874, June 2003.

[6]   **J. J. Simpson** and A. Taflove, "Three-dimensional FDTD modeling of the response of the global Earth-ionosphere waveguide to seismically-induced sources," *Proc. USNC/URSI National Radio Science Meeting*, Monterey, CA, June 2004.

[7]   **J. J. Simpson**, A. Taflove, J. A. Mix, and H. Heck, "A study of a microwave electromagnetic bandgap structure with waveguiding defect for potential use as a bandpass wireless interconnect," *Proc. IEEE AP-S International Symposium,* Monterey, CA, vol. 2, pp. 1523-1526, June 2004.

[8]   **J. J. Simpson** and A. Taflove, "Recent advances in FDTD modeling of ULF/ELF propagation within the global Earth-ionosphere waveguide," *Proc. USNC/URSI National Radio Science Meeting*, Boulder, CO, F2-3, p. 167, Jan. 2005.

[9]   **J. J. Simpson** and A. Taflove, "Whole Earth FDTD modeling of ELF electromagnetic sounding of oil deposits with the U.S. Navy's ELF transmitter system," *Proc. USNC/URSI National Radio Science Meeting*, Washington, D.C., July 2005.

[10] **J. J. Simpson**, A. Taflove, J. A. Mix, and H. Heck, "An experimental and computational study of bandpass wireless digital-bus interconnects using electromagnetic bandgap technology at 50 GHz," *Proc. IEEE AP-S International Symposium,* Washington, D.C., July 2005.

[11] **J. J. Simpson** and A. Taflove, "3-D FDTD modeling of ULF/ELF propagation within the global Earth-ionosphere cavity using an optimized geodesic grid," *Proc. IEEE AP-S International Symposium,* Washington, D.C., July 2005.

[12] **J. J. Simpson** and A. Taflove, "Global 3-D FDTD Maxwell's equations modeling of ionospheric disturbances associated with earthquakes using an optimized geodesic grid," *Proc. American Geophysical Union Fall Meeting*, San Francisco, CA, Dec. 2005.

[13] **J. J. Simpson** and A. Taflove, "An investigation of a novel radar for ionospheric disturbances using a global 3-D FDTD model of the earth-ionosphere waveguide," *Proc. URSI National Radio Science Meeting*, Boulder, CO, Jan. 2006.

[14] **J. J. Simpson**, A. Taflove, J. A. Mix, H. Heck, "Optimized substrate integrated waveguide bends for high-speed digital circuits," *Proc. IEEE AP-S International Symposium*, Albuquerque, NM, July 2006.

[15] **J. J. Simpson** and A. Taflove, "Proposal for an ELF radar of D-region ionospheric anomalies analyzed using a 3-D geodesic FDTD model of the Earth-ionosphere waveguide," *Proc. IEEE AP-S International Symposium*, Albuquerque, NM, July 2006.

[16] **J. J. Simpson** and A. Taflove, "3-D FDTD Maxwell's equations modeling of sub-30 kHz electromagnetic wave propagation in the Earth-ionosphere waveguide including ionospheric plasma as influenced by the geomagnetic field," Proc. American Geophysical Union Fall Meeting, San Francisco, CA, Dec. 2006.

Other Presentation

[1] **J. J. Simpson** and A. Taflove, "Three-dimensional FDTD modeling of the response of the global Earth-ionosphere waveguide to seismically-induced sources using latitude/longitude and spherical geodesic grids," *2nd International Conference on Discrete Global Grids*, Ashland, OR, Oct. 2004.

Academic Service

[1] **Session Chair**, "Innovative Approaches to Solving Large and Multiscale Radiation and Scattering Problems," *IEEE Antennas and Propagation Society International Symposium*, Washington, D.C., 2005.

[2] **Special Session Organizer and Chair**, "Emerging Techniques and Applications for FDTD Computational Modeling of Planetary Electromagnetic Wave Propagation in the ULF, ELF, and VLF bands," *North American Radio Science Meeting*, Ottawa, Canada, 2007 (to be held).

[3] **Reviewer**: *IEEE Transactions on Geoscience and Remote Sensing*; *IEEE Microwave and Wireless Components Letters*; *Annales Geophysicae*

Professional Society Memberships

IEEE Antennas and Propagation Society
IEEE Microwave Theory and Techniques Society
Tau Beta Pi Engineering Honor Society
Eta Kappa Nu Electrical Engineering Honor Society
American Geophysical Union (AGU)

Leadership Experience

Sept. 2001 – June 2003   Evanston, IL
Resident Assistant, September 2002 – June 2003: Slivka Hall (Science and Engineering Residential College); September 2001 – June 2002: Goodrich House (all-female hall)
Served as a mentor and advisor to 50 undergraduate students; utilized organizational and public speaking skills to plan and present social, educational, and recreational hall programs.

Feb. 2004 – present   Evanston, IL
Assistant Master, Shepard Residential College (multi-thematic)
Coordinated social and academic events and opportunities to foster interaction between 180 undergraduate residents and faculty from all seven schools of Northwestern University. Also served as an informal advisor to students, performed budgetary tasks, and supervised special equipment.

Skills

Programming Languages: FORTRAN, MATLAB
Parallel Programming Language: FORTRAN MPI
Software: OpenDX
Operating Systems: Windows, UNIX, Linux
Foreign Language: Proficient in German, including speaking, reading, and writing
License: Amateur Radio Operator (Extra Class, Callsign: AB9HZ)